Modeling and Inversion of CSEM Data using Green's Function Methods

Musisi Norbert

Master Degree in Petroleum Geoscience

Department of Earth Science

University of Bergen

June 2014

Abstract

The aim of the present study is to develop new approximations to the integral equation for 3D Controlled Source Electromagnetic (CSEM) synthetic data. Several scattering approximations to the integral equation have previously been developed to simulate the electromagnetic problems. In this thesis, new approaches to the approximate solution for the integral equation in 3D for marine CSEM at low frequency using the T-matrix approximation (TMA) and the Extended Born approximation (EBA) have been presented. Unlike the EBA that has been previously discussed in CSEM, the TMA has not yet been extended to CSEM though with many applications in seismics. The T-matrix approach only requires the knowledge of the perturbations and the Green's function to compute the electric field whereas the Extended Born approximation for electromagnetic forward modeling improves the ability to accurately simulate the internal fields for a distribution without inverting a large 3D matrix. The new methods have been implemented in MATLAB for forward modeling on synthetic marine CSEM data and the solutions compared with the Born approximation. In addition, sensitivity and validity of these methods for a reservoir in production with varying contrasts have been studied with several examples to show their accuracy. It appears that the new approximations have better accuracy and a wider electrical conductivity application range. The T-matrix is expected to approximate roughly the full integral equation solution for electromagnetic (EM) field, while the Extended Born is expected to improve the approaches of EM field over large conductivity contrasts between the reservoir and background model, compared to the Born approximation. The T-matrix and the Extended Born are valid for high contrasts. The effects of these approximations to different reservoir parameters have also been investigated. To improve the accuracy of these approximations, the number of grid blocks need to be increased at the expense of the computational cost. A cubic reservoir model works better than the rectangular block model for the T-matrix. Using numerical and analytical modeling, the T-matrix and the Extended Born have been expanded to CSEM monitoring of geophysical anomalies in the pore-fluid contents of the subsurface reservoirs. The ability of time-lapse CSEM data to monitor small changes in the electrical conductivity has been discussed. It has been found that these methods can detect the changes in the contrast of the reservoir due to fluid injection.

Acknowledgements

First, I would like to express my sincere gratitude to my advisor and supervisor, Prof. Jakobsen Morten, for his much needed encouragement, patience, and guidance along the path of this research. He always had time for me and made me feel that our topic of discussion was the most important item of the day. Without his support I would never have successfully completed as much accurate and faster as I did.

In addition, I would like to extend my appreciation to Associate professor Henk Keers for the skills and guidance he has given me as far as MATLAB programing is concerned.

I wish to thank the Norwegian government, through the Department of Earth Science, University of Bergen, for financing my master studies, otherwise my studies and this thesis would not have been possible.

It is imperative to express my sincere gratitude to the many people who saw me through this book; to all those who provided support, talked things over, read, wrote, offered comments, allowed me to quote their remarks and assisted in the editing, proofreading and design.

Last, but not least, I am extremely grateful to brother Edward and mother Beatrice for allowing me to spend most of their ample, valuable and much needed time on this thesis and as a student in Bergen.

……

Musisi Norbert Bergen, June 2014

Table of Contents

List of Figures

1 Introduction

1.1 CSEM Survey

Electromagnetic fields are useful in geophysics due to their interactive nature with the medium through which they propagate (Zhdanov 2009). This interaction can be used to determine certain physical properties of rocks, these being electrical conductivity $\boldsymbol{\sigma}$, dielectric permittivity $\boldsymbol{\varepsilon}$, and magnetic permeability $\boldsymbol{\mu}$. The electromagnetic methods are based on the study of the propagation of electric currents and/or electromagnetic fields in the Earth. Electrical resistivity of the subsurface provides important information on the porosity and pore geometry of the geologic formations as well as the nature of the fluids that fill the pore spaces. Resistivity increases exponentially for hydrocarbon bearing rocks, resulting into a strong resistivity contrast between gas-saturated and brine-saturated geological media.

Until of recent, the seismic method has been the dominant technique used for reservoir detection and monitoring. Due to its shortcomings, different electromagnetic methods have been developed to detect and monitor geological hydrocarbons. Electromagnetic (EM) methods have provided a more cost effective monitoring technique that, at a minimum, has reduced the frequency of seismic surveys. CSEM which exploits the conductivity contrasts in the subsurface sediments has become an important complementary tool for offshore petroleum exploration prior to drilling (Eidesmo, S. Ellingsrud et al. 2002, Mehta.K, Nabighian.M et al. 2005, Bakr and Mannseth 2009). Marine CSEM survey has been used in; estimating the formation resistivity without using borehole logs (Constable and Weiss 2006), CO_2 sequestration monitoring (Kang, Seol et al. 2011), and 3D modeling and time-lapse of CO_2 (Bhuyian, Landrø et al. 2012). It can effectively detect marine reservoirs with high saturation of up to 60- 80% (Wang, Luo et al. 2008, Constable 2010). This technique has been used mainly in discriminating between the hydrocarbon and the water-filled rocks in addition to estimating the geometry of the hydrocarbon (Bhuyian, Landrø et al. 2012). Hydrocarbons have a low conductivity less than 0.01 S/m while the formation water has a high conductivity of up to 10 S/m. Hence, the EM signal is strongly influenced by the pore-fluid contents (Bhuyian, Landrø et al. 2012).

1.1.1 Forward Modeling

Modeling data plays an important role in the standardization of the background field and the reservoir dimensions that play an important role during time-lapse CSEM monitoring. Time-lapse CSEM can normally be used as a reservoir monitoring tool to help in the reservoir management (Bhuyian, Landrø et al. 2012). Assuming that other changes in the reservoir properties remain unaffected by the changes in the pore-fluid content, monitoring the production of hydrocarbons will help to observe and track any changes in the subsurface

distribution through detection of changes in conductivity. The developed methods were tested for monitoring of geolectrical data to model the changes in saturation as reservoir production took place.

1.1.2 Inverse Modeling

Inversion of marine CSEM data has been previously done using Bayesian algorithm (Ray and Key 2012). Torres-Verdin and Habashy (1995) performed a linear inversion of 2D electrical conductivity. Basing on these studies, 3D inversion modeling of CSEM data has been done. In solving the inverse problems, the mathematical difficulty is that the inverse operator may not exist or may not be continuous over a given domain. Electromagnetic inversion methods are widely used in the interpretation of geophysical electromagnetic data in mineral, hydrocarbon, and underground water exploration. The EM response of the petroleum reservoir is weak compared to the background EM field generated by an electric dipole transmitter in layered geoelectric structures (Zhdanov 2009) ; thus rendering inversion of CSEM data a problem.

Bhuyian, Landrø et al. (2012) and Shahin, Key et al. (2010) noted that time-lapse CSEM data is achieved by carrying out several repeated surveys over a depleting reservoir at different times with the major aim of detecting and estimating the changes in the pore filling fluid properties. The main aim of CSEM monitoring is to image fluid flow in a reservoir during production since the electrical properties do change with fluid saturation. The monitoring process unlike exploration, is easily carried out and normally inexpensive since; (1) the same equipment used in the exploration are also used during the monitoring; (2) knowledge about the reservoir location and conductivity is acquired prior to monitoring; (3) the receivers being anchored on the seafloor reduces the experimental errors which would otherwise affect the process after subsequent surveys and ensures maximum mapping of the same target. According to Lien and Mannseth (2008), monitoring helps in determining the sensitivity of the CSEM data with respect to changes in conductivity distributions.

For enhanced oil production, brine or gas is injected into the depleted reservoir to displace the remaining oil towards the production well. Here, the main focus will be the detection of the electrical conductivity changes for a horizontal flooding with a two-phase zone separating the saline water and the saturated sediments; thus the reservoir being heterogeneous with varying brine saturations. As more conductive brine is injected into a depleted reservoir, conductivity increases there by decreasing the contrast. As it will be noted in chapter 4, a decrease in conductivity contrast of the reservoir decreases the electric field (an output in this case) indicating the change in the saturation of the hydrocarbon. Therefore, it will be expected that as more brine is injected, the formation resistivity of the reservoir increases. The extent to which the brine has migrated into the reservoir will be detected by the change in the anomalous electric field. With knowledge of the background field (assumed to be time independent) prior to monitoring, any changes into its field will be an indicator for saturation of the reservoir.

1.2 Approximations to Integral Equation

An interaction of the incident field with the scatterer gives rise to an interior electromagnetic field that leads to the generation of an exterior field, which constitutes the scattered electromagnetic field. The determination of the scattered field once the specific parameters of the scatterer and the incident field are given, forms the direct scattering problem (Charalambopoulos, Dassios et al. 2002). Electromagnetic field equations can be solved by several methods of which the integral equation (IE) approach will be discussed at length in the preceding chapters. Alongside the Finite Difference (FD); a very time consuming numerical method, and the Finite Element (FE); a very difficult method to implement, the integral equation forms the basis for the forward modeling (Martin Čuma, Masashi Endo et al. 2008). The integral equation is one of the powerful tools for forward EM numerical modeling and has been used in a wide range of applications such as geophysical prospecting; medical imaging and antenna design (Abubakar and Habashy 2005). One principle advantage of the IE method over the other techniques is that; it only requires the discretization of the anomalous domain. In addition, it is fast and accurate in simulation of the electromagnetic response in models with compact 2D or 3D bodies in a layered background (Zhdanov 2002).

Various integral equation approximations have previously been presented to solve the Maxwell's equations with the main difference lying in the formulation and treatment of their operator matrices in discretized form. These include, the novel EM scattering approximation (Gao, Fang et al. 2003); the quasi-analytical approximation (Zhdanov, Dmitriev et al. 2000); the quasi-linear approximation (Zhdanov, Dmitriev et al. 2000) and; the multi-grid quasi-linear approximation (Martin Čuma, Masashi Endo et al. 2008). Integral equation methods can be applied on various scatterer geometries both regular and irregular having grid cells of different shapes with the cuboid and spherical shapes.

Among these approximations to the integral equation using the Green's function, three approximations; the Born, Extended Born and the T-matrix will be studied and their Matlab implementation done. Solving three-dimensional problems requires the use of the T-matrix approximation and Extended Born that have better accuracy than the Born (Gelius and Tygel 2013). The modeling scheme developed here can be used to model both isotropic and anisotropic 3D EM data. It has been noted that the Born approximation has limited application for solving general 3D electromagnetic problems, though yielding an extremely fast approximate solution for low frequencies and relatively small volumetric contrast (Habashy, Groom et al. 1993).

The T-matrix for the forward modeling of 4D seismic was introduced by Jakobsen (2012) and it is this new approximation to the integral equation for the forward EM modeling that has been discussed in this study for 3D CSEM data. The T-matrix approach is based on a decomposition of an electromagnetic model into a relatively simple background medium and a perturbation. The background field is a very poor estimate for the internal fields of a conducting scatterer in an insulating background medium. The divergent behavior of the Born approximation has been alleviated by the Extended Born approximation (Habashy, Groom et al. 1993, Torres-Verdin and Habashy 1995, Gelius and Tygel 2013) which

produces a finite contribution from the charges to the scattered field in the low frequency limit, and renders it applicable to extremely resistive host media. With different implementation and treatment of results, there is a connection between the Extended Born considered here and that previously introduced (Habashy, Groom et al. 1993, Abubakar and Habashy 2005) and the discussion of Gelius and Tygel (2013).

1.3 Outline of the Thesis

This thesis has been organised into the following chapters;

Chapter 2 gives a background into the electromagnetic theory that forms the basis for this study. An insight into the different electromagnetic methods for propagation of electric currents has been discussed. The relationship between the electrical conductivity, charge and potential difference in isotropic materials has been briefly highlighted. The electromagnetic equations that govern the propagation of waves through the media have been derived as the basis for the integral equation and the approximations considered.

In the chapter 3, the theoretical details for the Born, the Extended Born and the T-matrix approximations are outlined. In addition, the formulation and discretization of the T-matrix and Extended Born approximations to the integral equation for the electric field are done after the formulation of the integral equation representation for the electric field everywhere in space is achieved. The assumptions and limitations of these approaches are also highlighted in this chapter.

Chapter 4 discusses the results obtained from the forward modelling for the T-matrix and the Extended Born approximations in comparison with the Born. Modeling herein, is done on synthetic data from different reservoir geometries to test for the accuracy of these approximations. The effect of the reservoir parameters on these approximations is studied in this chapter and the associated errors.

In Chapter 5, Born inversion has been performed on the forward modeling data obtained by using the Born, T-matrix, and Extended Born approximations. A comparison is done on the inverted data at low, moderate and high contrasts.

Chapter 6 gives a summary of the findings from forward and inverse modeling, the general conclusion from the findings and the way forward for future research. MATLAB codes developed and used in this thesis have been added in the appendex; for forward modeling (*EMforward.m*), inversion (*EMinversion.m*) and the Green's function (*greens.m*). The T-matrix background Green's function for a heterogeneous media though not used is discussed for future studies.

2 Electromagnetic Theory

The marine CSEM survey and theoretical background of electromagnetism have been discussed. This chapter gives an overview of terminologies that are used in electromagnetism.

2.1 Marine CSEM

This method has been historically used in petroleum exploitation. However, of recent it has obtained a lot of application in monitoring of hydrocarbon production and storage of carbon dioxide, appraising of the reservoir and in site licensing. The advantage of this method is that; (1) the sources of the EM field are located near the seafloor close to the target reservoir, which increases the sensitivity and resolution of the method (M.S. Zhdanov 2013); (2) serves as an effective geophysical tool to monitor hydrocarbon during production; (3) supplements seismic methods in validating the background models at a relatively low cost, and; (4) CSEM data has easy integration and interpretation. In marine CSEM survey, the horizontal dipole is towed along the in-line emitting a low frequency signal into the surrounding media (Eidesmo, S. Ellingsrud et al. 2002). There are two extreme source-receiver geometries, that is; 1) at an azimuth of 0^o (the in-line geometry) and; 2) in the orthogonal direction (broadside geometry) as illustrated in Figure 2.1.

The geometry in this study will be considered as an azimuth of zero-degree. Presence of a hydrocarbon causes a decrease in electrical conductivity which gives it a unique character to be easily detected. In the view point with (Eidesmo, S. Ellingsrud et al. 2002, Summerfield, Gale et al. 2005, Constable and Srnka 2007, Zhdanov 2009), the survey geometry is considered to consist of electric receivers that are placed stationary by the concrete anchors on the seabed (figure 2.2). The survey design determines how well the target can be detected and characterized. The energy source consisted of two electrodes in this case; 100m apart towed horizontally generating a horizontal electric dipole (HED) antenna at an elevation of 50m from the seabed. The dipole is assumed to emit a low-frequency signal with peak-to-peak current of 1000 amperes into the surrounding media. An array of stationary seafloor receivers normally record both the amplitude and phase of received signal, directly from the source to receiver, reflected and refracted energy from the subsurface , and the refracted energy from the sea-air interface (Eidesmo, S. Ellingsrud et al. 2002, Johansen, Wicklund et al. 2007). The recorded amplitude and phase from the received signal depend on the resistivity structure beneath the seabed. Electric fields attenuate less in resistive media and an increase in the electric field due to the reservoir can be measured at the seafloor at offsets roughly 2-5 times the depth of the reservoir below the seabed. Depending on the resistivity due to hydrocarbon saturation, the energy from the subsurface will include the energy from the reservoir.

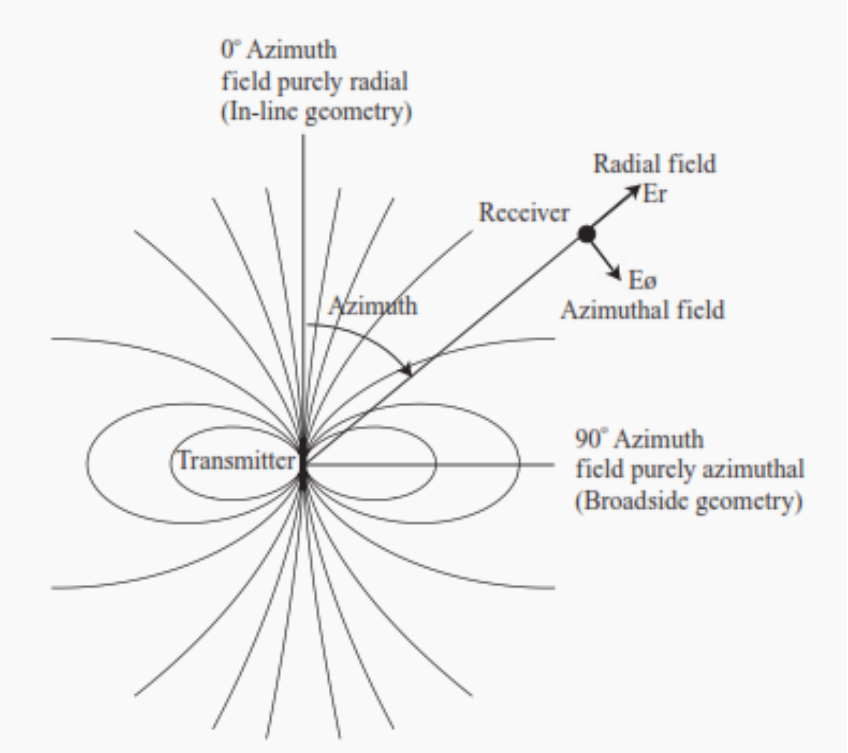

Figure 2.1:*The geometry of CSEM dipole fields. Along the polar axis of the dipole transmitter, the field is purely radial. Along the equatorial axis, the field is purely azimuthal. At other azimuths the received fields are a trigonometric mix of both modes (Constable and Weiss 2006).*

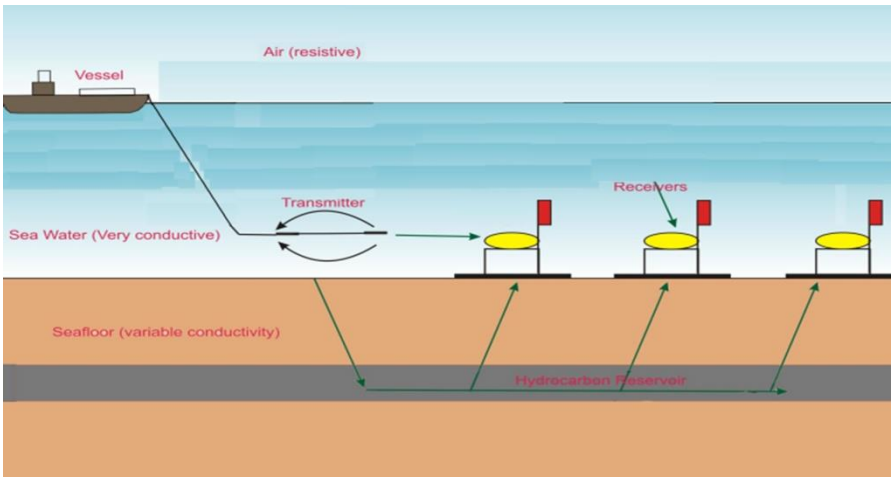

Figure 2.2**:** *Marine CSEM acquisition model with a horizontal transmitter towed approximately 30m above the seabed emitting a periodic pulse up to 1000 A, receivers anchored at the seafloor and the hydrocarbon layer buried several meters in the sediments.(Yahya 2012)*

Ellis and Sinha (2010) noted that the marine CSEM imaging exploits the variation in resistivity between brine saturated and gas/ oil/ hydrate saturated sediments; which gives a better understanding of the pore fluid and water saturation. The ability to understand and control reservoir behavior over the course of production allows for optimization of reservoir performance and production strategies. From the initial applications of EM methods in de-risking exploration and appraisal projects with direct hydrocarbon indication, the CSEM method can be logically extended through reservoir surveillance on the premise of fluid discrimination; in particular, tracking the position of the oil/ water and gas/ water contact.

According to the principle of reciprocity (Wang, Luo et al. 2008), during the inversion the transmission points will be exchanged with observation points. The effect of the reservoir is detectable in mCSEM data when using appropriate frequency and horizontal range from source to receiver was made to be of 7 times the depth of burial of the reservoir used in Gelius and Tygel (2013).

2.2 Electromagnetic Fields

Electromagnetic fields are useful in geophysics due to their interactive nature with the medium through which they propagate (Zhdanov 2009). This interaction can be used to determine certain physical properties of rocks, that is; electrical conductivity $\boldsymbol{\sigma}$, dielectric permittivity $\boldsymbol{\varepsilon}$, and magnetic permeability $\boldsymbol{\mu}$. For forward modeling problem, the operator equation is described by (Zhdanov 2009) as

$$\{\mathbf{E},\mathbf{H}\} = \mathbf{A}^{em}\{\boldsymbol{\sigma},\boldsymbol{\varepsilon},\boldsymbol{\mu}\} \qquad (2.1)$$

where $\mathbf{A}^{em}$ is an operator of the forward electromagnetic problem (non-linear in general). For inverse problem in electromagnetics, the electromagnetic parameters of the media $\boldsymbol{\sigma},\boldsymbol{\varepsilon},\boldsymbol{\mu}$ are determined from $\mathbf{E}$, $\mathbf{H}$ as

$$\{\boldsymbol{\sigma},\boldsymbol{\varepsilon},\boldsymbol{\mu}\} = \left(\mathbf{A}^{em}\right)^{-1}\{\mathbf{E},\mathbf{H}\} \qquad (2.2)$$

Equation (2.2) is non-linear inverse problem making the inversion of electromagnetic data a challenging problem in geophysics (Zhdanov 2002).

The electromagnetic methods are based on the study of the propagation of electric currents and electromagnetic fields in the Earth. There are two methods that can be used;

1) The direct current (D.C) methods or resistivity methods:- these considers injecting an electric current in the earth by a system of current electrodes and measuring the electrical potential with receiver electrodes; where, a low frequency current (<100 Hz) is used, to propagate inside the Earth practically like a direct current (Zhdanov 2002). The D.C surveys are used to determine the resistivity of the rocks. The resistivity of the rock provides information about the mineral content and the physical

structures of rocks, and also about fluids in the rocks. However, D.C survey are limited by their failure to penetrate through resistive formations (Zhdanov 2002).

2) Electromagnetic induction methods:- these are based on transient field which overcomes the limitation above since transient fields easily propagates through resistors. This method in addition to resistivity provides information about magnetic permeability $\boldsymbol{\mu}$, and dielectric constant $\boldsymbol{\varepsilon}$. Zhdanov (2002) indicates that this method can be used for ground, airborne, sea bottom and borehole observations. In this type, the receivers measures the total field formed by the primary signal in the transmitter and a scattered signal from the internal structures of the Earth.

2.2.1 Amplitude and Phase

The amplitude of the secondary field is measured usually by expressing it as a percentage of the theoretical primary field at the receiver or as the resultant of the in-line and the cross-line fields. Phase shift and the time delay in the received field by a fraction of the period, can also be measured and displayed. The second method of presentation of the field is to electronically separate the received field into two components; (1) In-phase (the "real") and, (2) Out-of-phase (the "quadrature" or "imaginary") component with the transmitted field.

In frequency domain electromagnetics, depth and size of the conductor primarily affect the amplitude of the secondary field. The quality of the conductor mainly affects the ratio of in-phase to out-of-phase amplitudes.

2.2.2 Skin Effect

Skin effect is the tendency of an alternating electric current (A.C) to become distributed within a conductor such that the current density is largest near the surface of the conductor, and decreases with greater depths in the conductor. An electric current mainly flows at the "skin" of the conductor, between the outer surface and a level called the *skin depth*. The skin effect is due to opposing eddy currents induced by the changing magnetic field resulting from the alternating current.

In a good conductor, displacement current is negligible in comparison to conduction current, i.e. $\boldsymbol{\sigma} \gg \omega\boldsymbol{\varepsilon}$.

$$\begin{aligned} \mathbf{J}_{total} &= \mathbf{J}_{conduction} + \mathbf{J}_{displacement} \\ \mathbf{J}_{total} &= \boldsymbol{\sigma}\boldsymbol{E} + i\omega\boldsymbol{\varepsilon}\boldsymbol{E} \\ \left|\mathbf{J}_{conduction}\right| &\gg \left|\mathbf{J}_{displacement}\right|, \end{aligned} \qquad (2.3)$$

Given that $\boldsymbol{\sigma} \gg \omega\boldsymbol{\varepsilon}$, the propagation constant within a good conductor may be approximated by the propagation constant as

$$\gamma = \boldsymbol{\alpha} + i\boldsymbol{\beta} = \sqrt{i\omega\boldsymbol{\mu}\left(\boldsymbol{\sigma} + j\omega\boldsymbol{\varepsilon}\right)} \approx \sqrt{i\omega\boldsymbol{\mu}\boldsymbol{\sigma}} = \sqrt{\omega\boldsymbol{\mu}\boldsymbol{\sigma}\angle 90^{0}}$$

$$\gamma = \boldsymbol{\alpha} + i\boldsymbol{\beta} = \sqrt{\frac{\omega\boldsymbol{\mu}\boldsymbol{\sigma}}{2}}\left(1+i\right)$$

$$\boldsymbol{\alpha} = \boldsymbol{\beta} = \sqrt{\frac{\omega\boldsymbol{\mu}\boldsymbol{\sigma}}{2}} = \sqrt{\pi f\boldsymbol{\mu}\boldsymbol{\sigma}} \qquad (2.4)$$

with the real and imaginary parts of the propagation constant, α and β as the attenuation and the phase constants, respectively. The rate of attenuation in a good conductor can be characterized by a distance defined as the skin depth. The attenuation in a good conductor increases with frequency that is; at higher frequencies, the skin depth is smaller which causes the effective resistance of the conductor to increase.

2.2.3 Skin Depth ($\boldsymbol{\delta}$)

The attenuation constant (skin depth) defines the rate of decay of the wave fields as the waves propagate. Skin depth is the distance over which a plane wave is attenuated by a factor of e^{-1} in a good conductor, or as the depth at which flux density and eddy currents have decayed to e^{-1} of their surface value. Thus the decay from the surface to the interior is exponential.

$$\mathbf{E}\left(\mathbf{x}\right) = \mathbf{E}_0 e^{-\boldsymbol{\alpha}\mathbf{x}}$$

$$\mathbf{E}\left(\boldsymbol{\delta}\right) = \mathbf{E}_0 e^{-\boldsymbol{\alpha}\boldsymbol{\delta}}$$

$$\mathbf{E}\left(\boldsymbol{\delta}\right) = \mathbf{E}_0 e^{-1} \qquad (2.5)$$

Thus, $\boldsymbol{\alpha}\boldsymbol{\delta} = 1$

And from (Constable 2010), it then follows from equation (2.5) that

$$\boldsymbol{\delta} = \frac{1}{\boldsymbol{\alpha}} = \frac{1}{\sqrt{\pi f\boldsymbol{\mu}\boldsymbol{\sigma}}} \qquad (2.6)$$

with f is the frequency (Hz), $\boldsymbol{\sigma}$ is the electrical conductivity (S/m), and $\boldsymbol{\mu}$ is absolute magnetic permeability of the conductor. Due to the skin depth effect, very low frequencies (0.05-1 Hz) are applied (S. E. Johansen, H.E.F. Amundsen et al. 2005), if a deep sub-seafloor target must be penetrated. The antenna frequency affects the resolution on the E-field contrast when evaluating models with and models without hydrocarbon. The relationship between any frequency and the maximum depth of detectable reservoirs (Tadiwa, Yahya et al. 2013) can be given by,

$$Z_{max} = 600 - 851.2\ln\left(f\right) \qquad (2.7)$$

where, Z_{max} the maximum depth, and f is the antenna frequency. EM signals are rapidly attenuated in seawater (approximately 551m at 0.3 Ω-m) and seafloor sediments saturated with saline water. These signal pathways will dominate at near source-to-receiver offsets (approximately 3km) (S. E. Johansen, H.E.F. Amundsen et al. 2005).

2.3 Electrical Resistivity

Measuring the electrical resistivity of the subsurface is one of the most powerful prospecting methods in hydrocarbon exploration (Árnason 2010). Subsurface resistivities are controlled by properties of interest like, permeability and porosity, salinity, saturation, and fluid-rock interaction; which to a great extent characterize the reservoir (Johansen, Wicklund et al. 2007). Measurement of electrical resistivity beneath the sea floor plays a crucial role in hydrocarbon exploration and reservoir assessment and development (Tadiwa, Yahya et al. 2013). In interpretation of electric field data measurements at the earth's surface, knowledge of electrical properties of rocks comprising the earth's interior is required. While water-wet sediments, in the over- and under-lying sediments are typically less than a few Ω-m (generally have resistivities in the range 1-5 Ω-m), hydrocarbon-bearing sediments have much higher resistivities of a few tens of Ω-m or higher (30-500 Ω-m) (S. E. Johansen, H.E.F. Amundsen et al. 2005, Tadiwa, Yahya et al. 2013). The electromagnetic methods have the widest conductivity range (of magnitude 10^{32}) in comparison with other common physical properties (Yves Gueguen and palciauskas 1994), and it is this large contrast that makes them powerful tools in the detection of areas of anomalous conductivity.

2.3.1 Ohm's Law

At low frequencies $\left(\omega < 10^3\ Hz\right)$, electrical resistivity, $\boldsymbol{\rho}$ or electrical conductivity, $\boldsymbol{\sigma}$ are the quantities that characterize the electrical charge transport. When a static electric field, $\mathbf{E}$ (V/m) is applied, an electric current density, $\mathbf{J}$ (A/ m^2) is established due to the displacement of the various charged particles. From Yves Gueguen and palciauskas (1994) these are related by the expression

$$\mathbf{J} = \boldsymbol{\sigma}\mathbf{E} = \frac{1}{\boldsymbol{\rho}}\mathbf{E}, \qquad (2.8)$$

that defines the electrical conductivity/resistivity of an isotropic material.
However, it should be noted that the conductivity $\boldsymbol{\sigma}$ and resistivity $\boldsymbol{\rho}$ are intrinsic material properties, independent of the sample geometry. The resistivity $\boldsymbol{\rho}$ (Ω-m) is related to the potential difference $\mathbf{V}$ (V) and current $\mathbf{I}$ (A).This potential difference provide information on the form of subsurface heterogeneities and their electrical properties. The greater the electrical contrast between the hydrocarbon and the heterogeneity, the easier its detection.

2.3.2 Conduction in Solution

Electrical conduction in rocks is mainly through ion movement in pore filling brine. Pore spaces in rocks usually contain waters that contain salts which dissociate totally in solution and can move independently under the influence of an applied electric field (Yves Gueguen and palciauskas 1994). At steady state, the ion velocity, $\boldsymbol{v}$ is given from the Stoke's law; which states that the applied electric force, $q\boldsymbol{E}$ is balanced by the viscous force, $6\pi\eta r\boldsymbol{v}$ exerted by the field on the hydrated ion. The expression relating the electric and the viscous forces is stated from (Yves Gueguen and palciauskas 1994) as;

$$q\boldsymbol{E} = 6\pi\eta r\boldsymbol{v} \qquad (2.9)$$

where η is the viscosity of the water and r is the effective radius of the ion. The ion mobility is given as

$$\boldsymbol{u} = \frac{q}{6\pi\eta\boldsymbol{r}} \qquad (2.10)$$

Since $\boldsymbol{v} = \boldsymbol{uE}$ depends on particle type and its interaction with the medium, the ionic conductivity $\boldsymbol{\sigma}_w$ is given by the relation

$$\boldsymbol{\sigma}_w = nq\boldsymbol{u} = \frac{nq^2}{6\pi\eta\boldsymbol{r}} \qquad (2.11)$$

2.3.3 Archie's Law

With lack of sufficient information on pore microstructure, one heavily relies on the empirical relations between the formation factor and porosity (Yves Gueguen and palciauskas 1994). The resistivity measurements serve as one of the principal methods for estimating fluid saturations in oil-bearing rocks.

$$F = \phi^{-m} \qquad (2.12)$$

Or

$$F = \left(\phi - \phi_o\right)^{-m} \qquad (2.13)$$

Here F is the formation factor, ϕ is the porosity, and m is the cementation exponent being constant for a given rock type but for majority sandstones being close to $m = 2$. The laws (2.12) and (2.13) are the empirical relations which fit the data over a range of porosity: $0.05 \le \phi \le 0.40$ by Yves Gueguen and palciauskas (1994). The resistivity index, RI (unit less) is a function of saturation and pore microstructure expressed by the relation

$$RI = \left(S_w\right)^{-n} = \frac{\rho_t}{\rho_o} \qquad (2.14)$$

where n is saturation exponent approximately constant for a given porous medium. For a given system of fluids, ρ_t and ρ_o are the resistivities of a partially saturated rock and a completely saturated rock with a conducting fluid, respectively.

The electrical resistivity of reservoir rocks is highly sensitive to changes in water saturation. From Archie's law, fluid saturation can accurately be determined through description of the electrical resistivity of rocks as a function of water saturation (S_w), porosity (ϕ), and pore fluid resistivity (ρ_{brine}). All petroleum fluids (oil, condensate, and hydrocarbon gas) are electrically resistive; rendering the Archie's law appropriate for any combination of oil, hydrocarbon gas, and condensate (Yves Gueguen and palciauskas 1994).

2.3.4 Oil and Gas Saturation in Rocks

The resistivity of the reservoir is primarily controlled by the saline brine that fills the rock pores (Vilamajó, Queralt et al. 2013). The resistivity of the storage formation however, is strongly controlled by a resistive fluid when injected into the reservoir. Due to the very low conductivity of oil and natural gas compared to water, increasing the saturation of these fluids will significantly decrease the bulk resistivity (Yves Gueguen and palciauskas 1994). These variations can help to discriminate between fluids. Porosity is a crucial factor in determining resistivity. Saturation, the proportion of oil, gas, water and other fluids in a rock, is a crucial factor in formation evaluation (Jean-Louis Chardac, Mario Petricola et al. 1996). Saturation changes are crucial to fluid flow and must be carefully monitored to optimize reservoir management, and delay gas or water coning (Jean-Louis Chardac, Mario Petricola et al. 1996). Fluid saturation can be assessed indirectly by measuring the resistivity or electrical resistance of the rock layer (Yves Gueguen and palciauskas 1994). From Archie's law

$$\sigma_t = \frac{1}{a}\sigma_w \phi^m s_w^n \qquad (2.15)$$

where a is the tortuosity factor and σ_w is the conductivity of the formation saline water. Yves Gueguen and palciauskas (1994) noted that to determine the saturation S_o (oil) and S_w (water) is one of the most economically important rock physics problems. The product of oil saturation and porosity, $S_o\phi$, is proportional to the volume of oil (or gas) that exists in a reservoir. The relative permeability of oil, which depends on S_o, indicates how rapidly the oil can be extracted.

2.4 Maxwell's Equations

The propagation of electromagnetic waves away from the time-varying sources in form of energy is governed by Maxwell's equations. These summarize the connection between the electric and magnetic fields, charges, currents, and the coupling between the electric and

magnetic field quantities. The basis of the theory of electromagnetic fields studied by geophysicists is provided by the macro-electrodynamics equations, i.e., Maxwell's equations.

2.4.1 Electromagnetic Field Equations

An electromagnetic wave equation is a second order partial differential equation that describes the nature of electromagnetic wave propagation in a given medium or vacuum. These wave equations are derived from the Maxwell's equations. Variation in the electric field generates the magnetic field, vice versa. These equations hold for any material and at any spatial location in an arbitrary (x, y, z) coordinate system. The generalized forms of Maxwell's equations are summarized below.

1) The generalized Ampere's law, which states that both conduction currents and displacement currents $\frac{\partial \boldsymbol{D}}{\partial t}$ generate the magnetic field.

$$\nabla \times \mathbf{H} = \mathbf{J} + \mathbf{J}^e + \frac{\partial \boldsymbol{D}}{\partial t} \qquad (2.16)$$

2) Faraday's law of electromagnetic induction, which states that the time-varying magnetic field is always accompanied by a spatially varying, non-conservative electric field. That is when the magnetic flux changes, an electric field is created. This leads to the Maxwell- Faraday equation

$$\nabla \times \mathbf{E} = -\frac{\partial \boldsymbol{B}}{\partial t} \qquad (2.17)$$

3) Using the Gauss's law for electrostatics which states that total magnetic flux through a closed surface is zero, the 3rd equation is obtained as

$$\nabla \cdot \mathbf{B} = 0 \qquad (2.18)$$

4) Coulomb's law which states that electric charges generate the electric field, forms the fourth Maxwell's equation as

$$\nabla \cdot \mathbf{D} = \boldsymbol{q} + \boldsymbol{q}^e \qquad (2.19)$$

where **E** and **D** are the vectors of electric field; **H** and **B** are vectors of magnetic field. **J** is the conduction current density and $\mathbf{q}$ is the spatial density of free electronic charges. $\mathbf{J}^e$ and $\boldsymbol{q}^e$ are densities of extraneous electric currents and charges in the transmitter. The electric currents and charges are inter-related by the continuity equation

$$\nabla \cdot \left(\mathbf{J} + \mathbf{J}^e \right) = -\frac{\partial \left(\boldsymbol{q} + \boldsymbol{q}^e \right)}{\partial t} \qquad (2.20)$$

Equation (2.20) expresses the fact that the divergence of electric currents from an infinitesimal volume is equal to the rate of decrease of electric charge density with time.

Equations (2.16) – (2.19) are supplemented by the constitutive relations reflecting the electromagnetic properties for linear and isotropic media. These relations are; $\boldsymbol{D} = \varepsilon \boldsymbol{E}$ and $\boldsymbol{B} = \mu \boldsymbol{H}$, with ε and μ as the dielectric constant and magnetic permeability of the medium, respectively. The free space dielectric constants are given by, $\varepsilon_o = 8.85 \times 10^{-12}$ (F/m) and $\mu_o = 4\pi \times 10^{-7}$ (H/m). The conduction current density however is expressed in terms of electric field by the Ohm's law; $\mathbf{J} = \sigma \mathbf{E}$ which is the third constitutive relation.

2.4.2 Field Equations in the Frequency Domain

Maxwell's equations being linear in nature, it then follows that a field varying arbitrarily in time can be represented as a sum of harmonic fields whose time dependence is expressed by a factor $e^{-i\omega t}$, where $\boldsymbol{i} = \sqrt{-1}$, ω is the angular frequency and t is the time (Zhdanov 2009). For a monochromatic field, equations (2.16) – (2.19) take the form;

$$\begin{aligned} \nabla \times \mathbf{H} &= \boldsymbol{\sigma} \mathbf{E} + \mathbf{J}^e \\ \nabla \times \mathbf{E} &= i\omega \mathbf{B} \\ \nabla \cdot \mathbf{B} &= 0 \\ \nabla \cdot \mathbf{D} &= \boldsymbol{q} + \boldsymbol{q}^e \end{aligned} \qquad (2.21)$$

$\boldsymbol{\sigma} = \sigma - i\omega\boldsymbol{\varepsilon}$ is the complex electrical conductivity of the medium. By separating the Maxwell's equations (2.21), using the constitutive relations,

$$\boldsymbol{\mu} \nabla \times \left(\frac{1}{\boldsymbol{\mu}} \nabla \times \mathbf{E} \right) - \left(i\omega\boldsymbol{\sigma}\boldsymbol{\mu} + \omega^2 \boldsymbol{\mu}\boldsymbol{\varepsilon} \right) \mathbf{E} = i\omega \boldsymbol{\mu} \mathbf{J}^e \qquad (2.22)$$

And

$$\boldsymbol{\sigma} \nabla \times \left(\frac{1}{\boldsymbol{\sigma}} \nabla \times \mathbf{H} \right) - i\omega\boldsymbol{\sigma}\boldsymbol{\mu}\mathbf{H} = \boldsymbol{\sigma} \nabla \times \left(\frac{1}{\boldsymbol{\sigma}} \mathbf{J}^e \right) \qquad (2.23)$$

Zhdanov (2002) considers a homogeneous domain of extraneous currents or extraneous charges, that is; $\mathbf{J}^e = 0$ and $\boldsymbol{q}^e = 0$. Then it follows that,

$$\nabla^2 \mathbf{E} + k^2 \mathbf{E} = 0, \qquad (2.24)$$

And

$$\nabla^2 \mathbf{H} + k^2 \mathbf{H} = 0 \qquad (2.25)$$

Equations (2.24) and (2.25) are the Helmholtz equations where $k^2 = -(i\omega\boldsymbol{\sigma}\boldsymbol{\mu} + \omega^2 \boldsymbol{\mu}\boldsymbol{\varepsilon})$.

3 Green's Function Methods

This section deals with integral equation and the Green's function formulation which are then used in the derivations of the approximations. For modelling, the feasibility of the Born ,EBA and TMA pproximations is done by descritization for their implementation in MATLAB. The inversion scheme to be used in the proceeding chapters is also discussed.

3.1 Green's Function

This is an integral kernel that is used to solve linear inhomogeneous differential equations with boundary conditions by expressing the solution in terms of an integral equation. The electromagnetic field in the presence of macroscopic dielectrics is governed by an inhomogeneous vector Helmholtz equation (Chew 1999). From equation (2.22), it then reduces to

$$\nabla\times\nabla\times\mathbf{E}(\mathbf{r})-k^2\mathbf{E}(\mathbf{r})=\mathbf{J}^e(\mathbf{r}) \qquad (3.1)$$

with $\mathbf{E}(\mathbf{r})\to\mathbf{0}$ as $\mathbf{r}\to\infty$.

Using the Green's function formulation, the solution to the Helmholtz equation (3.1) can be given as

$$\mathbf{E}(\mathrm{r})=\int_v dv\mathbf{G}(\mathbf{r},\mathbf{r}')\mathbf{J}(\mathbf{r}'), \qquad (3.2)$$

where the Green's tensor is a solution to

$$\nabla\times\nabla\times\mathbf{G}(\mathbf{r},\mathbf{r}')-k^2\mathbf{G}(\mathbf{r},\mathbf{r}')=\delta(\mathbf{r}-\mathbf{r}')\mathbf{I}. \qquad (3.3)$$

It is also true that $\mathbf{G}(\mathbf{r},\mathbf{r}')\to\mathbf{0}$, as $|\mathbf{r}-\mathbf{r}'|\to\infty$. Here, $\mathbf{r}=(\mathrm{r}_1,\mathrm{r}_2,\mathrm{r}_3)$ and $\mathbf{r}'=(\mathrm{r}'_1,\mathrm{r}'_2,\mathrm{r}'_3)$ are the source and observation points, respectively. For an infinitely extended, homogeneous dielectric (Bulk medium), the Green's tensor is a solution to

$$\nabla\times\nabla\times\mathbf{G}^b(\mathbf{r},\mathbf{r}')-k^2\mathbf{G}^b(\mathbf{r},\mathbf{r}')=\delta(\mathbf{r}-\mathbf{r}')\mathbf{I} \qquad (3.4)$$

Using the identity $\nabla\times\nabla\times=\nabla\nabla.-\Delta\mathbf{I}$, reducing the Helmholtz vector to scalar equation is done by taking the divergence of equation (3.4) (Chew 1999).

$$\nabla.\mathbf{G}^b(\mathbf{r},\mathbf{r}')=-\frac{1}{k^2}\nabla\delta(\mathbf{r}-\mathbf{r}') \qquad (3.5)$$

Expanding equation (3.4), and substituting equation (3.5) using the identity above,

$$\nabla\left[-\frac{1}{k^2}\nabla\delta(\mathbf{r}-\mathbf{r}')\right]-\left(\Delta+k^2\right)\mathbf{G}^b(\mathbf{r},\mathbf{r}')=\delta(\mathbf{r}-\mathbf{r}')\mathbf{I}\,, \qquad (3.6)$$

This reduces to

$$\left(\Delta+k^2\right)\mathbf{G}^b(\mathbf{r},\mathbf{r}')=-\left[\mathbf{I}-\frac{1}{k^2}\nabla\nabla\delta(\mathbf{r}-\mathbf{r}')\right]\delta(\mathbf{r}-\mathbf{r}')\,. \qquad (3.7)$$

For a homogeneous background, the Green's function in vector form is related to that in the scalar form by writing (Habashy, Groom et al. 1993, Chew 1999)

$$\mathbf{G}^b(\mathbf{r},\mathbf{r}')=\left[\mathbf{I}-\frac{1}{k^2}\nabla\nabla\delta(\mathbf{r}-\mathbf{r}')\right]\mathrm{g}(\mathbf{r},\mathbf{r}')\,, \qquad (3.8)$$

where the scalar Green's function, *g* satisfies the scalar Helmholtz equation,

$$\left(\Delta+k^2\right)\mathrm{g}(\mathbf{r},\mathbf{r}')=-\delta(\mathbf{r}-\mathbf{r}')\,, \qquad (3.9)$$

subject to appropriate boundary conditions; where,

$$\mathrm{g}(\mathbf{r},\mathbf{r}')=\frac{e^{ik|\mathbf{r}-\mathbf{r}'|}}{4\pi|\mathbf{r}-\mathbf{r}'|} \qquad (3.10)$$

At infinity, consider $\mathrm{Im}\,k>0$. Substituting equation (3.10) into equation (3.8) (Chew 1999)

$$\mathbf{G}^b(\mathbf{r},\mathbf{r}')=\frac{1}{4\pi}\left[\mathbf{I}-\frac{1}{k^2}\nabla\nabla\delta(\mathbf{r}-\mathbf{r}')\right]\frac{e^{ik|\mathbf{r}-\mathbf{r}'|}}{|\mathbf{r}-\mathbf{r}'|}\,, \qquad (3.11)$$

$$\mathbf{G}^b(\mathbf{r},\mathbf{r}')=\frac{\delta(\boldsymbol{\rho})\mathbf{I}}{3k^2}+\frac{e^{ik\rho}}{4\pi k^2\rho^3}\left\{\left[1-ik\rho-(k\rho)^2\right]\mathbf{I}-\left[3-3ik\rho-(k\rho)^2\right]\mathbf{e}_\rho\mathbf{e}_\rho\right\} \qquad (3.12)$$

where $\boldsymbol{\rho}=\mathbf{r}-\mathbf{r}'$, $\rho=|\boldsymbol{\rho}|$, $\mathbf{e}_\rho=\boldsymbol{\rho}/\rho$ and $\Delta(1/\mathrm{r})=4\pi\delta(\mathbf{r})$. Equation (3.12) is implemented in MATLAB by Stav (2010). Once the Green's function in the scatterer and the background is implemented, then the remaining part can easily be determined in order to calculate the integral equation approximations.

3.1.1 The Singularity of Green's Function

It is imperative to discuss the singularity of the Green's function prior to formulating the EBA and the TMA. The Green's function $\mathbf{G}(\mathbf{r},\mathbf{r}')$ need to be redefined at points when $\mathbf{r}\to\mathbf{r}'$ (singular points). Inspecting equation (3.11), Kahnert (2003) shows that,

$$\mathbf{G}^b(\mathbf{r},\mathbf{r}')\to\mathrm{O}(|\mathbf{r}-\mathbf{r}'|^{-3})\,, \qquad (3.13)$$

when a second derivative at points $\mathbf{r} \to \mathbf{r}'$ is computed. Therefore, the volume integral (equation 3.2) needs to be performed with care due to the singularity of the free space- dyadic Green's function.

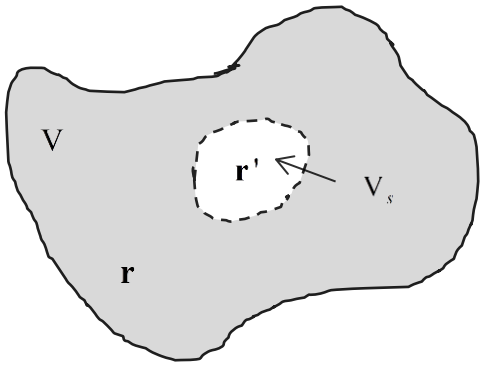

Figure 3.1: *An illustration of the scattering field embedded in the background with* V_s *as an arbitrary volume inside V and containing observation point* $\mathbf{r}'$. *The volume element V is very small compared to the wave length.*

The volume integral over V can then be obtained **(**Kahnert 2003) by considering the long wave approximation as,

$$\int_V d\mathbf{r}'\mathbf{G}(\mathbf{r},\mathbf{r}')\mathbf{J}(\mathbf{r}') = \left[\mathbf{M} - \frac{1}{k_o^2}\mathbf{L}\right]\mathbf{J}(\mathbf{r}), \qquad (3.14)$$

$$\mathbf{M} = \int_V d\mathbf{r}'\left[\mathbf{G}^b(\mathbf{r},\mathbf{r}') - \mathbf{G}^s(\mathbf{r},\mathbf{r}')\right], \qquad (3.15)$$

$$\mathbf{L} = \oint_{\partial v} d^2r'\hat{n}.\left[\frac{\mathbf{r}-\mathbf{r}'}{4\pi|\mathbf{r}-\mathbf{r}'|^3}\right], \qquad (3.16)$$

Where

$$\mathbf{G}^s(\mathbf{r},\mathbf{r}') = \frac{1}{k_o^2}\nabla\nabla\frac{1}{4\pi|\mathbf{r}-\mathbf{r}'|}, \qquad (3.17)$$

leads to all the terms being regular. For weaker interactions as in TMA, equation (3.15) tends to zero implying that equation (3.14) reduces to,

$$\int_V d\mathbf{r}'\mathbf{G}(\mathbf{r},\mathbf{r}')\mathbf{J}(\mathbf{r}') = -\frac{1}{k_o^2}\mathbf{L}\mathbf{J}(\mathbf{r}), \qquad (3.18)$$

From equation (3.18) and (3.12), for singularity, the second term in equation (3.12) will go faster to zero than the first term. Therefore, the Green's function along the diagonal will be implemented as,

$$\mathbf{G}(\mathbf{r},\mathbf{r}') = -\frac{\delta(\rho)\mathrm{I}}{3k_o^2} = -\frac{\delta(\rho)\mathrm{I}}{3\left(\sigma^b + i\omega\varepsilon\right)} = -\frac{1}{3\sigma^b}, \text{ for } \mathbf{r} = \mathbf{r}' \qquad (3.19)$$

Equation (3.19) is consistent with approximating the t-matrix for multiple scattering of EM waves (Jakobsen 2012); as the frequency independent model parameter, t in each grid cell by Stav (2010).

3.2 Integral Equation Formulation

To derive the integral equation, the Green's function technique is usually applied. When conductivity and electric field are assumed to be fixed in a given cell, the discretization of the integral equation yields a linear system of equations. While using the integral equation, the conductivity distribution is divided into the background conductivity for calculation of the Green's function, and the anomalous conductivity within the domain of integration, (Black and Zhdanov 2010). The solution to the forward problem is then computed through three distinct steps (Zhdanov 2002, Martin Čuma, Masashi Endo et al. 2008); (1) calculation of the background fields induced on the receivers by the response of the homogeneous background; (2) calculation of the anomalous fields induced in the domain of interests, and; (3) calculation of fields on the receivers induced by the anomalous fields in the domain. The resulting field on the receivers is the sum of the background field from step 1 and anomalous field from step 3, (Martin Čuma, Masashi Endo et al. 2008).

Assuming the scatterer inside a background medium which is not necessarily homogeneous, the scattering from the object is described by a volume distribution of currents, $\mathbf{J}^a(\mathbf{r})$ induced inside the scatterer. From Maxwell's equations and the use of the constitutive relations $\mathbf{D}(\boldsymbol{r}) = \varepsilon(\boldsymbol{r})\mathbf{E}(\boldsymbol{r})$ and $\mathbf{J}(\boldsymbol{r}) = \boldsymbol{\sigma}(\boldsymbol{r})\mathbf{E}(\boldsymbol{r})$, it then follows that

$$\nabla\times\mathbf{H}(\boldsymbol{r}) = \mathbf{J}(\boldsymbol{r}) + \mathbf{J}^a(\boldsymbol{r}) + i\omega\mathbf{D}(\boldsymbol{r})$$

$$\nabla\times\mathbf{H}(\boldsymbol{r}) = \left[\boldsymbol{\sigma}(\boldsymbol{r}) + i\omega\varepsilon(\boldsymbol{r})\right]\mathbf{E}(\boldsymbol{r}) + \mathbf{J}^a(\boldsymbol{r}) \qquad (3.20)$$

From the Faraday's law in frequency domain,

$$\nabla\times\mathbf{E}(\boldsymbol{r}) = -i\omega\mu_o\mathbf{H}(\boldsymbol{r}) \qquad (3.21)$$

By finding the divergence of equation (3.21),

$$\nabla\times\nabla\times\mathbf{E}(\boldsymbol{r}) = -i\omega\mu_o\nabla\times\mathbf{H}(\boldsymbol{r}) \qquad (3.22)$$

Decoupling of the Maxwell's equations (3.20) and (3.22) gives a new equation that depends only on the electric field, which in anisotropic media is given by,

$$\nabla\times\nabla\times\mathbf{E}_i(\boldsymbol{r})-\mu_o\omega^2\left[\varepsilon(\boldsymbol{r})-i\frac{\sigma(\boldsymbol{r})}{\omega}\right]\mathbf{E}_i(\boldsymbol{r})=-i\omega\mu_o\mathbf{J}_i^q(\boldsymbol{r}) \quad (3.23)$$

Then equation (3.23) can be written in a condensed form as, $\mathbf{L}\left[\mathbf{E}_i(\boldsymbol{r})\right]=-i\omega\mu_o\mathbf{J}_i^q(\boldsymbol{r})$

where $\mathbf{L}=\nabla\times\nabla-\mu_o\omega^2\left[\varepsilon(\boldsymbol{r})-i\frac{\sigma(\boldsymbol{r})}{\omega}\right]$ is an operator acting upon the electric field $\mathbf{E}(\mathbf{r})$ and the bracket is the spatial variation in the medium properties. Therefore the solution for equation (3.23) is found by casting it in an integral form where the dyadic Green's tensor is introduced

$$\mathbf{L}(\mathbf{r})\left[\mathbf{G}_{ij}(\mathbf{r},\mathbf{r}')\right]=-\mathbf{I}\delta_{ij}(\boldsymbol{r}-\boldsymbol{r}') \quad (3.24)$$

where $\mathbf{I}$ is the dyadic identity (unity tensor). The anisotropic conductivity contrast between a hydrocarbon filled reservoir and background model, is given by

$$\Delta\boldsymbol{\sigma}_{jk}(\boldsymbol{r})=\boldsymbol{\sigma}_{jk}(\boldsymbol{r})-\boldsymbol{\sigma}_{jk}^b(\boldsymbol{r}) \quad (3.25)$$

where $\boldsymbol{\sigma}_{jk}(\boldsymbol{r})$ and $\boldsymbol{\sigma}_{jk}^b(\boldsymbol{r})$ are the conductivities of the reservoir and the background model, respectively. The anomalous electric field is given by second term in the Lippmann-Schwinger equation (for $\mathbf{r},\ \mathbf{r}'\in\mathbf{V}$), from a singular inhomogeneous vector Fredholm integral equation of the second order. The anisotropic electric field in all receiving positions (receivers) is calculated from

$$\mathbf{E}_i(\boldsymbol{r})=\mathbf{E}_i^b(\boldsymbol{r})+i\omega\mu_o\int_V\mathbf{G}_{ij}(\boldsymbol{r},\boldsymbol{r}')\Delta\boldsymbol{\sigma}_{jk}(\boldsymbol{r}')\mathbf{E}_k(\boldsymbol{r}')d\boldsymbol{r}',\ \mathbf{r}\notin\boldsymbol{V} \quad (3.26)$$

where $\mathbf{E}_i^b(\boldsymbol{r})$ is the background field that can be calculated for a known source $\mathbf{J}_i^b(\boldsymbol{r})$. The second term of equations (3.26) for both internal and external points can be recast in the form that separates the scattered field into inductive (due to the vector potential) and galvanic (due to scalar potential) terms. From equation (3.26), the total field is represented as the sum of the background field $\mathbf{E}_i^b(\boldsymbol{r})$ and the scattered field (the integral term). The scattered field is generated by the scattering currents and/or charges induced inside the scatterer by the interaction of the total electric field $\mathbf{E}_i(\boldsymbol{r})$ (Habashy, Groom et al. 1993).

3.3 The Born Approximation

The Born Approximation is widely used in solving scattering problems in acoustics, electrodynamics, electromagnetics and quantum mechanics. The Born approximation is adopted to avoid solving the super-large system of linear equations for the full integral equation algorithm (Wang, Luo et al. 2008) and also to increase the speed of modeling. Born approximation has a wide applicability both for inverse and forward scattering problems in

electromagnetics. This approach considers the total electric field in the integral terms being approximated by the background field (i.e. the field excited in the absence of the conductivity contrast) and also neglects multiple scattering within the scatterer (Abubakar and Habashy 2005). The Born gives a representation of electric field that is linear in $\mathbf{Q}_{jk}(\mathbf{r})$, where $\mathbf{Q}_{jk}(\mathbf{r}) = i\omega\mu_o \Delta\boldsymbol{\sigma}_{jk}(\boldsymbol{r})$ is the change in the material properties from the background medium. The born approximation assumes that the anomalous electric field inside the anomalous domain is zero (Wang, Luo et al. 2008) and multiple scattering within the scatterer are neglected. Typically, these series are either divergent or very slowly convergent for large contrasts. To analyze the convergence, a dimensionless contrast defined as

$$\delta_{jk} = \frac{1}{\left|k^2\right|} \max\left|\mathbf{Q}_{jk}(\mathbf{r})\right| \qquad (3.27)$$

By neglecting the displacement currents, equation (3.27) reduces to (Abubakar and Habashy 2005, Gao, Abubakar et al. 2010);

$$\delta_{jk} = \frac{\sigma_{jk}^{max} - \sigma_{jk}^{b}}{\sigma_{jk}^{b}} \qquad (3.28)$$

If the anomalous field is negligibly small inside V, in comparison with the background field, the conventional Born approximation $\mathbf{E}_i^b(\boldsymbol{r})$ for the anomalous field can be obtained from the first term in the solution of equation (3.26), as

$$\mathbf{E}_i(\boldsymbol{r}) \approx \mathbf{E}_i^b(\boldsymbol{r}) \qquad (3.29)$$

Therefore,

$$\mathbf{E}_i(\boldsymbol{r}) = \int_V \mathbf{G}_{ij}^b(\mathbf{r},\mathbf{r}')\Delta\boldsymbol{\sigma}_{jk}(\mathbf{r}')\mathbf{E}_k(\mathbf{r}')d\boldsymbol{r}' \qquad (3.30)$$

The approximation in equation (3.30) is only valid for small conductivity contrasts between background media and the scatterer, for a relatively small inhomogeneity and at low frequencies (Zhdanov 2009).

3.3.1 Discretization of the Born Approximation

In practice, forward modeling and inversion of electromagnetic data involves the use of discrete data points and model parameters. The integral equation for the anomalous field in component form (Stav 2010) can be written as

$$\Delta E_i(\boldsymbol{r}) = \int_V G_{ij}(\boldsymbol{r},\boldsymbol{r}')\Delta\sigma_{jk}(\boldsymbol{r}')E_k(\boldsymbol{r}')d\boldsymbol{r}' \qquad (3.31)$$

For $i, j = x, y, z = 1, 2, 3$.

For an isotropic material $\Delta\boldsymbol{\sigma}_{jk}(\mathbf{r}') = \delta_{jk}\Delta\boldsymbol{\sigma}(\mathbf{r}')$, equation (3.31) can be re-written as (Stav 2010)

$$\Delta E_i(\boldsymbol{r}) = \int_V G_{ij}(\boldsymbol{r},\boldsymbol{r}')\, E_j(\boldsymbol{r}')\, \Delta\boldsymbol{\sigma}(\boldsymbol{r}')\, d\boldsymbol{r}' \qquad (3.32)$$

$$\Delta E_i(\boldsymbol{r}) = \int_V G_{ij}(\boldsymbol{r},\boldsymbol{r}')\, E_j(\boldsymbol{r}',\boldsymbol{r}'')\, \Delta\boldsymbol{\sigma}(\boldsymbol{r}'')\, d\boldsymbol{r}' d\boldsymbol{r}''$$

And

$$\int E_j(\boldsymbol{r}')d\boldsymbol{r}' = \int E_j(\boldsymbol{r}'')\delta(\boldsymbol{r}'-\boldsymbol{r}'')\, d\boldsymbol{r}' d\boldsymbol{r}'' = \int E_j(\boldsymbol{r}',\boldsymbol{r}'')\, d\boldsymbol{r}' d\boldsymbol{r}'' \qquad (3.33)$$

It follows from equation (3.32) that the discretization integral can be solved by summing over all grid cells (Stav 2010).

$$\Delta E_i^p = G_{ij}^{pq} E_j^{qr} \Delta\sigma^r \Delta V \qquad (3.34)$$

with $\Delta\mathbf{V}$ as the volume of each grid cell and indices $p = 1, \ldots, M$; $q, r = 1, \ldots, N$ where M is the number of receivers and N the number of model parameters or grid cells. The electric field from equation (3.34) can be expressed by summing over the repeated indices (Stav 2010). By letting indices $i, p \rightarrow I$, and $j, q \rightarrow J$, that is;

$$\mathrm{I} = (i-1)\mathrm{M} + p \qquad (3.35)$$

$$\mathrm{J} = (j-1)\mathrm{N} + q \qquad (3.36)$$

In discretized form, the Greens function is represented by two indices and therefore takes the form $G_{ij}^{pq} \rightarrow G_{IJ}$, which in implementation also considers the volume ΔV of the grid cells forming the scatterer. In the discretized notation, equation(3.34) reduces to (Stav 2010)

$$\Delta E_I = G_{IJ} E_J^r \Delta\sigma^r \qquad (3.37)$$

3.4 The Extended Born Approximation

Habashy, Groom et al. (1993) developed the Extended-Born technique to improve the Born-approximation and its limitations. This technique replaces the total field in the integral equation (2.51) not by the background field, like in the Born approximation, but now considering its projection onto the scattering tensor $\Gamma(\mathbf{r}')$. The method sufficiently assumes a smooth spatial variation of the internal electric field and the total field inside the object (Song and Liu 2004). It improves the ability to accurately simulate the internal electric field $\mathbf{E}_i(\boldsymbol{r}')$ for a given conductivity distribution without having to invert the large, often full, stiffness matrix resulting from solving the 3D integral equation schemes (Abubakar and Habashy 2005). The total electric field in the interior of the scatterer is considered to be the result of the application of the depolarization tensor on to the incident electric field. Therefore, it is important to determine the depolarization tensor in order to allow the replacement of the integral equations for the interior fields by integral representations of these fields (Charalambopoulos, Dassios et al. 2002). According to Charalambopoulos, Dassios et al.

(2002), the depolarizing dyadic strongly depends on the geometrical;-the shape of the scatterer, and the physical;-low frequency regime characteristics of the scatterer. After the construction of the depolarization dyadic, the next step is to extend the calculations to obtain the corresponding results (Charalambopoulos, Dassios et al. 2002).

3.4.1 Formulation of the Extended Born Approximation

The Extended Born approximation is based on; (1) considering a homogeneous and isotropic medium permitting the propagation of electromagnetic waves; (2) recognizing that for interior points, $\boldsymbol{r} \in \boldsymbol{V}$, a dominant contribution to the integral in equation (3.26) results from scattering points which are in the neighborhood of the observation point $\boldsymbol{r}' = \boldsymbol{r}$ since the Green's tensor $\mathbf{G}^b(\mathbf{r},\mathbf{r}')$ exhibits a singularity or peak at that point (Habashy, Groom et al. 1993, Torres-Verdin and Habashy 1995, Zhdanov 2002, Abubakar and Habashy 2005) Considering the basic integral equation of 3D electromagnetic forward modeling equation (3.26) and neglecting the $i\omega\mu_o$ on the second term, the integral equation for the data is re-written as

$$\mathbf{E}_i(\boldsymbol{r}) = \mathbf{E}_i^b(\boldsymbol{r}) + \int_V \mathbf{G}_{ij}^b(\boldsymbol{r},\boldsymbol{r}')\Delta\boldsymbol{\sigma}_{jk}(\boldsymbol{r}')\mathbf{E}_k(\boldsymbol{r}')d\boldsymbol{r}' \qquad (3.38)$$

This equation however, is integrable since $\mathbf{E}_i(\boldsymbol{r}') - \mathbf{E}_i(\boldsymbol{r})$ vanishes as $\boldsymbol{r}' \to \boldsymbol{r}$ and $\mathbf{G}_{ij}^b(\mathbf{r},\mathbf{r}')$ is singular in this scenario given by equation (3.19). Considering the scattering domain, equation (3.38) is modified to take the form

$$\mathbf{E}_i(\boldsymbol{r}') = \mathbf{E}_i^b(\boldsymbol{r}') + \int_V \mathbf{G}_{ij}^b(\boldsymbol{r}',\boldsymbol{r}'')\Delta\boldsymbol{\sigma}_{jk}(\boldsymbol{r}'')\mathbf{E}_k(\boldsymbol{r}'')d\boldsymbol{r}'' \qquad (3.39)$$

For the different points in the scattering domain; $\mathbf{E}_i(\boldsymbol{r}') \approx \mathbf{E}_k(\boldsymbol{r}'')$. By using this condition in equation (3.39) gives

$$\mathbf{E}_i(\boldsymbol{r}') = \mathbf{E}_i^b(\boldsymbol{r}') + \int \mathbf{G}_{ij}^b(\mathbf{r}',\mathbf{r}'')\Delta\boldsymbol{\sigma}_{jk}(\mathbf{r}'')\mathbf{E}_k(\mathbf{r}')d\mathbf{r}'' \qquad (3.40)$$

The electric field in the scattering domain from equation (3.40) can then be obtained as

$$\mathbf{E}_i(\boldsymbol{r}') = \mathbf{E}_i^b(\boldsymbol{r}') + \lambda_{ik}(\mathbf{r}')\mathbf{E}_k(\mathbf{r}') \qquad (3.41)$$

$\lambda(\mathbf{r}')$ is a tensor that can be explicitly written as

$$\lambda_{ik}(\mathbf{r}') = \int \mathbf{G}_{ij}^b(\mathbf{r}',\mathbf{r}'')\Delta\boldsymbol{\sigma}_{jk}(\mathbf{r}'')d\mathbf{r}'' \qquad (3.42)$$

And according to (Torres-Verdin and Habashy 1995, Zhdanov 2002, Song and Liu 2004) equation (3.42) is independent of the illuminating sources and is a nonlinear function of the anomalous conductivity distribution. By re-arranging (3.41),

$$\left[\mathbf{I} - \lambda_{ik}(\mathbf{r}')\right]\mathbf{E}_k(\boldsymbol{r}') = \mathbf{E}_i^b(\boldsymbol{r}') \qquad (3.43)$$

The well-known EBA (Gao, Fang et al. 2003, Abubakar and Habashy 2005) assumes sufficiently smooth spatial variations of the internal electric field $\mathbf{E}(\mathrm{r})$ with the total field inside the object expressed mathematically via a nonlinear transformation approximated as

$$\mathbf{E}_k\left(\boldsymbol{r}'\right) \approx \boldsymbol{\Gamma}_{ki}\left(\mathbf{r}'\right)\mathbf{E}_i^b\left(\boldsymbol{r}'\right), \quad \forall \mathbf{r} \in \mathbf{V} \tag{3.44}$$

with $\boldsymbol{\Gamma}_{ki}\left(\mathbf{r}'\right)$ known as the depolarizing tensor that is defined as

$$\boldsymbol{\Gamma}_{ki}\left(\mathbf{r}'\right) = \left[\mathbf{I} - \lambda_{ik}(\mathbf{r}')\right]^{-1} \tag{3.45}$$

It should be noted that the unknown transformation $\boldsymbol{\Gamma}_{ki}\left(\mathbf{r}'\right)$ is a complicated function of the field quantities and object properties. However, such a nonlinear transformation may be simplified as a linear one, that is; $\mathbf{E}_i\left(\boldsymbol{r}\right) \approx \mathbf{E}_i^b\left(\boldsymbol{r}\right)$ considering that the Green's function $\mathbf{G}_{ij}^b\left(\mathbf{r},\mathbf{r}'\right)$ is singular when $\mathbf{r}' \to \mathbf{r}$ and falls off rapidly for larger $\left|\mathbf{r}'-\mathbf{r}\right|$. In the well-known EBA, such scattering tensor is approximated by a source-independent tensor (Song and Liu 2004). Substituting equation (3.44) into equation (3.43) yields the Extended-Born Approximation for the electric fields computed outside the domain V.

$$\mathbf{E}_i\left(\boldsymbol{r}\right) = \mathbf{E}_i^b\left(\boldsymbol{r}\right) + \int_V \mathbf{G}_{ij}^b\left(\mathbf{r},\mathbf{r}'\right)\Delta\boldsymbol{\sigma}_{jk}\left(\mathbf{r}'\right)\boldsymbol{\Gamma}_{ki}\left(\mathbf{r}'\right)\mathbf{E}_i^b\left(\boldsymbol{r}'\right)d\boldsymbol{r}' \tag{3.46}$$

3.4.2 Discretization of the Extended-Born Approximation

Considering the Integral Equation form (3.46) for the electric field, the challenge is on solving for the depolarizing tensor $\boldsymbol{\Gamma}_{ki}\left(\mathbf{r}'\right)$. From equation (3.46), the anomalous electric field is given by

$$\Delta\mathbf{E}_i\left(\boldsymbol{r}\right) = \int_V \mathbf{G}_{ij}^b\left(\mathbf{r},\mathbf{r}'\right)\Delta\boldsymbol{\sigma}_{jk}\left(\mathbf{r}'\right)\boldsymbol{\Gamma}_{ki}\left(\mathbf{r}'\right)\mathbf{E}_i^b\left(\boldsymbol{r}'\right)d\boldsymbol{r}' \tag{3.47}$$

From the discretization of equation (3.42) with dV as the anomalous volume, it follows that

$$\lambda_{ik}^p = \mathrm{G}_{ij}^{pq} dV \Delta\boldsymbol{\sigma}_{jk}^q \tag{3.48}$$

where $i,j = x,y,z = 1,2,3$ are tensors. The indices $p = 1,\ldots,\mathrm{M},$ and $q,r = 1,\ldots,\mathrm{N}$, are vectors; where, M is the number of receivers and N the number of model parameters or grid cells. The electric field for the scatterer in the right hand side of equation (3.47) can be expressed as

$$\mathrm{E}_k^p = \Gamma_{ki}^p \mathrm{E}_i^0 \tag{3.49}$$

where

$$\Gamma_{ki}^p = \left[\mathbf{I} - \lambda_{ik}^p\right]^{-1} \tag{3.50}$$

And **I** is the diagonal matrix. Two indices i and p are reduced to one, that is; $i, p \to J$ as

$$J = (i-1)\mathrm{M} + p \qquad (3.51)$$

Then in this notation, the discretized background electric field for the integral equation can be written as,

$$\mathrm{E}_K = \Gamma_{Ki}\mathrm{E}_i^0 \qquad (3.52)$$

The electric field between the background and the scattering domain for the Integral Equation in (3.47) where $\Delta\sigma_{JK}$ is the anomalous conductivity contrast for an anisotropic media can then be given as,

$$\Delta E_I = \mathrm{G}_{IJ}\Delta\sigma_{JK}E_K \qquad (3.53)$$

3.5 T-matrix Approximation

The integral equation can be approximated by using the T-matrix approach. The computation of the T-matrix is completely independent of the source-receiver configuration, but only requires the knowledge about the scattering potential (or perturbations) and the Green's function for the reference medium (Jakobsen 2012). The Green's function for any reference medium can be computed numerically once (Jakobsen 2012). According to Jakobsen (2012), the T-matrix approach as a method for the volume integral approximation is more useful for 4D than 3D seismic surveys, and can be useful for special 3D seismic forward modeling of fluid saturated cavities and related heterogeneities characterized by large or huge contrasts.

3.5.1 Derivation of T-matrix

The derivation of T-matrix is fully anisotropic in nature. Consider multiple receivers located at positions x_r where $r = 1,\ldots,R$. The domain V with the scattering potential $\Delta\sigma$ being non-zero is divided into a set of N grid blocks with centroids x_i and volume δv_i with $i = 1,\ldots,N$. The size of an individual grid block is chosen small enough compared to the dominant wavelength given by, $\lambda = 503(f\sigma)^{-1/2}$, where f is the dominant frequency and σ is the electrical conductivity. The symmetrized Lippmann-Schwinger equation after discretization can be written as (Jakobsen 2012),

$$\mathrm{E}_m = \mathrm{E}_m^b + \sum_{i=1}^{N}\sum_{j=1}^{N}\delta r_j \mathrm{G}_{mi}^b \Delta\sigma_{ij}\mathrm{E}_j \qquad (3.54)$$

where

$$\Delta\sigma_{ij}^{pq} = \Delta\sigma_i\delta_{ij}\delta_{pq} \qquad (3.55)$$

with
$$\delta_{ij},\delta_{pq}=\begin{cases}1:\ for\, i=j\\ 0:elsewhere\end{cases} \qquad (3.56)$$

And index m may refer to a receiver position as well as the position of a particular scattering object. For the discretization of Green's function, we use

$$\mathrm{G}_{ij}^{b}=\mathrm{G}^{b}\left(\boldsymbol{r}_i,\boldsymbol{r}_j\right),\quad i\neq j \qquad (3.57)$$

And

$$\delta v_i \mathrm{G}_{ii}^{b}=\int_{Vs} d\mathbf{r}\mathrm{G}^{b}\left(\boldsymbol{r}_i,\boldsymbol{r}_j\right) \qquad (3.58)$$

To calculate the Green's function values G_{ij}^{b} in equation (3.57), one can either use an analytical formula for homogeneous media, ray theory in the case of heterogeneous media (Jakobsen 2012), or purely numerical method. It now follows from Equation (3.46) that

$$\mathbf{E}_R=\mathbf{E}_{RV}^{b}+\mathbf{G}_{RV}^{b}\Delta\boldsymbol{\sigma}\mathbf{E} \qquad (3.59)$$

And

$$\mathbf{E}=\mathbf{E}^{b}+\mathbf{G}^{b}\Delta\boldsymbol{\sigma}\mathbf{E} \qquad (3.60)$$

where the components of the $R\times N$ - dimensional matrix $\mathbf{G}_{RV}^{b}$ is always given by Equation (3.56) since this matrix of Green's function values is associated with a single receiver position x_r and one scattering grid block position. In the calculation of the components of the $N\times N$ - dimensional matrix $\mathbf{G}^{b}$, both the Equations (3.59) and (3.60) are needed (Jakobsen 2012), since the matrix of Green's function values is associated with the positions x_p and x_q ($p,q=1,\ldots,N$) of similar or different grid blocks within the discretized scattering domain only. From the quantum mechanical potential scattering approach (Jakobsen 2012) the T-matrix is defined by

$$\Delta\boldsymbol{\sigma}\mathbf{E}=\mathbf{T}\mathbf{E}^{b} \qquad (3.61)$$

Using this definition in the Lippmann Schwinger Equation (3.59),

$$\mathbf{E}=\mathbf{E}^{b}+\mathbf{G}^{b}\mathbf{T}\mathbf{E}^{b} \qquad (3.62)$$

Multiplying Equation (3.62) with $\Delta\boldsymbol{\sigma}$ from the left,

$$\Delta\boldsymbol{\sigma}\mathbf{E}=\Delta\boldsymbol{\sigma}\mathbf{E}^{\boldsymbol{b}}+\Delta\boldsymbol{\sigma}\mathbf{G}^{b}\mathbf{T}\mathbf{E}^{\boldsymbol{b}} \qquad (3.63)$$

Using the definition (in equation 3.61) of the T-matrix in conjunction with the above Equation (3.63),

$$\mathbf{T}\mathrm{E}^{b} = \Delta\boldsymbol{\sigma}\mathbf{E}^{\boldsymbol{b}} + \Delta\boldsymbol{\sigma}\mathbf{G}^{b}\mathbf{T}\mathbf{E}^{\boldsymbol{b}} \tag{3.64}$$

Since $\mathbf{E}^{\boldsymbol{b}}$ is arbitrary, it follows that

$$\mathbf{T} = \Delta\boldsymbol{\sigma} + \Delta\boldsymbol{\sigma}\mathbf{G}^{b}\mathbf{T} \tag{3.65}$$

Thus from Equation (3.65), which is the Lippmann-Schwinger equation for the T-matrix, it follows that

$$\mathbf{T} = \left(\mathbf{I} - \Delta\boldsymbol{\sigma}\mathbf{G}^{b}\right)^{-1}\Delta\boldsymbol{\sigma}\,, \tag{3.66}$$

which represents a full numerical solution of the LS- equation including all the effects of multiple scattering. The full numerical solution may be convenient for forward modeling, at least if the models are not too large, like in many cases of 4D seismic. However, for inverse modeling, it is imperative to use an approximation; which can be the Born (Neumann) series for the T-matrix (Sheng 1995). This approximation can be written as

$$\mathbf{T} = \Delta\boldsymbol{\sigma} + \Delta\boldsymbol{\sigma}\mathbf{G}^{b}\Delta\boldsymbol{\sigma} + \Delta\boldsymbol{\sigma}\mathbf{G}^{b}\Delta\boldsymbol{\sigma}\mathbf{G}^{b}\Delta\boldsymbol{\sigma} + \ldots = \left[\sum_{k=0}^{\infty}\left(\Delta\boldsymbol{\sigma}\mathbf{G}^{b}\right)^{k}\right]\Delta\boldsymbol{\sigma} \tag{3.67}$$

which is obtained from equation (3.66), for $\left\|\mathbf{I} - \Delta\boldsymbol{\sigma}\mathbf{G}^{b} \gg 0\right\|$; that is, the contrast volume is sufficiently small, and **I** is an identity matrix (Jakobsen 2012).

3.5.2 Implementation of T-matrix

For a domain **V** discretized into grid cells each of volume $\Delta\mathrm{V}$ with constant conductivity contrast with in each cell, the integral equation for the anomalous field in discretized form can be written as,

$$\Delta E_{i}^{p} = G_{ij}^{pq}T_{jk}^{qr}\mathrm{E}_{k}^{r}\Delta V \tag{3.68}$$

For T-matrix approach,

$$\mathbf{T}_{jk}^{qr} = \left(\mathbf{I} - \Delta\boldsymbol{\sigma}_{ml}^{st}\mathbf{G}_{lj}^{tq}\right)^{-1}\Delta\boldsymbol{\sigma}_{mk}^{sr} \tag{3.69}$$

The indices in equation (3.68) to be valid for implementation in MATLAB, it should be that the indices $m = l$ and $s = t$. The indices $p = 1,\ldots,\mathrm{M}$ and $q,r,s,t = 1,\ldots,\mathrm{N}$, where M and N are the number of receivers in the survey and the number of grid cells respectively. By reducing the indices from 2 to 1, that is; $i,p \to \alpha$ and $j,q \to \beta$

$$\alpha = (i-1)\mathrm{M} + p \text{ and } \beta = (j-1)\mathrm{N} + q \tag{3.70}$$

Letting indices, $c, \mathrm{s} \to \chi$; $\mathrm{l}, t \to \zeta$, and $k, r \to \gamma$ that is

$$\chi = (c-1)\mathrm{N} + \mathrm{s}$$

$$\zeta = (l-1)\mathrm{N} + t \tag{3.71}$$

$$\gamma = (k-1)\mathrm{N} + r$$

Thus equation (3.69) in reduced indices is written as

$$\mathbf{T}_{\beta\gamma} = \left(\mathbf{I} - \Delta\boldsymbol{\sigma}_{\chi\zeta}\mathbf{G}_{\zeta J}\right)^{-1} \Delta\boldsymbol{\sigma}_{\chi\gamma} \tag{3.72}$$

Thus using equations (3.70 – 3.72), equation (3.68) with $\mathbf{G}_{\alpha\beta} = \mathbf{G}_{ij}^{pq}\Delta V$ in discretized form can be written as,

$$\Delta\mathbf{E}_{\alpha} = \mathbf{G}_{\alpha\beta}\mathbf{T}_{\beta\gamma}\mathbf{E}_{\gamma} \tag{3.73}$$

In the MATLAB code for T-matrix, $\mathbf{G}_{\alpha\beta}$ was computed as $\mathbf{G}_{vv}$ and $\mathbf{G}_{rv}$ the Green's tensor in the background and in the scattering domain, respectively. The new coupling $\mathbf{T}_{\beta\gamma}$ for the diagonal anomalous conductivity and the background Green's tensor can be modified to cater for both homogeneous and heterogeneous models obtained by reducing 4 indices to 2; and $\mathbf{E}_{\gamma}$ is the electric field obtained with no hydrocarbon present. For the T-matrix and the Extended Born approximations, the singularity of the Green's function is considered by using equation (3.19).

4 Modeling 3D and 4D CSEM Data

4.1 Outline

Numerical modeling has today been applied as an engine for EM inversion, verification of hypothetical conductivity models constructed, and as a tool for various feasibility studies (Avdeev 2005). Forward modeling involves the use of known geological structures to produce geophysical field data. This technique determines what a given sensor would measure in a given formation and environment by applying a set of theoretical equations for the sensor response. This begins with a numerical solution to the equation of motion. Therefore, numerical modeling represents an approach in which a true earth structure is replaced by one for which a numerical approximation to Maxwell's equations can be made and evaluated. There are several techniques for electromagnetic forward modeling and in this chapter a 3D CSEM model is considered in relation to the integral equation approximations of the Born, Extended Born and the T-matrix approaches. The dependence of these approximations on the reservoir model and their effects on changing the reservoir parameters such as contrast volumes, conductivity contrasts, number and size of grid cells will be discussed. Depending on the simplifying assumptions made for the Born, Extended-Born, and the T-matrix, it is expected that the reservoir parameters will affect these approximations differently.

Since the frequency of the fields emitted by the source strongly affects the signals (Lien and Mannseth 2008), very low source frequencies of 0.25 Hz in particular will be used. The MATLAB code (*EMforward.m*) based on the Born, T-matrix and the Extended Born approximations to integral equation for the 3D electromagnetic field case has been developed. The code was tested on the 3D geo-electrical models in the next sections.

4.1.1 Effect of Grid Size

In modeling, while using the approximations to the integral equation, the scatterer needs to be discretized into a large number of grid cells depending on the reservoir dimensions, frequency and the depth of the scatterer from the seabed (Gao, Fang et al. 2003). Therefore, increasing the number of grid cells in the discretization scheme will significantly increase the computation time and memory required to store the larger matrices.

To determine the optimal grid size, a simple model consisting of a cube of dimensions 150 m was considered. The total number of grid cells depends on the grid size for a reservoir with fixed dimensions. Here, modeling was done fast with the grid blocks assumed to be cubes of varying sizes of 150 m, 75 m, 50 m, and 25 m. The T-matrix approach was used since it is able to approximate roughly the solution of the full integral equation. The scatterer as a

control was also considered as a big grid block for comparing the effects of the grid size since it gave the maximum amplitude (figure 4.1). The computation time was seen to depend on the size of the grid block. Finer grid blocks imply a larger number of grid cells and hence more computation time. Decreasing the size of grid blocks increases the number of the grid cells (Table 1) which in turn decreases the magnitude of the anomalous electric field recorded by the receivers (figure 4.1 and 4.2).

Size of the grid cell (m^3)	**Time taken (s) to compute**		**Relative errors (%)**	
	Green's	T-matrix	Magnitude	Phase
150×150×150	0.004	0.228	35.53	6.52
75×75×75	0.011	0.122	11.92	2.88
50×50×50	0.049	0.186	5.88	1.47
25×25×25	1.777	3.847	-	-

Table 1*: The table showing the effect of grid size on computation time and errors for the different sizes relative to the 25 m cube for a cubic scatterer of 150 m using the T-matrix approximation.*

The course grid model records a higher value in magnitude as compared to the finer and a relatively larger model gives large amplitude compared to the smaller one. This effect can be illustrated from table 1 alongside the errors computed for the different grid sizes relative to the T-matrix solution for a 25 m cubic grid block. In figure 4.1, the relative errors in magnitude and phase for a 150 m cubic scatterer were plotted. It is clearly shown that there is convergence for the T-matrix approximation as the grid size decreases. The relative error in phase calculated by the T-matrix method had a change of 6.5% from the finest to the coarsest grid cells. The error between the two successive amplitudes decreases as the grid size decrease. This laterally means that the magnitude tends to be the same as the grid size decreases.

To confirm the optimal size of the grid block to be considered in modeling, a separate test was conducted on a 100 m cubic scatterer to obtain different grid sizes. It can be shown from figure 4.2 that for a 25 m grid block there was convergence in amplitude and phase. The relative errors were analyzed for the magnitude and phase using the T-matrix approximations to the integral equation. The relative errors however, decrease with the decrease in the size of the grid cells.

Therefore, with the 25 m grid cell giving small errors compared to the neighboring grid sizes will be considered in the next sections to discuss the different approximations to the integral equation and how they are affected by the different reservoir parameters. However, the 25 m grid has some drawbacks like requiring much more computation time if bigger scattering volumes were to be considered.

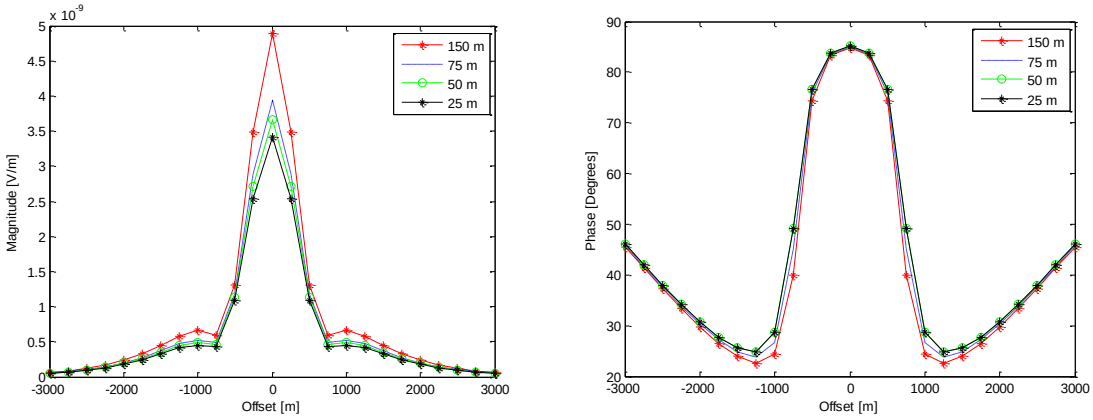

(a) $\Delta\mathbf{E}_x$ for 150 m cube (b) θ_x for 150 m cube

Figure 4.1: *Effects of grid size on convergence when* $\Delta\mathbf{E}_x$ *(a) and* θ_x *(b) for a cubic scatterer of size 150 m and contrast -0.25 S/m were considered. The scatterer was discretized into cubic grids of size 150 m (red), 75 m (blue), 50 m (green) and 25 m (black).*

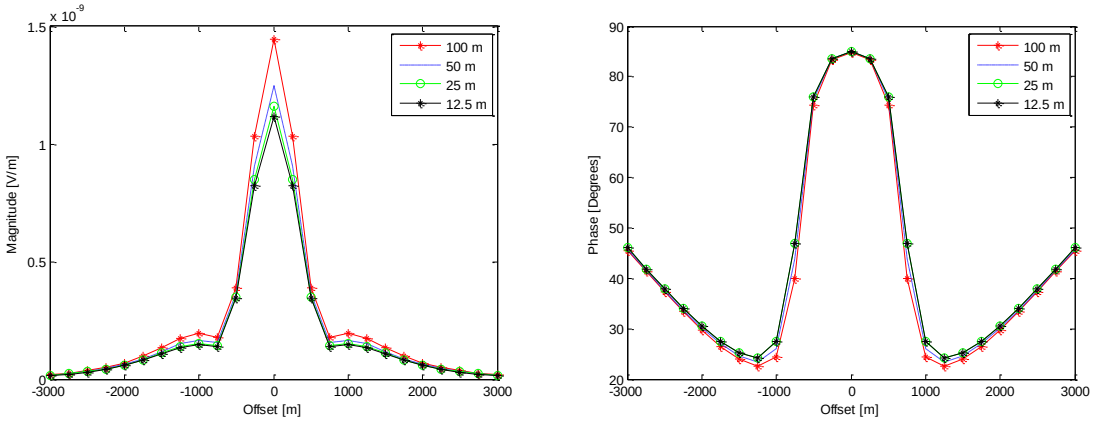

(a) $\Delta\mathbf{E}_x$ for 100 m cube (b) θ_x for 100 m cube

Figure 4.2: *Effects of grid size on convergence when* $\Delta\mathbf{E}_x$ *(a) and* θ_x *(b) for a cubic scatterer of size 100 m and contrast -0.25 S/m were considered. The scatterer was discretized into cubic grids of size 100 m (red), 50 m (blue), 25m (green) and 12.5 m (black).*

4.2 Homogeneous Model

In this section, a detailed comparison of the different approximations was considered for a homogeneous conductivity model. As already discussed, the number of grid cells heavily affects the amplitude and phase of the anomalous electric field. Here, a cube of grid size of 25 m was used to investigate the limit of accuracy of the different approximations for high and low contrasts. The conductivity of the reservoir was varied as discussed by Gelius and Tygel (2013) to have values of $0.001 \le \sigma \le 0.499$ [S/m].

4.2.1 Geometry of the Model

The geo-electric model discussed here was obtained (and modified) from Gelius and Tygel (2013) to consist of a line of 25 receivers that were arranged along the middle row (y = 0) of the reservoir. It stretched from -3000m to 3000m along the x- direction with in a homogeneous background with no sea layer and the source placed at (0, 0, 0). An electric dipole transmitter was considered towed along the in-line (x-direction) with an interval of 250 m between the receivers. As noted in Zhdanov (2009) for simulation, the broadcasting frequency was considered as 0.25 Hz and the current at the transmitter end to be 1000 A. The input and reservoir parameters were summarized the table 2.

Source and receiver		**Reservoir model**	
Receivers (number)	25	Thickness (m)	50
Receiver separation (m)	250	Depth (m)	850
Dipole length (m)	100	Conductivity, σ^b (S/m)	0.5
Source strength (A)	100000	Conductivity, σ (S/m)	$0.001 \le \sigma \le 0.499$
Frequency (Hz)	0.25	Grid cells (number)	$30 \times 10 \times 2$
Depth (m)	0	Grid volume (m^3)	$25 \times 25 \times 25$

Table 2: *Source, receiver and reservoir model parameters used in forward CSEM modelling. The symbols used; m-meter, A-ampere, Hz-hertz, S/m- Siemens per meter.*

The receivers record signals from the transmitting horizontal electric dipole of 100 m in length with a source strength of 100×1000 A, and from the electromagnetic response of the geo-electric structures (Zhdanov 2009). Figure 4.3 shows the location of the reservoir model in the vertical plan. A resistive hydrocarbon reservoir with half dimensions as that in Gelius and Tygel (2013), that is; $750 \times 250 \times 50 m^3$ was embedded in a conductive layer placed to have its center at (0, 0, 850 m) below the receivers as shown in figure 4.4.

The resistivity of the conductive layer will however vary as saline water is injected during hydrocarbon production. In figure 4.4, illustrates the scatterer and acquisition geometry. The domain was chosen as $-375m \le x \le 375m$, $-125m \le x \le 125m$ in the x- and y- directions and $0m \le z \le 850m$ in the z direction with uniform grid size as $\Delta x = \Delta y = \Delta z = 25m$.

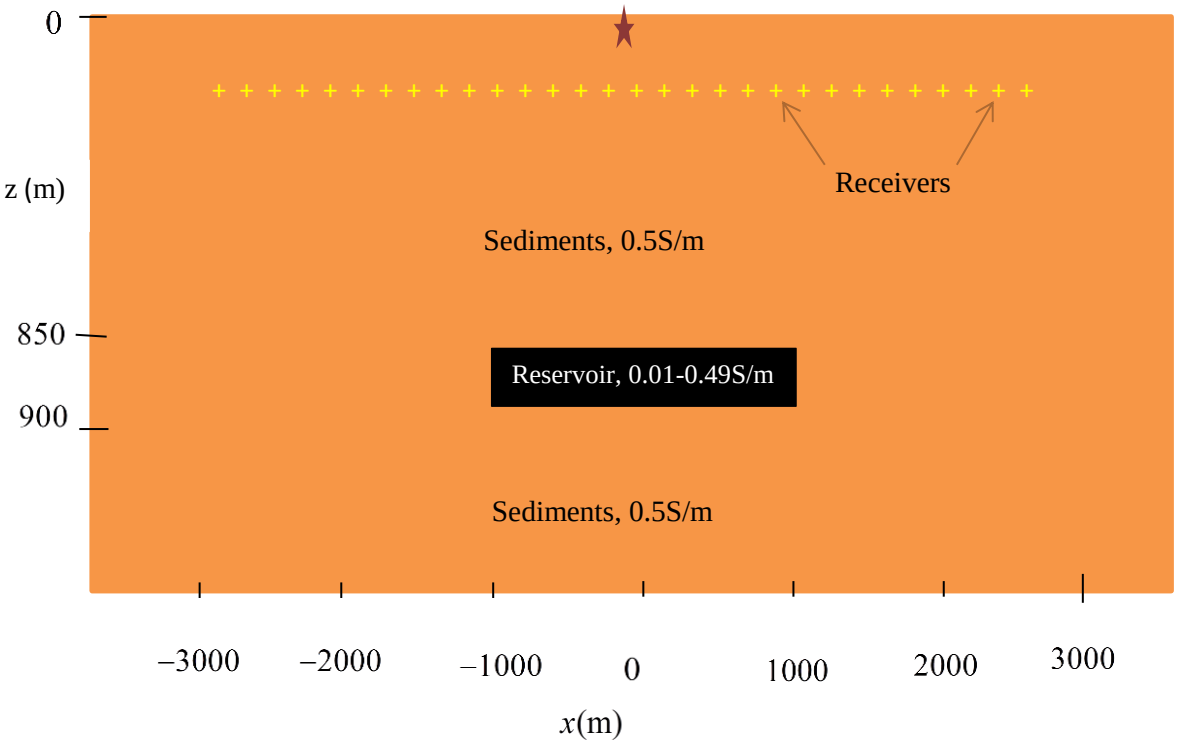

Figure 4.3: *Vertical section through a 2D homogeneous geo-electrical model for the CSEM showing the location of the source (red), receivers (+) and reservoir (black) with conductivity 0.5 S/m located at a depth of 850m below seafloor with conductivity of range 0.01-0.49 S/m.*

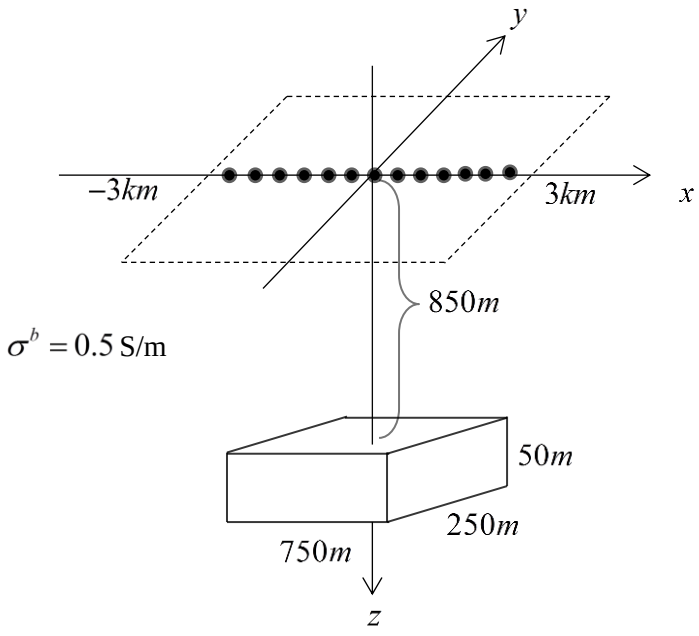

Figure 4.4: *3-D Schematic view of scatterer and acquisition geometry. The receivers (black circles) are placed along the x-direction with the reservoir located at a depth of 850 m below the seabed.*

The electric fields from the scatterer were computed based on equation (3.37), equation (3.53) and equation (3.73) for the Born, Extended Born and the T-matrix approximations, respectively. The results obtained from the Born and EBA were compared to those from the T-matrix approach which roughly approximate the solution of the full integral equation.

The horizontal E-field measured along the survey line is usually dominated by the radial field component which is responsible for increase in the amplitudes and phases of the E-fields as the lateral extent of resistor increases (Bhuyian, Landrø et al. 2012). For data display, only the amplitude and phase of the inline anomalous electric field ($\mathbf{E}_x$) will plotted and compared for the different approximations when contrast was varied.

The effect of the conductivity contrast on the accuracy of different approximations was also analysed. The conductivity of the scatterer was chosen as 0.499 S/m which is so close to that of the background medium. This from equation (3.25) implies that the contrast will be small ($\Delta\sigma = -0.001\,\text{S/m}$). Figure 4.5 (a) and (b) shows the magnitude and phase for the Born, Extended Born and T-matrix converge which is consistent from the theory. As the conductivity in the scatterer increases ($\sigma = 0.25$ S/m), the contrast also increases ($\Delta\sigma = -0.25$) which makes the magnitude and phase for Born to deviate much from that of extended Born and the T-matrix. Figure 4.5 (c) and (d) shows that for near offsets, the magnitude for Born is less than that corresponding to Extended Born and T-matrix. However, for larger offsets, the three approximations tend to agree in magnitude though with different phases.

Figure 4.5 (e) and (f) were obtained when magnitude and phase, respectively were plotted for the conductivity of 0.001 S/m in the scatterer to give to a high contrast $\Delta\sigma = -0.499\,\text{S/m}$. The Extended Born is a better estimate with the T-matrix slightly below the EBA while the magnitude for Born decreased sharply as compared to that of EBA and TMA. The figure also indicates that the Extended Born and T-matrix approximation gave same values in the phase and with a phase shift from +80 to -80 degrees in the region where the reservoir is situated. The Born still has a higher positive phase and largest in the vicinity of the reservoir.

4.2.2 Relative Errors

Errors in CSEM data are majorly of two forms; (1) measurement errors which are random instrumental noise; and (2) modeling errors due to the misrepresentation of the correct physical problem (Bhuyian, Landrø et al. 2012). The errors in magnitude and phase for both the Born and Extended Born were computed relative to the T-matrix from

$$\varepsilon_{app} = \frac{\left|E_{TMA} - E_{app}\right|}{\left|E_{TMA}\right|} \times 100\% \qquad (4.1)$$

And

$$\varphi_{app} = \frac{\left|\theta_{TMA} - \theta_{app}\right|}{\left|\theta_{TMA}\right|} \times 100\% \qquad (4.2)$$

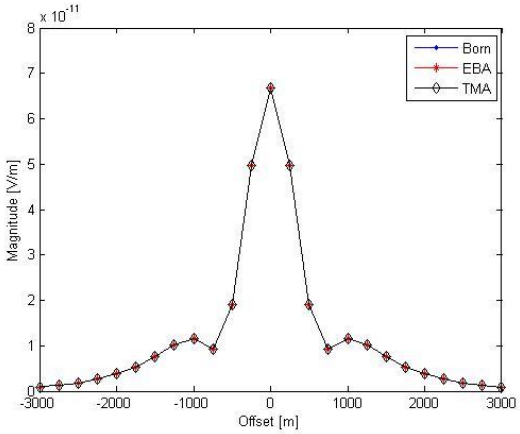

(a) $\Delta \mathbf{E}_x$ with $\Delta\sigma$ = -0.001

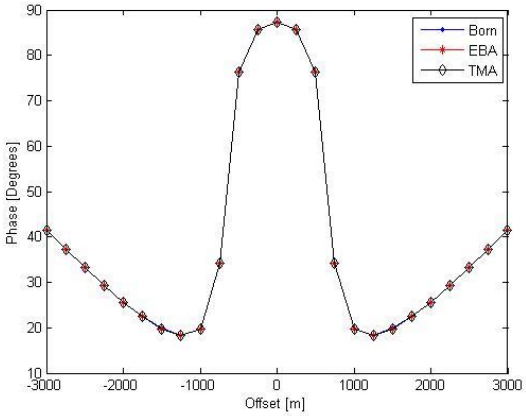

(b) θ_x with $\Delta\sigma$ = -0.001

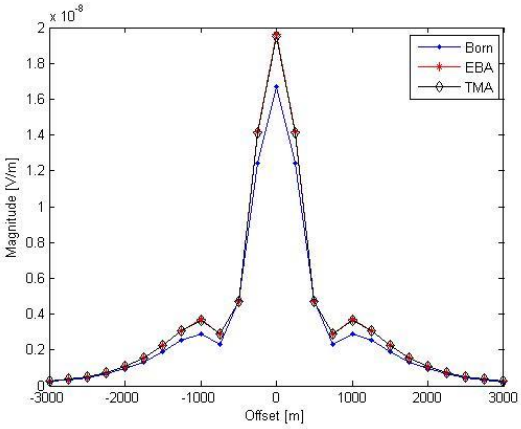

(c) $\Delta \mathbf{E}_x$ with $\Delta\sigma$ = -0.25

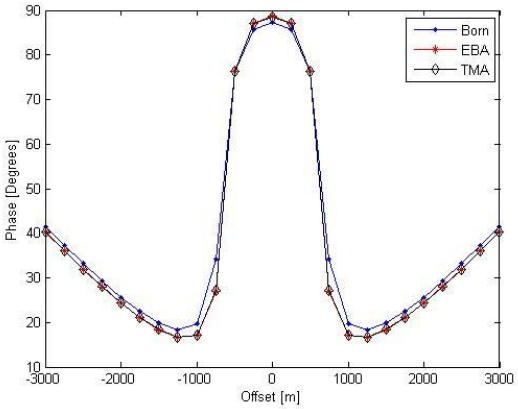

(d) θ_x with $\Delta\sigma$ = -0.25

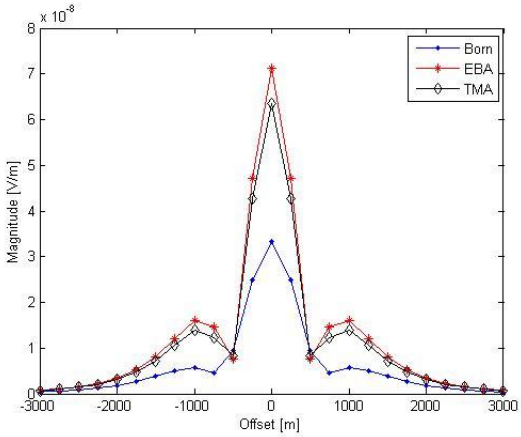

(e) $\Delta \mathbf{E}_x$ with $\Delta\sigma$ = -0.499

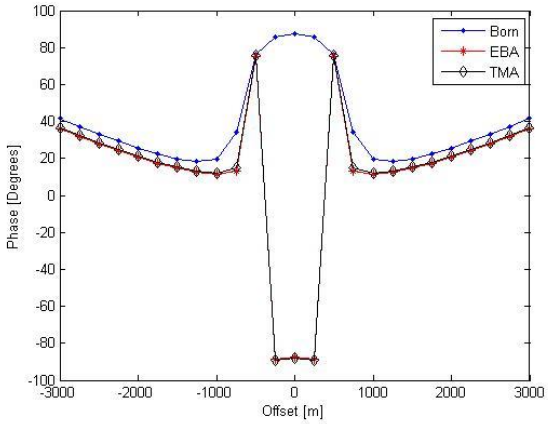

(f) θ_x with $\Delta\sigma$ = -0.499

Figure 4.5: *Magnitude (left) and phase (right) of the anomalous electric field for a homogeneous reservoir model with varying contrasts; (a) - (b), low; (c) - (d), moderate and; (e) - (f), high. The background conductivity is 0.5 S/m and the frequency of 0.25 Hz is used.*

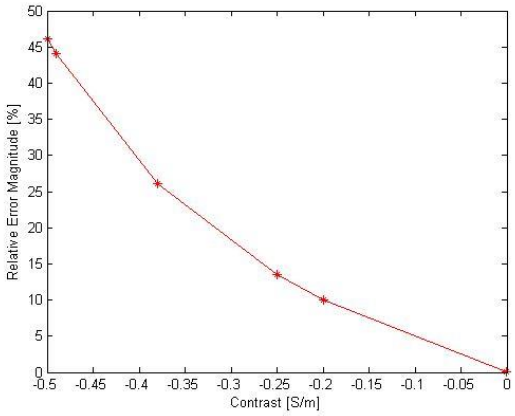

(a) Magnitude for ε_{app} Born

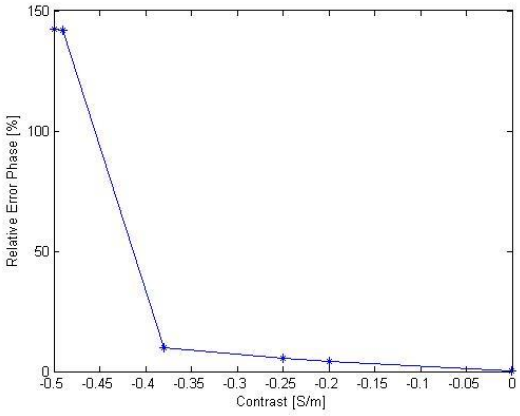

(b) Phase for φ_{app} Born

Figure 4.6**:** *Errors in (a) magnitude and (b) phase for Born approximation relative to T-matrix approach when different contrasts were considered for a homogeneous model.*

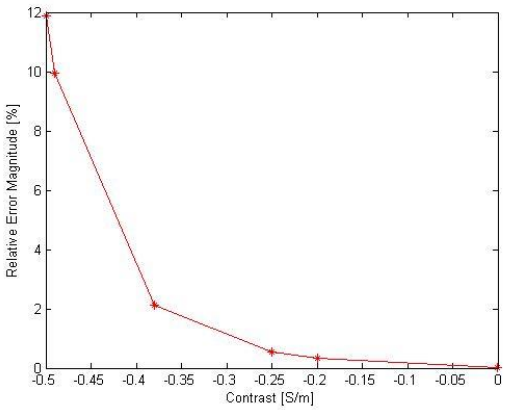

(a) Magnitude for ε_{app} EBA

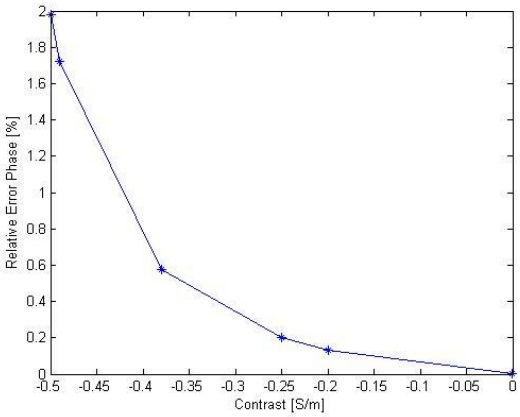

(b) Phase for φ_{app} EBA

Figure 4.7***:*** *Errors in (a) magnitude and (b) phase for Extended Born approximation relative to the T-matrix approach for the different contrasts for a homogeneous model.*

where ε_{app} and φ_{app} are the relative errors in magnitude and phase for the approximation considered; E_{TMA} and θ_{TMA} are the magnitude and phase for the T-matrix ; while E_{app} and θ_{app} the magnitude and phase in the approximation considered. Here, only the anomalous filed was considered for the computation of these relative errors. As shown in figure 4.6 and 4.7, the relative errors in magnitude are higher for Born, which is between 45- 25 % than for the Extended Born with 12- 2 % from higher to moderate contrasts. In figure 4.7 (a) and (b), there is a minimal error of 0.5- 0 % in the magnitude and phase when the Extended Born is used to approximate the integral equation relative to the T-matrix for moderate to low contrasts. The Born approximation has higher errors in phase for large contrast (150 %) but decreases rapidly for moderate to small contrasts (from 10- 0 %). The error in phase between the Extended Born and Born is almost 75 times larger for higher contrasts.

5 Inversion of 3D and 4D CSEM Data

In this chapter, time-lapse monitoring and Born inversion on the 3D forward data generated by the approximations of the Born, T-matrix and Extended Born have been performed. The results for these approximations will greatly depend on the approach used and the noise level in the data parameters. The major focus will be on the accuracy of the inverted data from the T-matrix and Extended Born relative to the Born approximation.

5.1 Monitoring of 3D CSEM Data

Time-lapse water flood monitoring in hydrocarbon reservoirs is normally used to distinguish different shapes of the advancing waterfront (Zach, Frenkel et al. 2009). To apply 4D CSEM monitoring, there is a need for permanently installed system to reduce the errors incurred in repeating the experiment. During monitoring, measurements of in-line electric field, E_x at a single frequency are conducted at different times with the source and the receiver locations being fixed. Repeating the experiment is not only done for monitoring purposes but also greatly reduces the measurement and modeling errors incurred during forward modeling. This enhances the signal-to-noise ratio after the spatial derivatives of the signal are accurately calculated (Andréis and MacGregor 2011). Initially before injection, the total electric field is given from equation (3.26) as

$$E_x^i(r) = E_x^{ib}(r) + \partial E_x^i(r) \qquad (5.1)$$

After injection and the measurements repeated, the electric field becomes

$$E_x^r(r) = E_x^{ir}(r) + \partial E_x^r(r) \qquad (5.2)$$

Since the background field is independent of time, this means that,

$$E_x^{ib}(r) = E_x^{ir}(r) \qquad (5.3)$$

where $E_x^{ib}(r)$ and $E_x^{ir}(r)$ are the initial and repeated background fields respectively. Due to changing conductivity distribution within the reservoir, the anomalous electric field will change with time (Lien and Mannseth 2008). Then, the magnitude of time-lapse anomalous in-line electric field difference is given by subtracting equation (5.1) from equation (5.2) as

$$\delta E_x^{r-i}(r) = E_x^r(r) - E_x^i(r)$$

$$\delta E_x^{r-i}(r) = \left[E_x^{rb}(r) + \partial E_x^r(r)\right] - \left[E_x^{ib}(r) + \partial E_x^i(r)\right]$$

$$\delta E_x^{r-i}(r) = \partial E_x^r(r) - \partial E_x^i(r) \qquad (5.4)$$

where i and r, respectively represent the initial and repeat measurements. The $\partial E_x^i(r)$ and $\partial E_x^r(r)$ are the initial and repeat anomalous electric field measurements respectively, which satisfy the condition; $\left|\delta E_x^{r-i}\right| \ll \left|\partial E_x^r\right| or \left|\partial E_x^i\right|$. Similarly, $\delta\theta$ the associated time-lapse phase difference, is given by subtraction of the initial phase from the repeated as

$$\delta\theta = \theta^r - \theta^i \qquad (5.5)$$

5.1.1 Time-lapse CSEM

In this section, the lateral extent (saturation) of the injected fluid was modeled to increase whereas the conductivity of the injected fluid and hydrocarbon remained fixed. The section, a homogeneous model though not feasible for CSEM production and monitoring was previously used to develop the methodology, test the accuracy and limits of the MATLAB codes. The 4D CSEM forward modelling using MATLAB code (*EMforward.m*) for the Born, EBA and TMA to the integral equation will be discussed for two reservoir models.

Two models with different reservoir dimensions ("small" and "large") were considered. The number of grids, grid size and the reservoir size were increased. The model was assumed to have 403 receivers arranged in 13 rows each with 31 receivers, the grid size of $50\times50\times50m^3$ for a reservoir with $1500\times1500\times50m^3$ in order to increase the sensitivity of the monitoring as indicated in figure 5.1. Figure 5.2, illustrates the injection and production wells used in modelling; where a lateral flooding of water from the left to right was simulated.
Three sets of background conductivity for each grid cell related to one pre and two post injection surveys have been used to model the CSEM response as in figure 5.3. Using conductivities of the injected fluid as 0.38 S/m and that of hydrocarbon as 0.28 S/m, the data was acquired at each stage during production, to consist of amplitude and phase of the electric field. For more analysis, the amplitude ratios, 4D anomaly and the phase differences between pre and post injection will be calculated.

5.1.2 Model 1

For model 1, the reservoir dimensions in figure 5.1 were halved in x and y- directions $750\times750\times25m^3$. The optimal grid size of $25\times25\times25m^3$ maintained discretizing the reservoir into grids gave $30\times30\times1$ cells. The conductivities for the injected fluid and the hydrocarbon were 0.38 S/m and 0.28 S/m. Figure 5.3 illustrates the waterfront in the reservoir; (a) before injection, (b) after 5 years, and (c) after 10 years of production.

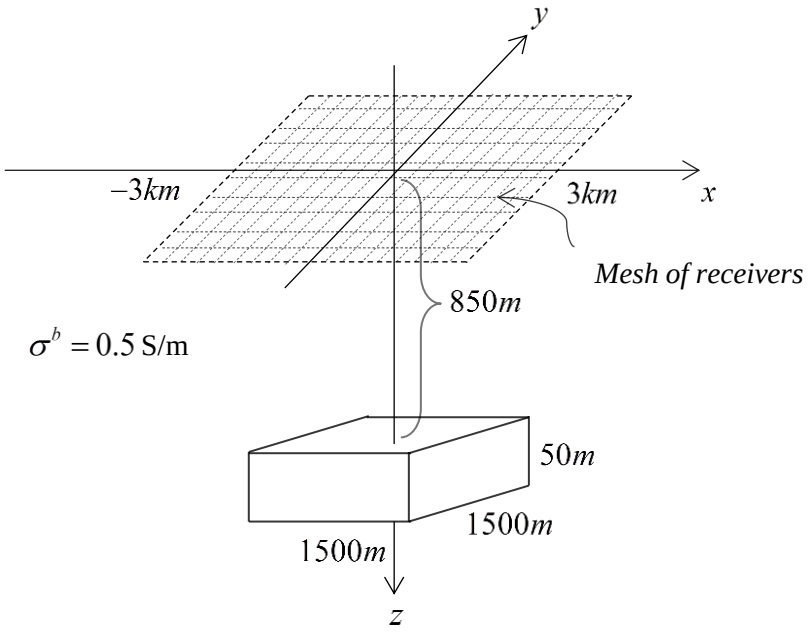

Figure 5.1*: The reservoir model with a 2D receiver grid as viewed from the side. The source is located in the middle of the mesh emitting a signal at a single frequency of 0.25Hz.*

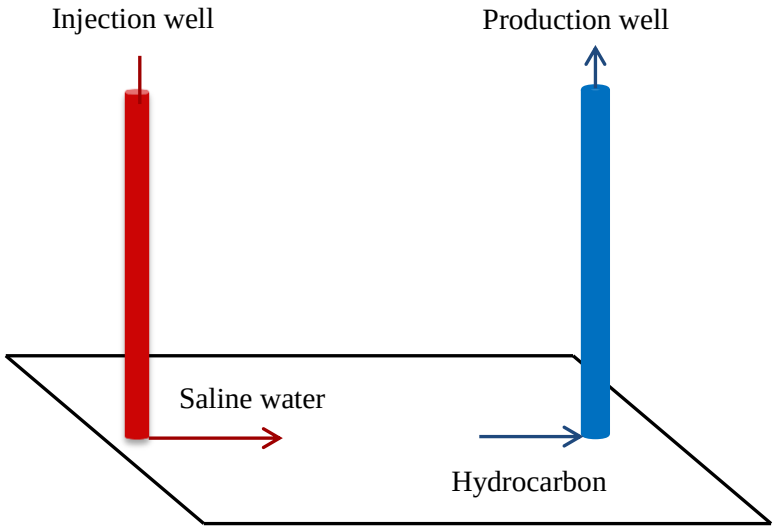

Figure 5.2: *A schematic illustration of the water flooding and position of the injection and production wells in the reservoir.*

The magnitude and phase for the middle receiver row were plotted in addition to the 4D anomaly, phase difference and amplitude ratio to be compared with the results from the larger model (model 2). The data set in magnitude and phase acquired before and during production were plotted in figure 5.4 to show the effects of water flooding on the reservoir. The magnitude of the electric field decreased as more saline water was injected. Born approximation is observed to be less accurate although the deviation decrease as the water front floods to the right of the reservoir.

Reservoir Model	**Error in Born** (%)				**Error in EBA** (%)			
	Model 1		*Model 2*		*Model 1*		*Model 2*	
	ε_B	φ_B	ε_B	φ_B	ε_{EBA}	φ_{EBA}	ε_{EBA}	φ_{EBA}
After 5 years	45.43	1142.85	17.36	99.86	2.57	0.49	0.20	0.06
After 10 years	47.89	132.06	12.57	70.69	1.26	1.69	0.11	0.08
Between 5 and 10 years	51.67	58.59	9.31	2.69	0.36	0.04	0.05	0.05

Table 3: *Errors in magnitude and phase for Born and Extended Born relative to the TMA solution for anomalous electric field in the reservoir while in production for models 1 and 2.*

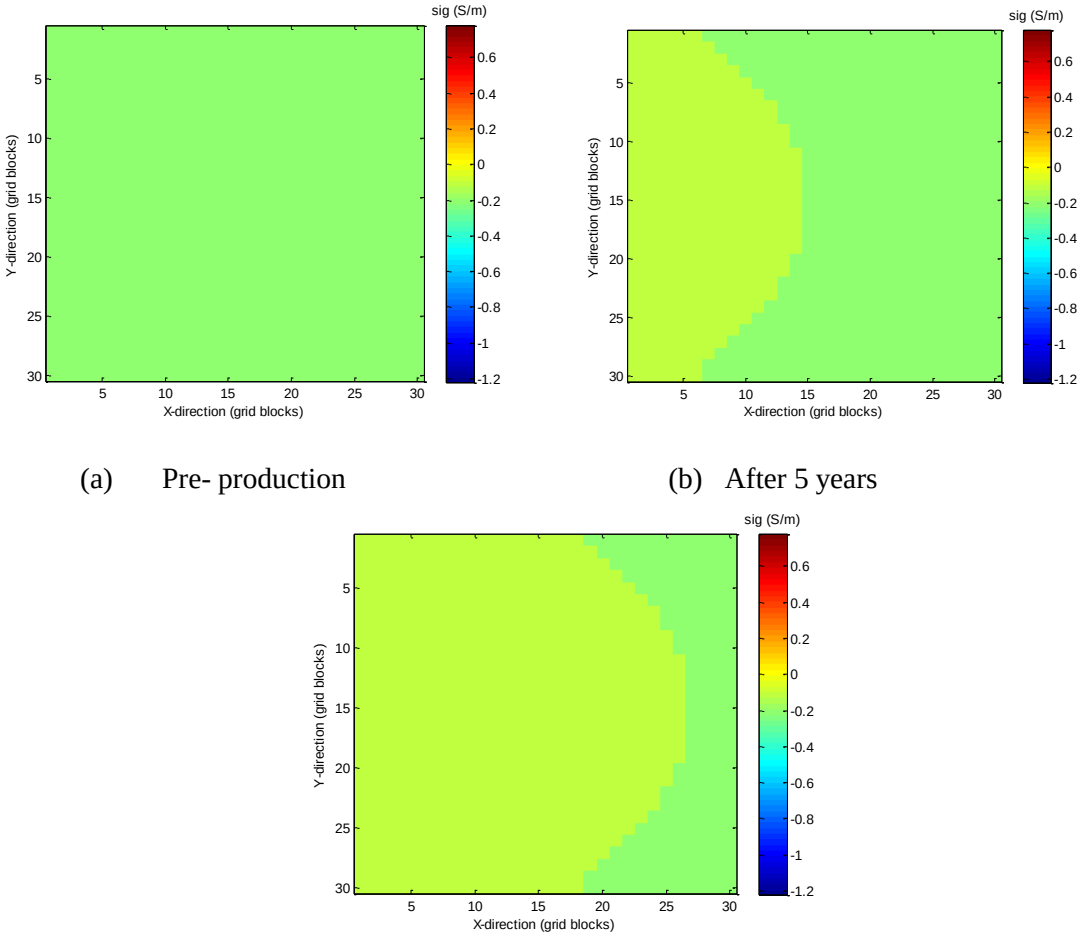

(a) Pre- production

(b) After 5 years

(c) After 10 years

Figure 5.3**:** *Visualization models for time-lapse CSEM (a) before and (b) after 5 years, and (c) after 10 years of production. The water floods laterally in the positive x-direction of the reservoir. Theconductivities of water (light green) and hydrocarbon (green) were 0.38 S/m and 0.28 S/m.*

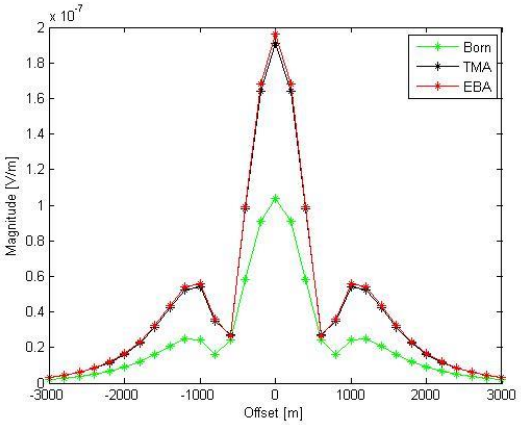

(a) ΔE_x at t_0 (Before)

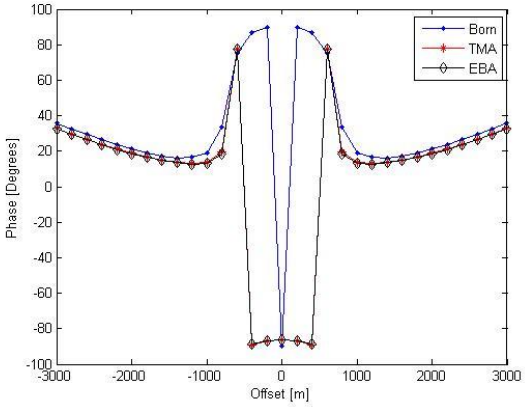

(b) θ_x at t_0 (Before)

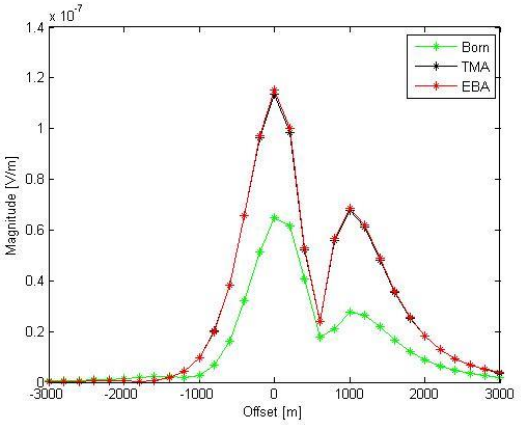

(c) ΔE_x at t_1 (After 5 years)

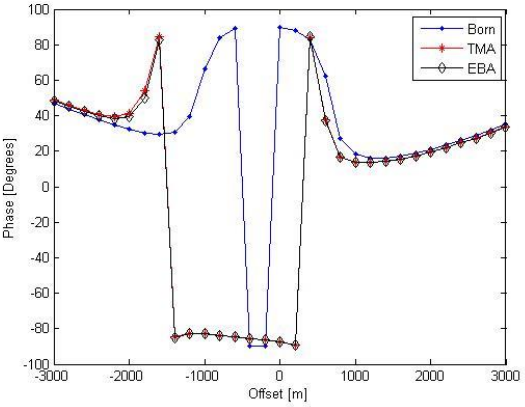

(d) θ_x at t_1 (After 5 years)

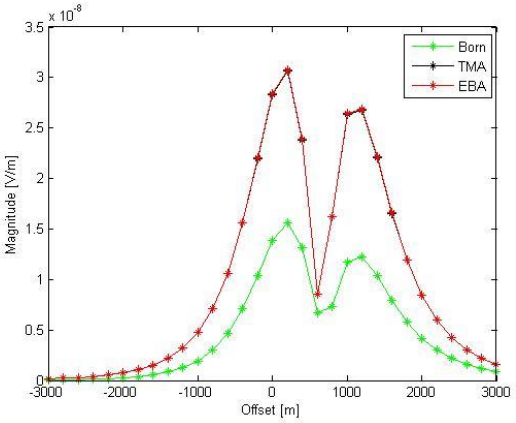

(e) ΔE_x at t_2 (After 10 years)

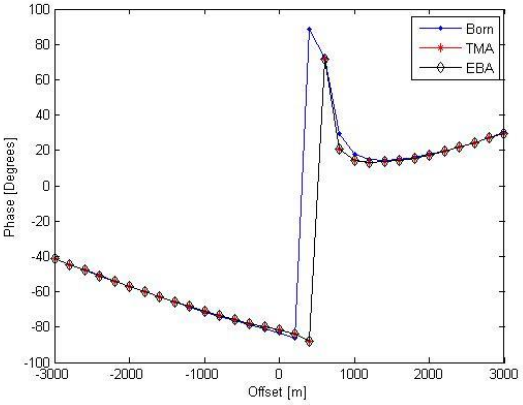

(f) θ_x at t_2 (After 10 years)

Figure 5.4: *Magnitude (left) and phase (right) for the anomalous electric field in reservoir model 1 before and during production; (a)-(b) before production, (c) - (d) after 5 years and (e) - (f) after 10 years of production when using the frequency of 0.25 Hz.*

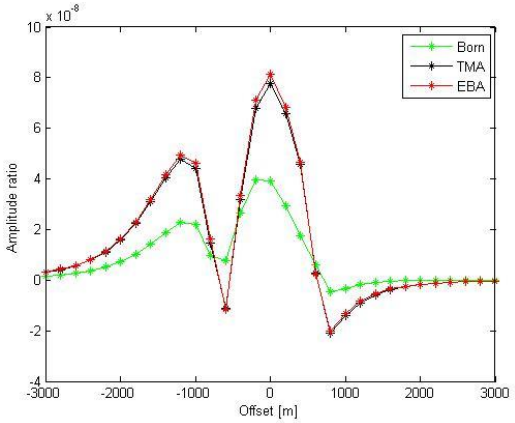

(a) ∂E_0 (between t_0 and t_1)

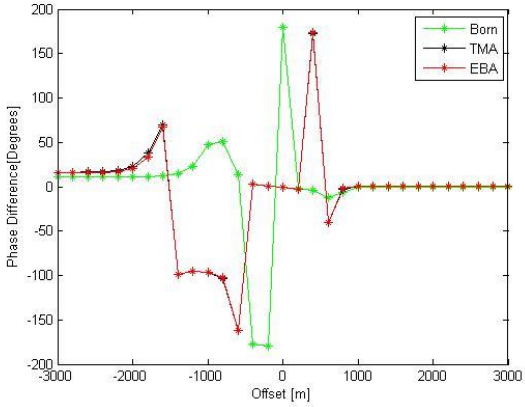

(b) $\delta\theta_0$ (between t_0 and t_1)

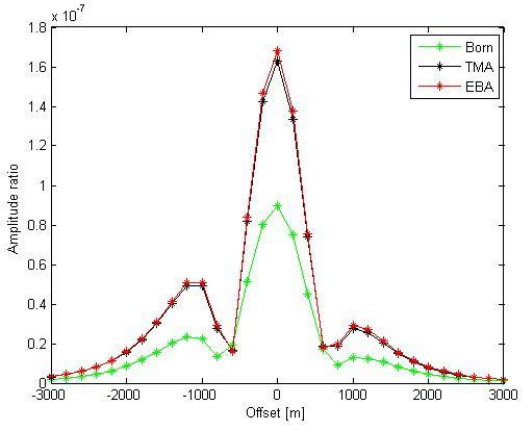

(c) ∂E_1 (between t_0 and t_2)

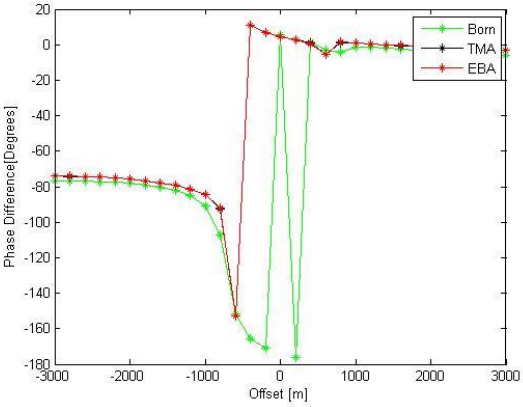

(d) $\delta\theta_1$ (between t_0 and t_2)

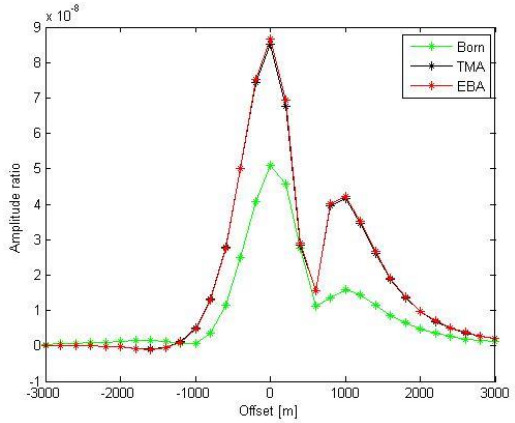

(e) ∂E_2 (between t_1 and t_2)

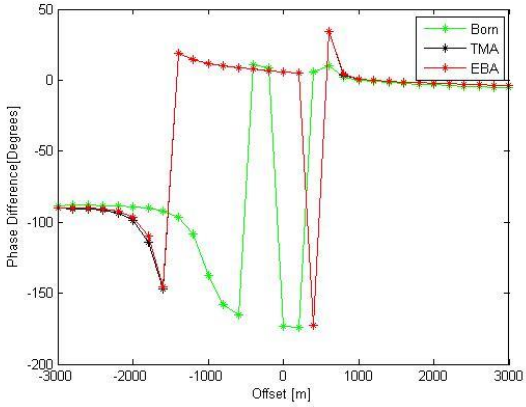

(f) $\delta\theta_2$ (between t_1 and t_2)

Figure 5.5: *Time- lapse Magnitude (left panel) and phase (right panel) for anomalous field; (a) - (b) before production; (c) - (d) after 5 years and; (e) - (f) after 10 years of production for model 1.*

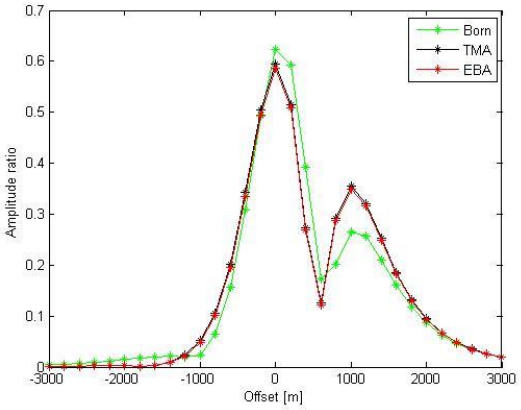

(a) A_R (between t_0 and t_1)

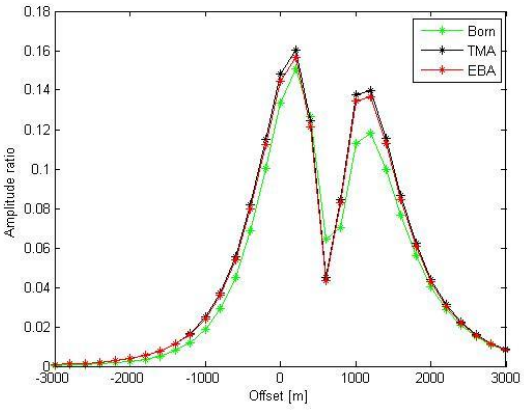

(b) A_R (between t_0 and t_2)

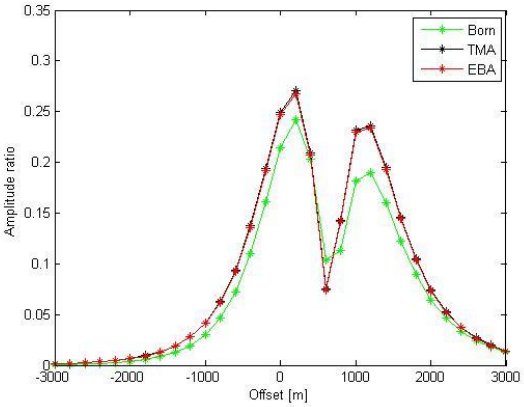

(c) A_R (between t_2 and t_1)

Figure 5.6: *Amplitude ratio obtained between the repeat and the base electric field during and before production, respectively for the Born, TMA, and EBA for model 1.*

The relative errors in magnitude and phase are generally small when Extended Born is used to approximate the T-matrix approximation compared to the Born as illustrated in table 3. The errors in magnitude increased by 2.46 % and decreased by 1.31 % from 5 years to 10 years of production for Born and extended Born, respectively.

However, it is also shown that the phase decreased as production occurs by 9.79 % and increased by 1.2 % for Born and Extended Born, respectively. In figure 5.5 (a) and (c), the anomaly in amplitude increase as production progresses as expected and the phase difference tends to zero along the entire horizontal axis except in the reservoir location for the approximations considered before production started. However, there was a phase shift after the saline water was injected (figure 5.6).

5.1.3 Model 2

To handle larger models at a low frequencies such as 0.25 Hz, the cell size needs to be increased (Streich 2009). From figure 5.1, for a larger model the optimal grid size in model 1 was doubled to $50\times50\times50m^3$ and the number of cells to be $30\times30\times1$ grids. The modeling was done using some parameters from table 2, with a mesh of 403 receivers and conductivities of 0.38 S/m and 0.28 S/m for injected fluid and hydrocarbon, respectively. A bigger model was considered to determine its effects on the magnitude and phase of the anomalous electric field. The data set in magnitude and phase acquired before and during production for the middle row were plotted in figure 5.7 to illustrate the effects of flooding on the reservoir; (a) and (b), before; (c) and (d), after 5 years; and, (e) and (f) after 10 years of production. The magnitude of the electric field decreases as more saline water is injected (figure 5.7). This is attributed to an increase in conductivity of the reservoir as more conductive water is added there by decreasing the contrast. There is a phase shift in the vicinity of the reservoir but the different approximations converge far from the reservoir. Born approximation is observed to be less accurate although the deviation decrease as the water front floods to the right of the reservoir. The phase difference for Born, TMA and EBA agree at far as production continues (figure 5.8).

The relative errors in magnitude and phase are generally small (0.20 %) when the Extended Born is used to approximate the T-matrix approximation compared to the Born (17.36 %) as shown in table 3. The errors in magnitude decreased by 4.79 % and 0.09 % from 5 years to 10 years of production for Born and extended Born, respectively. However, it is also shown that the phase decreased as production occurred by 29.17 % and increased by 0.02 % for Born and Extended Born, respectively. Figure 5.8 shows the anomaly in the amplitude and phase for the electric fields before and during production of the hydrocarbon. The magnitude and phase before injection were subtracted from that of the monitor survey. Generally, the anomaly in amplitude decreased with increase in the time of production as expected and the phase difference tends to zero along the entire horizontal axis except in the reservoir location for the approximations considered before production started. However, there was a phase shift after the saline water was injected as shown in figure 5.8 (d), though the Born still exhibited higher phase differences.

The similarity observed in the TMA and EBA data behaviour can be explained by the fact that the approximations are based on the T-matrix and the depolarization tensor calculation, which are independent of the background field. Therefore, these approximations cannot take into account properly the background field which cause discrepancies in these approximations (Zhdanov, Dmitriev et al. 2000). The EBA and TMA gave a large phase difference in the location of the reservoir before injection which attenuated faster as time of fliud injetion increased as shown in figure 5.8. The strength and resolution of the time-lapse largely depend on the variation of the base and repeat responses for varying fluid saturation (Bhuyian, Landrø et al. 2012). Therefore, the difference between the base and the repeat data results in enhanced time-lapse anomalies.

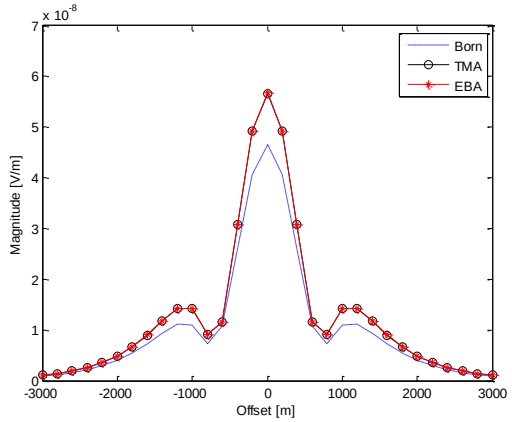

(a) ΔE_x at t_0 (Before)

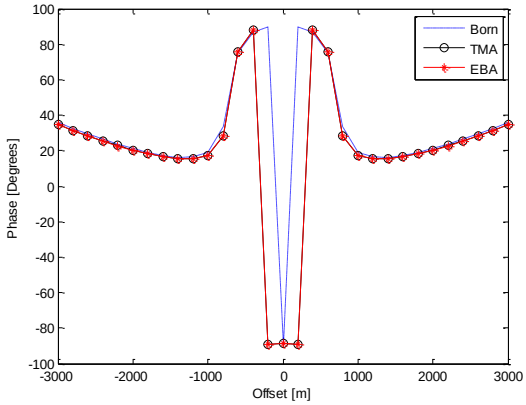

(b) θ_x at t_0 (Before)

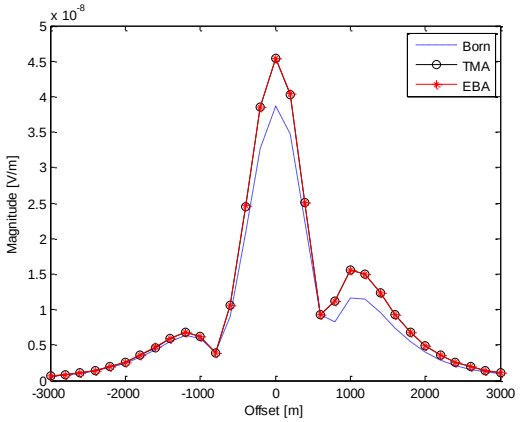

(c) ΔE_x at t_1 (After 5 years)

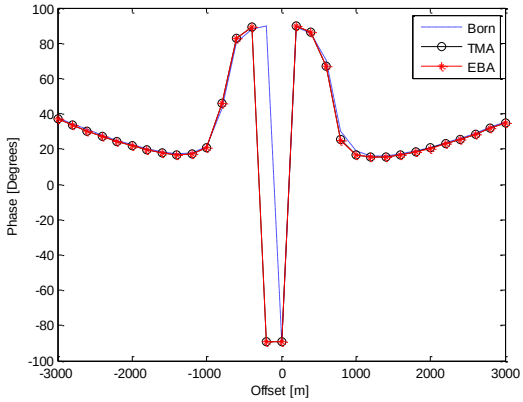

(d) θ_x at t_1 (After 5 years)

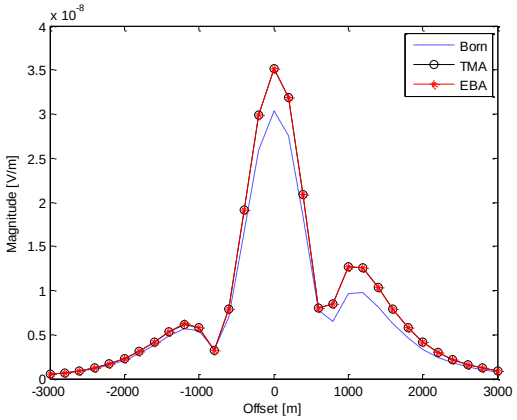

(e) ΔE_x at t_2 (After 10 years)

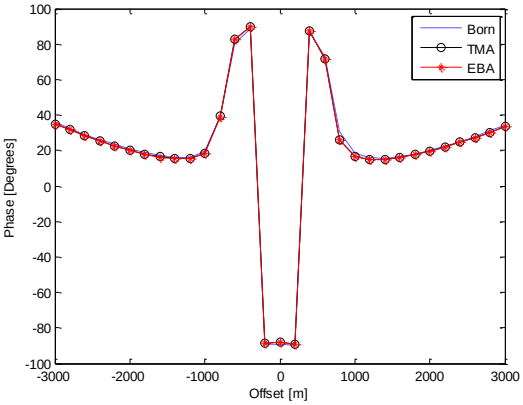

(f) θ_x at t_2 (After 10 years)

Figure 5.7: *Magnitude (left) and phase (right) for the anomalous electric field; (a)- (b) before, (c) - (d) after 5 years and (e) - (f) after 10 years of production for model 2 using the frequency of 0.25 Hz The injected water and hydrocarbon have conductivities of 0.38 S/m and 0.28 S/m.*

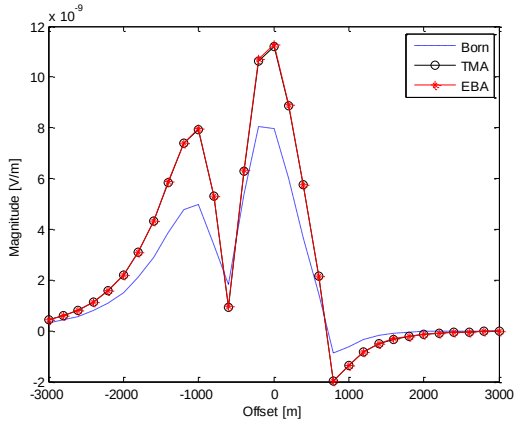

(a) ∂E_0 (between t_0 and t_1)

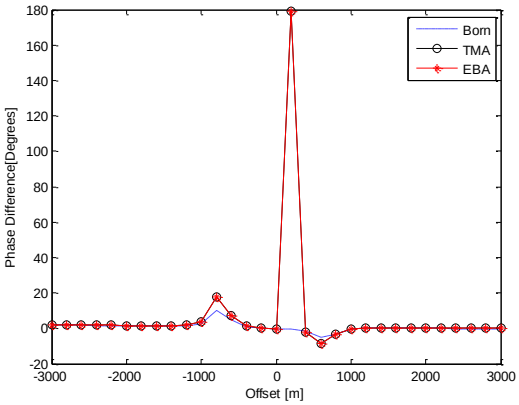

(b) $\delta\theta_0$ (between t_0 and t_1)

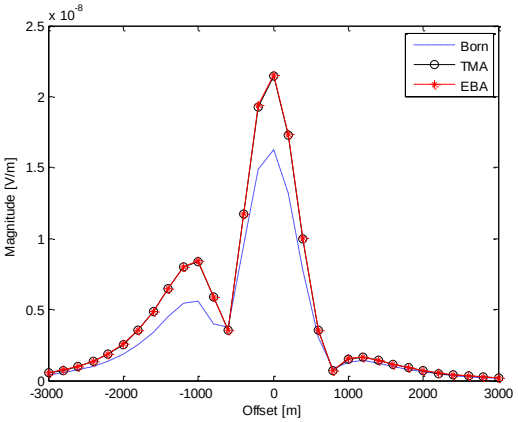

(c) ∂E_1 (between t_0 and t_2)

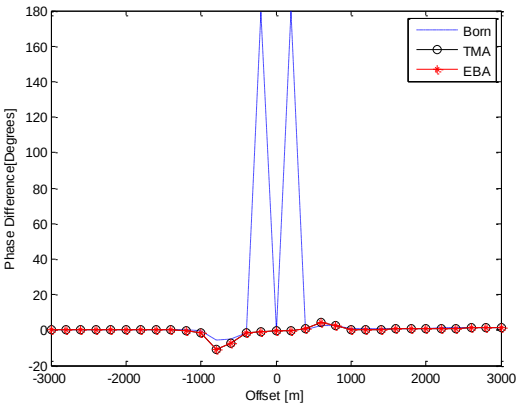

(d) $\delta\theta_1$ (between t_0 and t_2)

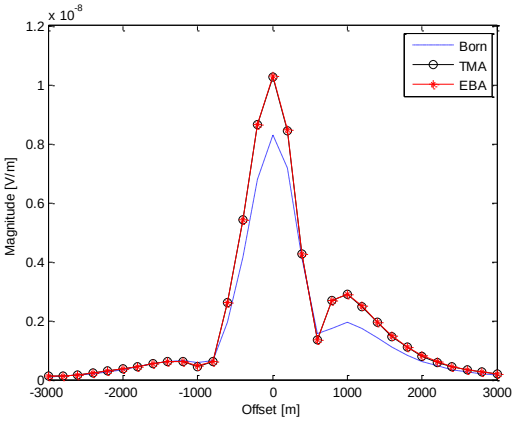

(e) ∂E_2 (between t_1 and t_2)

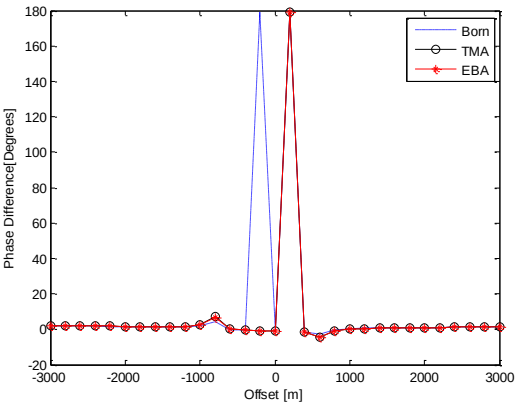

(f) $\delta\theta_2$ (between t_1 and t_2)

Figure 5.8: *Time- lapse Magnitude (left panel) and phase (right panel) for anomalous field; (a) - (b) before; (c) - (d) after 5 years, and; (e) - (f) after 10 years of production for model 2 with conductivities of 0.38 S/m (water) and 0.28 S/m (hydrocarbon).*

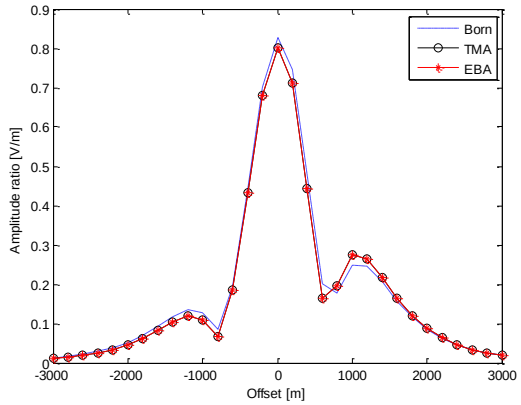

(a) A_R (between t_0 and t_1)

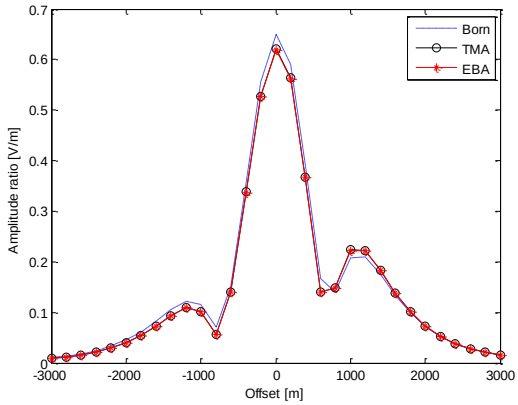

(b) A_R (between t_0 and t_2)

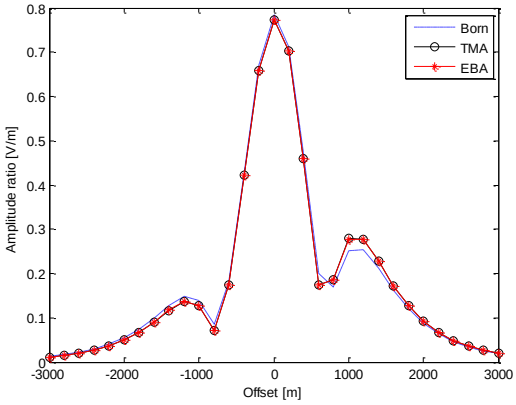

(c) A_R (between t_2 and t_1)

Figure 5.9: *The plots for amplitude ratio between the repeat and the base anomalous electric field for model 2 containing water and hydrocarbon with conductivities 0.38 S/m and 0.28 S/m, respectively before and during production for the Born, TMA, and EBA.*

From figure 5.9, the Born approximation tends to have higher amplitude ratio than the EBA and TMA. The ratio like the magnitude, decreased as the water front moved to the right of the reservoir. The amplitude ratio irrespective of the approximation, is used to locate the presence of the reservoir where the ratio is high.

The two models have been compared and found out that the errors in the Born and the Extended Born approximations relative to the TMA decreased when a relatively larger model with bigger grids was considered compared to the smaller model. The magnitude also reduced when a smaller model was considered. Therefore, while modeling the effort should not only be on the number of grid cells but also on the size of the reservoir in addition to the grid volume already discussed in sections above.

5.2 Inverse Theory

In geophysical practice, inversion is a set of methods used to extract useful inferences about the model parameters from geophysical measurements, that is; electromagnetic field behaviors. According to Martin Čuma, Masashi Endo et al. (2008), the theory basically involves the minimization of the misfit between observed field data and data calculated by forward model based on structural properties from the inversion. It aims at; (1) organizing the techniques to bring out their underlying similarities and pin down their differences; and (2) dealing with the fundamental question of the limits of information from given data (Menke 1989).

Inverse problem

5.2.1 Least Squares Solution

This method estimates the solution of an inverse problem by finding the model parameters that minimize a particular measure of the length of the estimated data, $\boldsymbol{d}_{est}$ (Menke 1989). The least squares method uses the L_2-norm to quantify the length and can be easily extended to the general linear inverse problem. The total prediction error or the misfit is defined (Menke 2012) as

$$\boldsymbol{E}_{err} = \boldsymbol{e}^T\boldsymbol{e} = \left(\boldsymbol{d} - A\boldsymbol{m}\right)^T\left(\boldsymbol{d} - A\boldsymbol{m}\right) \tag{5.6}$$

In index notation, the total prediction error is given as,

$$\boldsymbol{E}_{err} = \sum_i^N \left(d_i - \sum_j^M \mathrm{A}_{ij} m_j \right)\left(d_i - \sum_k^M \mathrm{A}_{ik} m_k \right) \tag{5.7}$$

By expanding equation (5.7) and reversing the order of summation,

$$\boldsymbol{E}_{err} = \sum_j^M \sum_k^M m_j m_k \sum_i^N \mathrm{A}_{ij}\mathrm{A}_{ik} - 2\sum_j^M m_j \sum_i^N \mathrm{A}_{ij} d_i + \sum_i^N d_i d_i \tag{5.8}$$

To minimize equation (5.8) the total error with respect to m_q, one of the model parameters, $\frac{\partial E_{err}}{\partial m_q} = 0$ is computed (Menke 2012), as

$$\frac{\partial E_{err}}{\partial m_q} = 2\sum_k^M m_k \sum_i^N \mathrm{A}_{iq}\mathrm{A}_{ik} - 2\sum_i^N \mathrm{A}_{iq} d_i, \tag{5.9}$$

with m_i and m_j as the independent variables, and their derivative is zero unless for $i = j$.
By writing equation (5.9) in matrix notation it then follows that,

$$\mathbf{A}^T\mathbf{A}\boldsymbol{m} - \mathbf{A}^T\boldsymbol{d} = 0 \qquad (5.10)$$

where $\mathbf{A}^T\mathbf{A}$ is a square $3N \times 3N$ matrix that multiplies a vector $\boldsymbol{m}$ of length $3N$; $\mathbf{A}^T\boldsymbol{d}$ is a vector of length 3N. Thus, equation (5.10) is a square matrix equation for the unknown model parameters. If the inverse of $\mathbf{A}^T\mathbf{A}$ exists, then

$$\boldsymbol{m}_{est} = (\mathbf{A}^T\mathbf{A})^{-1}\mathbf{A}^T\boldsymbol{d} \qquad (5.11)$$

with $\boldsymbol{m}_{est}$ the least squares solution for an inverse problem that has no exact solution. This method fails for problems with nonunique solutions. The least squares solution can take on any of the following criterion;

a) Underdetermined problems when there are more unknowns than data,
b) Evendetermined with just enough information to determine the model parameters,
c) Overdetermined problems when too much information is contained in the equation $\mathbf{A}\boldsymbol{m} = \boldsymbol{d}$. The least squares method is employed in this case to select the best approximate solution.

5.2.2 Tikhonov Regularization

This is one of the most successful and most popular regularization methods to solve discrete ill-posed problems with error-contaminated data such as the Fredholm Integral Equation. The Tikhonov regularized minimum norm solution of equation $\boldsymbol{d} = \mathbf{A}\boldsymbol{m} + \varepsilon$, is the vector $m_\lambda \in \mathbb{R}^n$ that minimizes the expression (Hansen 2010),

$$\|\mathbf{A}\boldsymbol{m} - \boldsymbol{d}\|_2^2 + \lambda^2 \|\boldsymbol{m}\|_2^2 \qquad (5.12)$$

with $\lambda > 0$ the regularization parameter that controls the weight between the two ingredients of the criterion function. According to (Hansen 2010);

a) *The first* term- $\|\mathbf{A}\boldsymbol{m} - \boldsymbol{d}\|_2^2$ measures the goodness-of-fit; that is, how well the solution $\mathbf{m}$ predicts the given (noisy) data $\mathbf{d}$. When the term is too large, $\mathbf{m}$ is a poor solution.
b) *The second* term- $\|\boldsymbol{m}\|_2^2$ measures the regularity of the solution. If the norm of $\mathbf{m}$ can be controlled, then the large noise components can be suppressed.
c) The balance between the two terms is controlled by the factor λ^2. The larger the λ, the more weight is given to the minimum of the solution norm, $\|\boldsymbol{m}\|_2^2$ and thus the regularity of the solution. For small λ, more weight is given to fitting the noisy data, resulting in solutions that are less regular.

For arbitrary vectors, the Tikhonov problem in equation (5.12) can be reformulated (Hansen 2010) as

$$\min_{m} \left\| \begin{pmatrix} \mathbf{A} \\ \lambda \boldsymbol{I} \end{pmatrix} \boldsymbol{m} - \begin{pmatrix} \boldsymbol{d} \\ 0 \end{pmatrix} \right\|_2 \qquad (5.13)$$

which clearly indicates a linear least squares problem. The normal equations (5.13) (Hansen 2010), takes the form

$$\begin{pmatrix} \mathbf{A} \\ \lambda \boldsymbol{I} \end{pmatrix}^T \begin{pmatrix} \mathbf{A} \\ \lambda \boldsymbol{I} \end{pmatrix} m = \begin{pmatrix} \mathbf{A} \\ \lambda \boldsymbol{I} \end{pmatrix}^T \begin{pmatrix} \boldsymbol{d} \\ 0 \end{pmatrix} \qquad (5.14)$$

The equation above can then simplify to

$$(\mathbf{A}^T \mathbf{A} + \lambda^2 \boldsymbol{I}) \boldsymbol{m} = \mathbf{A}^T \boldsymbol{d} \qquad (5.15)$$

And the estimated model parameter can be obtained (Hansen 2010, Menke 2012) as

$$\boldsymbol{m}_\lambda = (\mathbf{A}^T \mathbf{A} + \lambda^2 \boldsymbol{I})^{-1} \mathbf{A}^T \boldsymbol{d} \qquad (5.16)$$

5.2.3 Regularization Parameter

Since the solution of an ill-posed inverse problem may result in unstable, unrealistic models, the regularization theory provides guidance for overcoming this difficulty (Zhdanov 2009). Any regularization algorithm is based on the approximation of the non-continuous inverse operator $\mathbf{A}^{-1}$ by the family of continuous inverse operators $\mathbf{A}_\lambda^{-1}(\boldsymbol{d})$ that depend on the regularization parameter λ. The regularization parameter controls the relationship between the regularization and perturbation errors. The choice of the regularization parameter $\lambda > 0$, is not an easy task (Hansen 2010); and the method for choosing the regularization parameter should seek to minimize the errors in the regularized solution. It should however be noted that, both the perturbation errors and the regularization errors are always present in the regularization solution and their size depends on the regularization parameter (Hansen 2010).

5.2.4 L-Curve Method

One way of obtaining the regularization parameter is the use of the L-curve method. The L-curve is a parametric plot of ($\|\mathbf{A}\boldsymbol{m} - \boldsymbol{d}\|_2^2$, $\|\boldsymbol{m}_\lambda\|_2$), where $\|\mathbf{A}\boldsymbol{m} - \boldsymbol{d}\|_2^2$, measures the size of the regularized solution, and $\|\boldsymbol{m}_\lambda\|_2$ the corresponding residual (P. C. Hansen and O'Leary 1993, Hansen 2010). As noted in (P. C. Hansen and O'Leary 1993), the L-curve has a distinct L-shaped corner located exactly where the solution $\boldsymbol{m}_\lambda$ changes in nature from being dominated by regularization errors (flat part) to being dominated by the errors in the right side (vertical part).

The L-curve method considers the computation of the corner being a well-defined numerical problem, and this method is not "fooled" by correlated errors (P. C. Hansen and O'Leary

1993). The corner of the curve can be visualized in two ways; 1) as a point closest to the origin; 2) as a point on the curve where the curvature is a maximum.

When a graph is plotted in linear scale, it becomes difficult to inspect its features because of the large range of values for the two norms. However, to distinguish the signal from the noise, the log-log scale is used (Hansen 2010). This scale also emphasizes "flat" parts of the L-curve where the variation in either $\|\mathbf{A}\boldsymbol{m}-\boldsymbol{d}\|_2^2$ or $\| \boldsymbol{m}_\lambda \|_2$ is small compared to the variation in the other variable, thus emphasizing the corner of the curve.

5.2.5 Implementation of Inversion

From the general discrete linear equation given (Menke 2012) as,

$$\mathbf{d} = \mathbf{A}\mathbf{m}, \tag{5.17}$$

where

$$\mathbf{d} = \Delta\mathbf{E} = \left[\Delta\mathbf{E}_1, \Delta\mathbf{E}_2, ..., \Delta\mathbf{E}_N\right]^T \tag{5.18}$$

$$\mathbf{m} = \Delta\boldsymbol{\sigma} = \left[\Delta\boldsymbol{\sigma}_1, \Delta\boldsymbol{\sigma}_2, ..., \Delta\boldsymbol{\sigma}_M\right]^T$$

For electromagnetic modeling, equation (5.17) is treated as,

$$\Delta\mathbf{E} = \mathbf{A}\Delta\boldsymbol{\sigma} \tag{5.19}$$

where $\Delta\mathbf{E}$ and $\Delta\boldsymbol{\sigma}$ are respectively, the data and model parameters for the anomalous electric field and anomalous conductivity. And $\mathbf{A}$ is an operator obtained after multiplying the background field with the Green's tensor for the scattering volume.

During inversion, the main aim is to obtain the estimates of the model parameters given the observed data. Therefore, equation (5.19) then becomes,

$$\Delta\boldsymbol{\sigma} = \mathbf{A}^H \Delta\mathbf{E} \tag{5.20}$$

where $\mathbf{A}^H$ the generalized inverse operator is given as,

$$\mathbf{A}^H = \begin{cases} \mathbf{A}^{-1}; & \text{if inverse exists} \\ (\mathbf{A}^T\mathbf{A} + \lambda^2\mathbf{I})^{-1}\mathbf{A}^T; & \text{elsewhere} \end{cases} \tag{5.21}$$

In electromagnetic inversion the solutions are always non unique; therefore, the generalized operator matrix is considered to take the form, (Menke 2012)

$$\mathbf{A}^H = (\mathbf{A}^T\mathbf{A} + \lambda^2\mathbf{I})^{-1}\mathbf{A}^T \tag{5.22}$$

where λ is the regularization parameter. For implementation of the inverse of the electromagnetic fields, equation (5.20) takes the form $\mathbf{m}_\lambda = (\mathbf{A}^T\mathbf{A} + \lambda^2\mathbf{I})^{-1}\mathbf{A}^T\mathbf{d}$ from equation (5.16), where $\mathbf{m}_\lambda$ are the estimated model parameters which need to be calculated.

5.3 Inversion of CSEM Data

The actual detection of a potential petroleum reservoir is achieved through inversion of the EM data acquired in the receivers (Bakr and Mannseth 2009). Anomalous electric field for the Born, TMA and EBA were considered for different contrasts when a reservoir was under production. Inversion of CSEM data set acquired at each stage of production was independently inverted. The Born inversion was done to test the forward modeling data from Born, T-matrix and Extended Born approaches, (Born-Born, TMA-Born and EBA- Born).

5.3.1 Model 3

From the discretization of the integral equation under the different approximations, equation (3.37), (3.53), and (3.73) were obtained in chapter 3 for Born, TMA and EBA, respectively. The model parameter $\boldsymbol{m} = \Delta\sigma$, data parameter $\boldsymbol{d} = \Delta E$ and $A = G_{rv} \times E^b$ are related by the expression $\boldsymbol{d} = A\boldsymbol{m}$. The parameters from sections above were considered but now using a grid structure with 403 receivers in total that are arranged in 13 rows each with 31 receivers. The reservoir still had $30 \times 30 \times 1$ cubic grids. As noted in Bhuyian, Landrø et al. (2012), the grid geometry data facilitates mapping of modeled time-lapse anomalies. Thus the solution has more model parameters than the data parameters leading to nonuniqueness of the inverse problem. The regularization parameter is therefore important since the solution is non-unique and the Tikhonov regularization parameter was used. The study was limited to a linear inversion (Born) at the expense of the non-linear one. The *EMforward.m* and *EMinversion.m* were used for the forward and inverse modeling schemes.

The monitoring was divided into three different contrasts (low, moderate and high) to compare the results from the reservoir before and during production. Low, moderate and high contrasts were considered as 0.05 S/m, 0.25 S/m and 0.49 S/m, respectively for the hydrocarbon while keeping that of the injected fluid constant (0.5 S/m) as the background. The figures 5.10, 5.12, and 5.14, represent the contrast for the true model (left panel), and the Born inversion on the Born (second panel), the EBA (third panel), and the TMA (right panel) data before and during production. Figures 5.11, 5.13, and 5.15 represent the Born inversion on synthetic data generated using the Born (left panel), the Extended Born (middle panel) and the T-matrix (right panel) approximations. For low contrast before production, all the approximations agree since the hydrocarbon was the only pore-filling fluid in the reservoir (figure 5.10). There were no noticeable differences between the true and inverted models for a particular stage of production. This therefore implies that all the approximations agree for relatively small contrasts. Figure 5.11 shows results of contrast for the true and estimated model parameters which were also seen to give similar results for a particular production period. As the contrast increased (figure 5.12), distorted inverted images were observed for

both TMA and EBA. True and estimated model parameters gave similar values as shown in figures 5.13. The TMA gave better estimate results than the EBA consistent with the observation when the magnitude was plotted. For higher contrasts (figure 5.14), the T-matrix and the Extended Born failed before and after 5 years of production but gave results after 10 years of production. This feature exhibited with the T-matrix and the Extended Born is quite unique in monitoring of fluid injection, hydrocarbon storage (CO_2) and Enhance Oil Recovery.

Therefore, the TMA and the EBA could be better estimates of the water front as the production of hydrocarbon progresses. This is the same technique used in monitoring of the CO_2 storage and leakages within the reservoir. For all the Born inverted data to generate the estimated model, a more realistic model is produced than the simplified true model that was assumed since they indicate a transition zone (where both fluids exist). This is normally what happens during water flooding. It should be noted from figure 5.10 that the Born shows a significant transition zone than the TMA and the EBA approximations. Lien and Mannseth (2008) noted that the quality of the signal is influenced by the errors in the measured fields. There was a lot of noise that was simulated into the code that made the prediction of the good model a difficult. The need to add synthetic noise in the data is need to mimic the actual data. The EBA gave better results as the estimated model parameters matched closely the predicted as the depletion of the hydrocarbon proceeded.

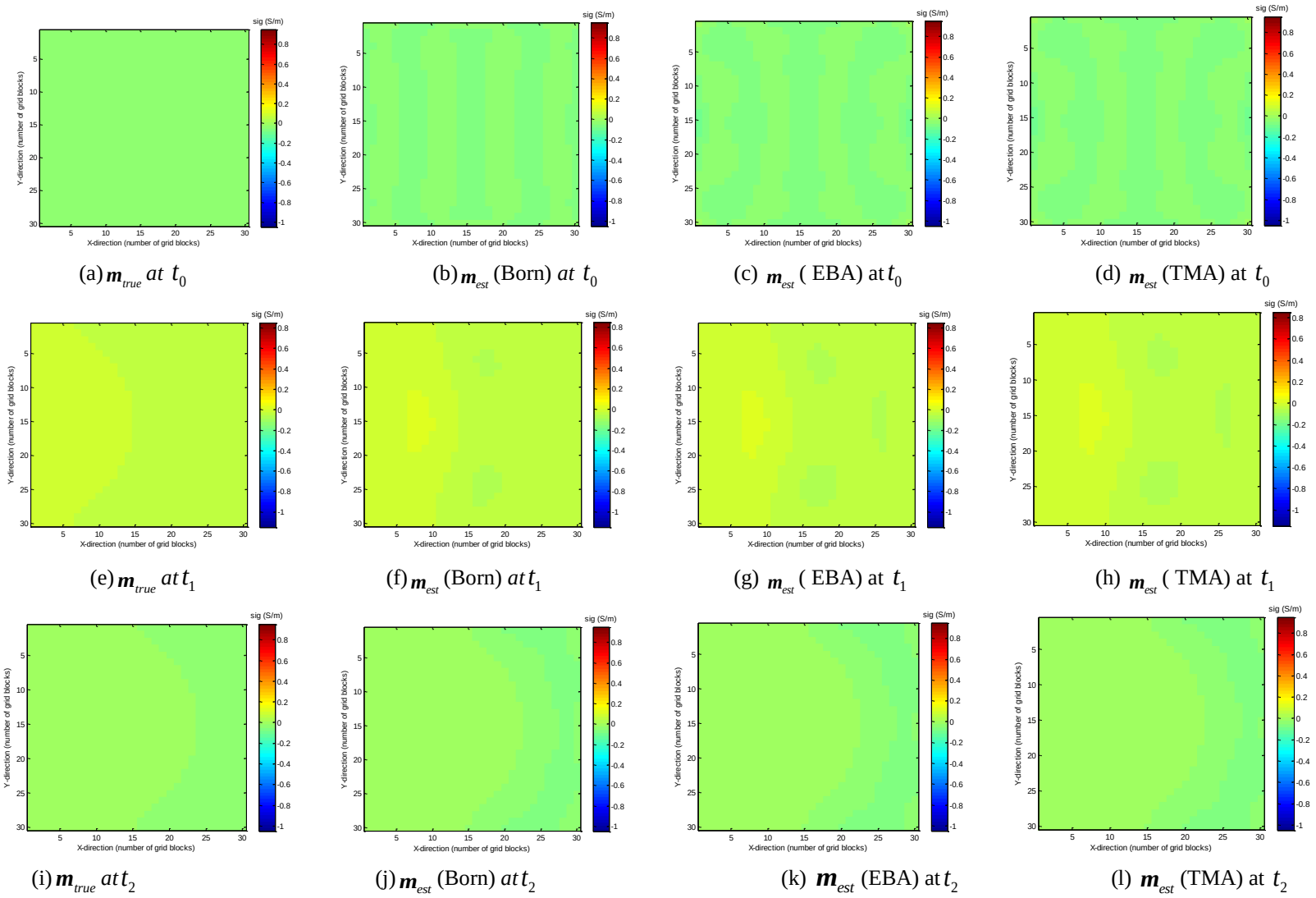

(a) $\boldsymbol{m}_{true}$ *at* t_0 (b) $\boldsymbol{m}_{est}$ (Born) *at* t_0 (c) $\boldsymbol{m}_{est}$ (EBA) at t_0 (d) $\boldsymbol{m}_{est}$ (TMA) at t_0

(e) $\boldsymbol{m}_{true}$ *at* t_1 (f) $\boldsymbol{m}_{est}$ (Born) *at* t_1 (g) $\boldsymbol{m}_{est}$ (EBA) at t_1 (h) $\boldsymbol{m}_{est}$ (TMA) at t_1

(i) $\boldsymbol{m}_{true}$ *at* t_2 (j) $\boldsymbol{m}_{est}$ (Born) *at* t_2 (k) $\boldsymbol{m}_{est}$ (EBA) at t_2 (l) $\boldsymbol{m}_{est}$ (TMA) at t_2

Figure 5.10 : *Plots for true (left panel) and inverted synthetic data using Born inversion on Born (second second), EBA (third panel) and TMA(right panel) for a reservoir before (a - d), after 5 years (e -h) and after10 years (i- l) of production for low contrast (-0.05 S/m).*

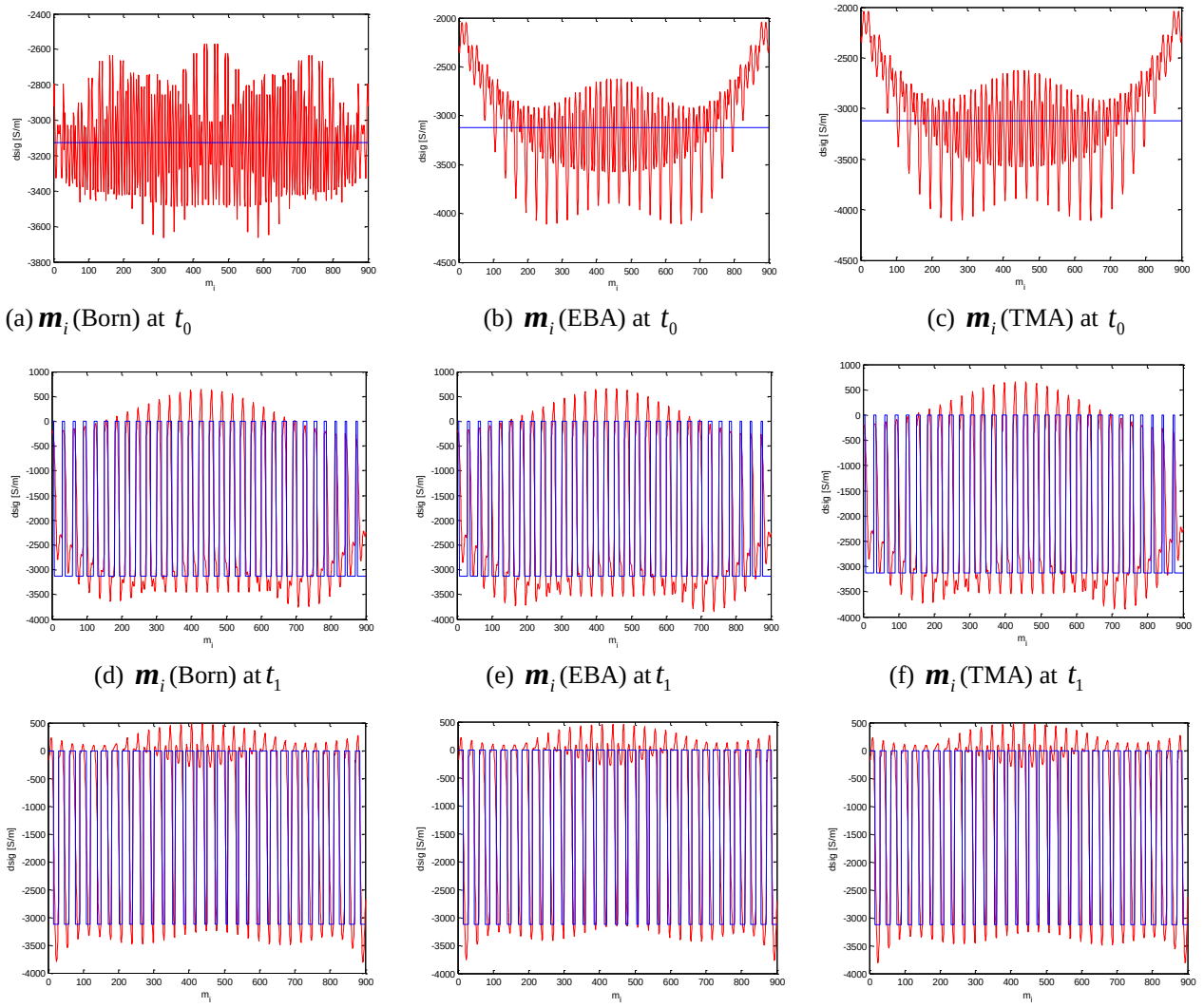

(a) $\boldsymbol{m}_i$ (Born) at t_0 (b) $\boldsymbol{m}_i$ (EBA) at t_0 (c) $\boldsymbol{m}_i$ (TMA) at t_0

(d) $\boldsymbol{m}_i$ (Born) at t_1 (e) $\boldsymbol{m}_i$ (EBA) at t_1 (f) $\boldsymbol{m}_i$ (TMA) at t_1

(g) $\boldsymbol{m}_i$ (Born) at t_2 (h) $\boldsymbol{m}_i$ (EBA) at t_2 (i) $\boldsymbol{m}_i$ (TMA) at t_2 Low contrast

Figure 5.11:*Born inversion on synthetic data generated using Born, EBA and TMA .The plots indicates the true (blue line) and estimated (red line) model parameters before (a - c), after 5 years(d - f) and after 10 years (g - i) of production for low contrast (-0.05 S/m).*

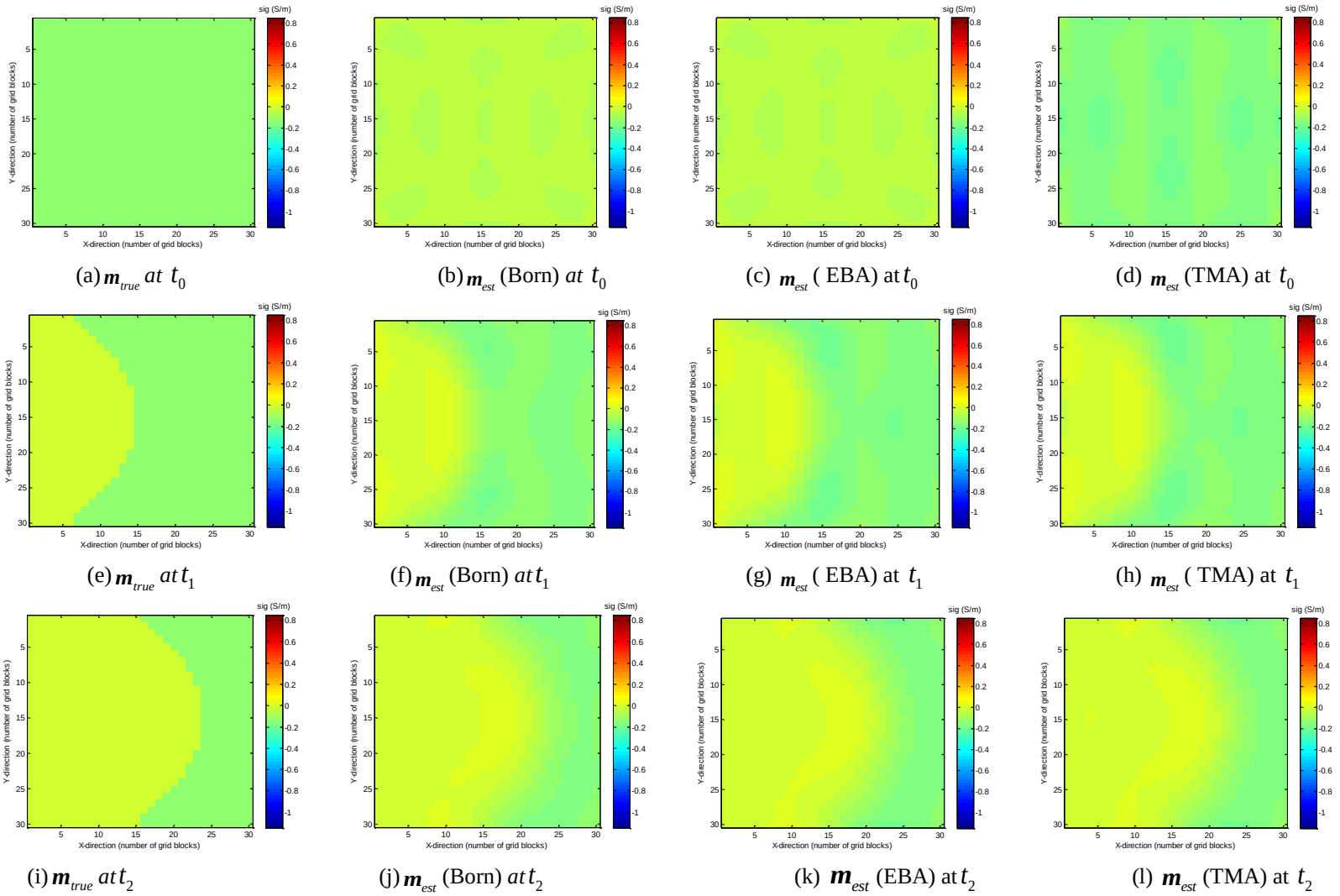

(a) $\boldsymbol{m}_{true}$ *at* t_0 (b) $\boldsymbol{m}_{est}$ (Born) *at* t_0 (c) $\boldsymbol{m}_{est}$ (EBA) at t_0 (d) $\boldsymbol{m}_{est}$ (TMA) at t_0

(e) $\boldsymbol{m}_{true}$ *at* t_1 (f) $\boldsymbol{m}_{est}$ (Born) *at* t_1 (g) $\boldsymbol{m}_{est}$ (EBA) at t_1 (h) $\boldsymbol{m}_{est}$ (TMA) at t_1

(i) $\boldsymbol{m}_{true}$ *at* t_2 (j) $\boldsymbol{m}_{est}$ (Born) *at* t_2 (k) $\boldsymbol{m}_{est}$ (EBA) at t_2 (l) $\boldsymbol{m}_{est}$ (TMA) at t_2

Figure 5.12: *Plots for true (left panel) and inverted synthetic data using Born inversion on Born (second second), EBA (third panel) and TMA(right panel) for a reservoir before (a - d), after 5 years (e -h) and after10 years (i- l) of production for moderate contrast (-0.25 S/m).*

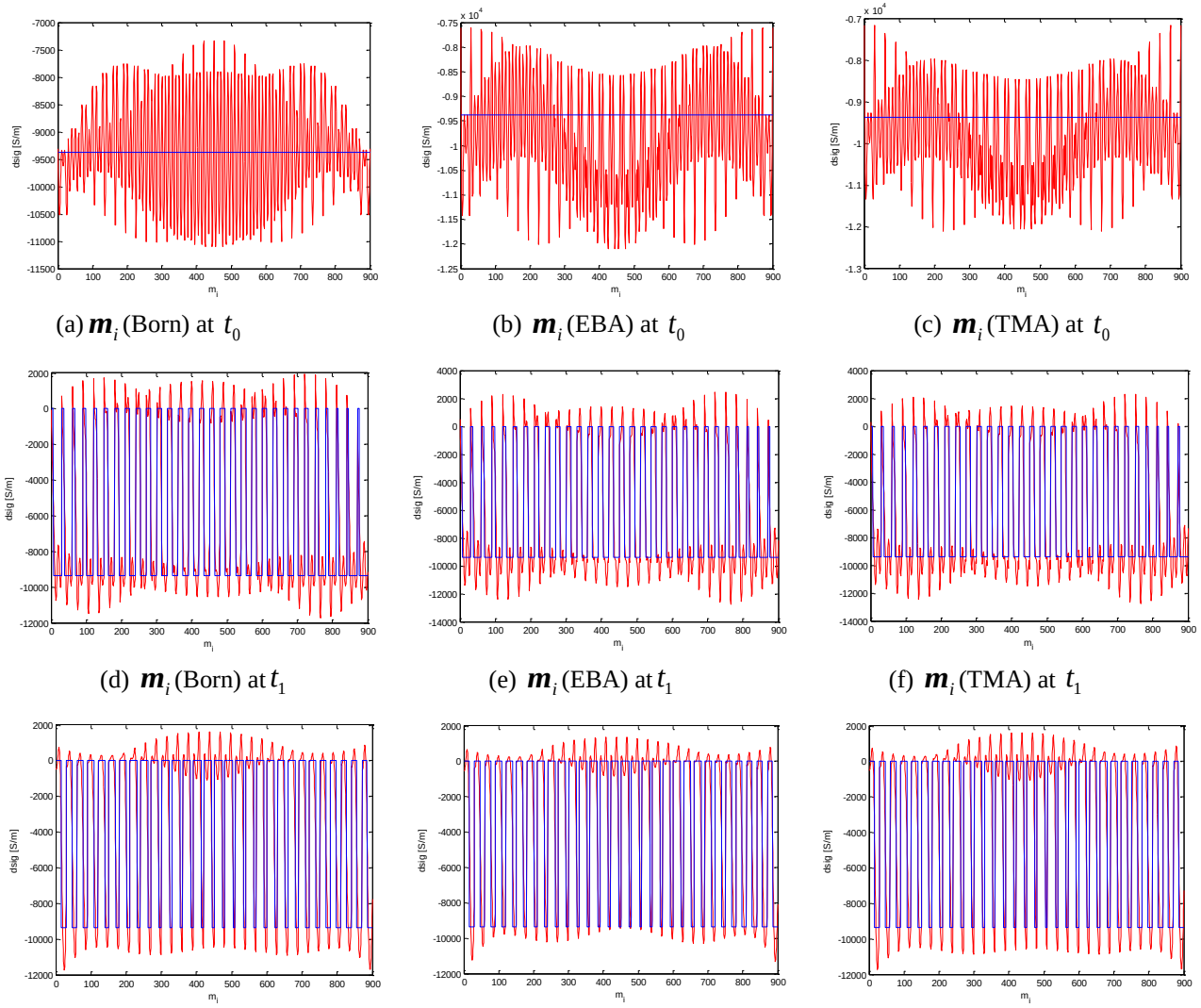

(a) $\boldsymbol{m}_i$ (Born) at t_0 (b) $\boldsymbol{m}_i$ (EBA) at t_0 (c) $\boldsymbol{m}_i$ (TMA) at t_0

(d) $\boldsymbol{m}_i$ (Born) at t_1 (e) $\boldsymbol{m}_i$ (EBA) at t_1 (f) $\boldsymbol{m}_i$ (TMA) at t_1

(g) $\boldsymbol{m}_i$ (Born) at t_2 (h) $\boldsymbol{m}_i$ (EBA) at t_2 (i) $\boldsymbol{m}_i$ (TMA) at t_2

Figure 5.13:*Born inversion on synthetic data generated using Born, EBA and TMA .The plots indicates the true (blue line) and estimated (red line) model parameters before (a - c), after 5 years(d - f) and after 10 years (g - i) of production for moderate contrast (-0.25 S/m).*

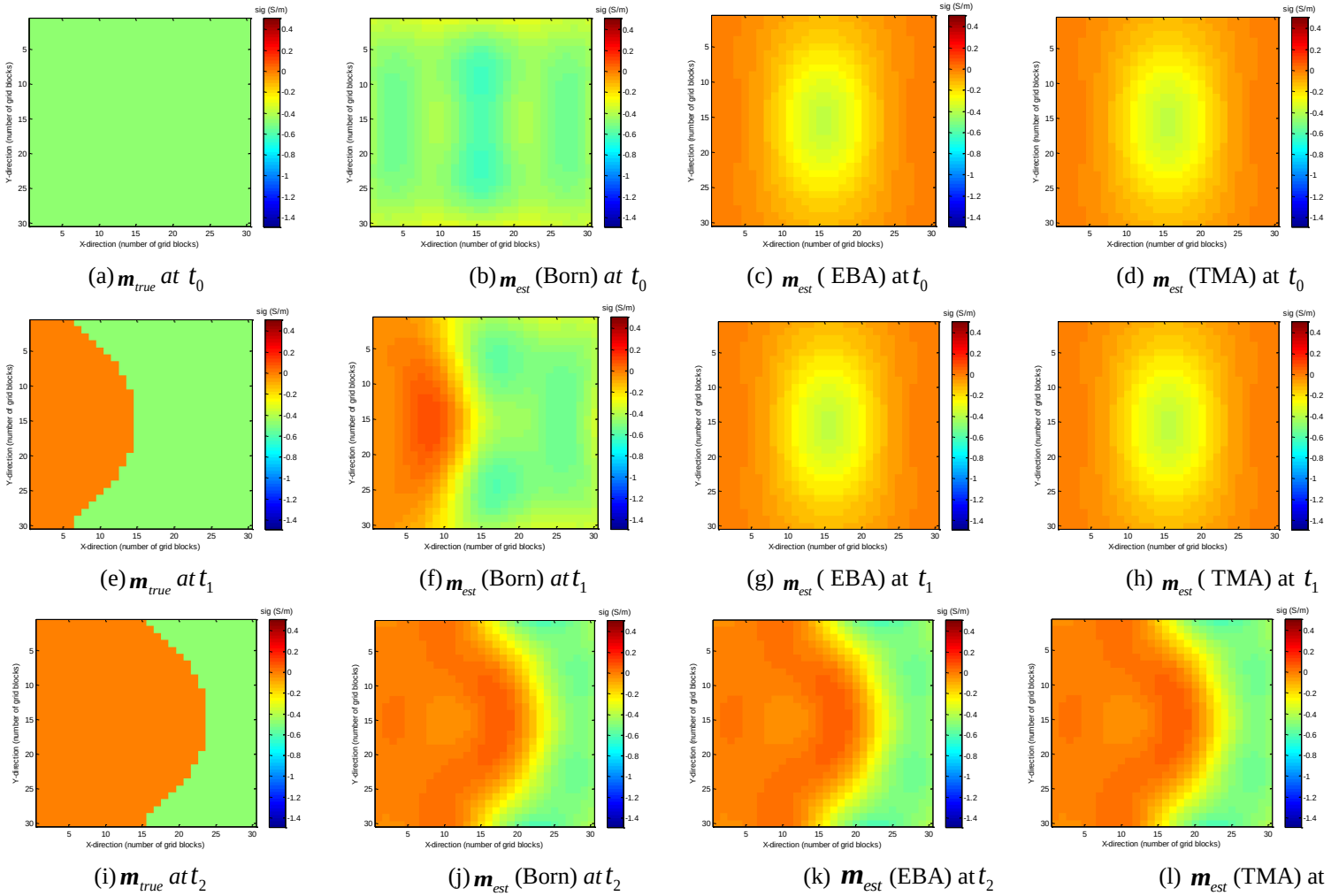

(a) $\boldsymbol{m}_{true}$ *at* t_0 (b) $\boldsymbol{m}_{est}$ (Born) *at* t_0 (c) $\boldsymbol{m}_{est}$ (EBA) at t_0 (d) $\boldsymbol{m}_{est}$ (TMA) at t_0

(e) $\boldsymbol{m}_{true}$ *at* t_1 (f) $\boldsymbol{m}_{est}$ (Born) *at* t_1 (g) $\boldsymbol{m}_{est}$ (EBA) at t_1 (h) $\boldsymbol{m}_{est}$ (TMA) at t_1

(i) $\boldsymbol{m}_{true}$ *at* t_2 (j) $\boldsymbol{m}_{est}$ (Born) *at* t_2 (k) $\boldsymbol{m}_{est}$ (EBA) at t_2 (l) $\boldsymbol{m}_{est}$ (TMA) at t_2

Figure 5.14: *Plots for true (left panel) and inverted synthetic data using Born inversion on Born (second second), EBA (third panel) and TMA(right panel) for a reservoir before (a - d), after 5 years (e -h) and after10 years (i- l) of production for high contrast (-0.49S/m).*

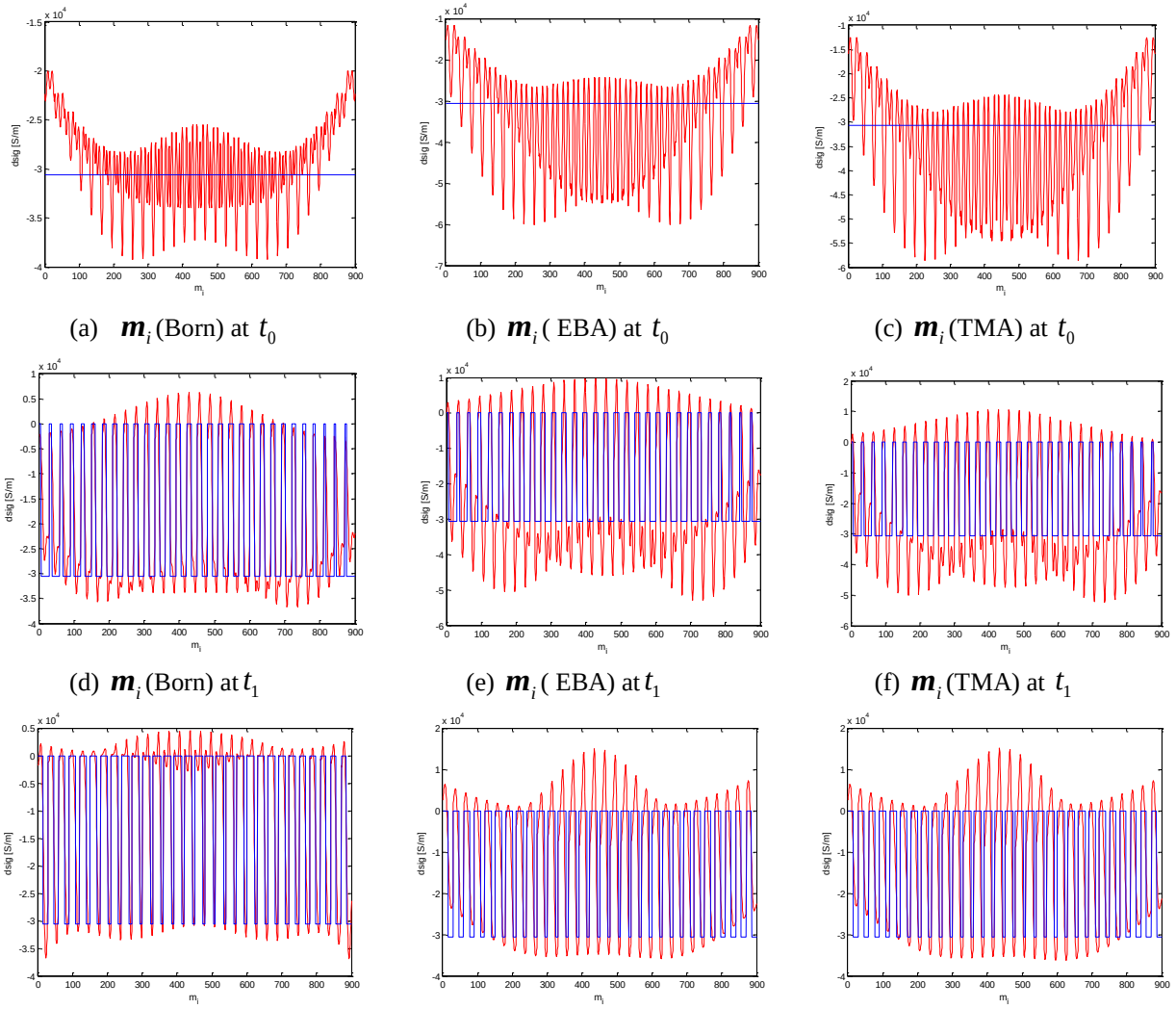

(a) $\boldsymbol{m}_i$ (Born) at t_0 (b) $\boldsymbol{m}_i$ (EBA) at t_0 (c) $\boldsymbol{m}_i$ (TMA) at t_0

(d) $\boldsymbol{m}_i$ (Born) at t_1 (e) $\boldsymbol{m}_i$ (EBA) at t_1 (f) $\boldsymbol{m}_i$ (TMA) at t_1

(g) $\boldsymbol{m}_i$ (Born) at t_2 (h) $\boldsymbol{m}_i$ (EBA) at t_2 (i) $\boldsymbol{m}_i$ (TMA) at t_2

Figure 5.15*: Born inversion on synthetic data generated using Born, EBA and TMA .The plots indicates the true (blue line) and estimated (red line) model parameters before(a - c), after 5 years(d - f)and after 10 years (g - i) of production for high contrast (-0.49 S/m).*

6 Discussion and Conclusion

6.1 Discussion

In modeling, the reservoir parameters affect the solution of the approximation considered to the integral equation. The synthetic data was modeled numerically using MATLAB codes for approximations to the integral equation developed for Extended Born, T-matrix and the Born modified from Stav (2010). The hydrocarbon reservoir always have very low conductivity values compared to its background, thus having negative contrast conductivity (Zhdanov 2009). It has been discussed in chapter 4 how the different parameters affect; (1) the magnitude and phase of the anomalous electric field; (2) the validity of the Born, Extended-Born and T-matrix approximations, and; (3) the nature of the solutions obtained. It is true that the magnitude of the anomalous electric field increases with increase in the contrast. The T-matrix and Extended Born give better results than the Born as contrast increases. The TMA and EBA have the T-matrix and the depolarization tensors that are non-linear in contrast; accounting for the increase in magnitude than the Born that is linear. It has also been shown that the T-matrix and Extended Born approaches to the integral equation approximation for a large number of grid cells are computationally time consuming since there is need to invert larger operator matrices.

For a reservoir with fixed dimensions as discussed in chapter 4, the change in the grid size implies a change in the number of grid blocks. The grid size is inversely proportional to the number of grid blocks, that is

$$\Delta v \propto 1/N \qquad (6.1)$$

where $\Delta v = dL_1 \times dL_2 \times dL_3$ is the volume of the grid block, and $N = N_1 \times N_2 \times N_3$ is the number of the grid cells in the x-, y- and z-directions, respectively. Equation (5.1) after removing the proportionality sign reduces to

$$\Delta v = \frac{V}{N} \qquad (6.2)$$

where V is the dimensions of the reservoir model considered. Therefore, a decrease in the grid size implies an increase in the number of grid cells. The number of the grid cells affect the computation time and in this thesis, the size of the grid cells was could not be reduced below $25 \times 25 \times 25 m^3$ due to the limited storage capacity and time for the computer used for the models. When the number of grid cells for a reservoir with fixed dimensions increase, the resolution will be very good at the expense of their variance. A balance between resolution

and variance is needed depending on the aim of the modeling. Therefore during the hydrocarbon exploration and data inversion, to obtain good results the number of grid cells must be increased depending on the specification of the computer since it is memory consuming and requires more computation time for a larger number of grid blocks. The reservoir dimension affects the number of grid cells for fixed grid size. For the code developed since it involves computing Green's function for all approximations and the large inverse matrix for the T-matrix which are memory consuming, it was limited to N<1000 on a laptop with RAM 8.00GB, i5-4200u and processor 2.30 GHz.

It has been found that all the three approximations give the same results (in amplitude and phase) for small contrast. From equation (3.45), the first term is considered in comparison with the higher order terms for small contrasts in updating the scattering field for the Extended Born approximation. Therefore, the scattering tensor will be approximated as,

$$\Gamma = \left[I - \lambda \right]^{-1} = I + I\lambda + I\lambda^2 + ... = \sum_{k=0}^{\infty} \lambda^k \,, \qquad (4.3)$$

where $\Gamma \to I$, as the contrast tends to zero ($\Delta\sigma \to 0$).

As noted from equation (3.66), the T-matrix will be approximated as $T \to \Delta\sigma$ for small contrasts. This therefore implies the scattering fields will be approximated by the background field since equation (3.53) and (3.73) will reduce to equation (3.37) which is the Born approximation. For moderate and high contrasts, T- and Γ- operators are non-linear in the contrast and will now have some small additive terms which modify the field in the scatterer from that of Born. The Extended Born dominates for higher contrasts at the expense of the T-matrix due to the T-operator terms in the TMA being reduced by the multiplying contrast factor ($\Delta\sigma$) when $\Delta\sigma < 1$ depending the conductivity of the surrounding layers. Heterogeneity has been noted to heavily affect both the magnitude and phase a feature that can be used to discriminate the fluids in the reservoir.

6.2 Conclusion

The computational time for TMA approximations is comparable with that required for the Born approximation, although the new approximate solutions are much more accurate. The developed approximations of the electromagnetic field can always be used as effective tools for fast 3D forward modelling. It has been shown that the Extended Born is a better approximation compared to the Born in estimating the electric field within the reservoir for appropriate parameters. This is true because the Extended Born approach considers the total electric field, in the interior of the scatterer to be the result of the application of a tensor on the incident electric field, as opposed to the background field only (Abubakar and Habashy 2005). However, when the T-matrix was considered in addition to the Extended Born in estimating the solution of the integral equation, it was found out that the T-matrix is better solution and it can be considered to calibrate the other approximations.

The numerical modeling results herein presented do prove that the modeling based on the Green's function methods to the integral equation is correct. However, it has been found that much of the computational time for running the code is spent on the computing of the anomalous electric field since it involves a linear system with a dense coefficient matrix which verifies (Bakr and Mannseth 2009) findings. Therefore, while modeling the grid volume must be chosen with great care since it plays an important role in determining the number of the grid cells, size of the co-efficient matrix, resolution and sensitivity of the reservoir the volume of the grid cells.

Independent of the approximation to the integral equation considered, it is generally true that they will agree for small contrasts and grid sizes even though their amplitudes will be small too. It has been found that the error for approximating the integral equation is higher when the Born approach is used instead of the Extended Born relative to the T-matrix approach which roughly approximates the integral equation. Therefore, using the Extended Born instead of the Born reduces the error much more. The numerical results suggest that the T-matrix and the Extended Born approaches are relatively accurate for moderate to high contrasts.

The results demonstrate that the T-matrix and Extended Born methods as approximations to the integral equation based on the Green's function can improve on the sensitivity of the reservoir a fact that can effectively be used in the marine CSEM to discriminate among the different pore-filling fluids in the subsurface due to the higher contrasts that exist within them. Also during production and storage monitoring, the lateral changes must be in position to be noted over time due to variation in the contrasts in the reservoir.

The inversion algorithm using a time-lapse CSEM monitoring example has been tested. Sensitivity analysis examples have been done using Born inversion on forward modeling data from Born, TMA and EBA; and results show that 3D Born approximation is an effective approach used to recover the synthetic data. Time-lapse CSEM approach is especially useful to identify the water flooded zone in the monitoring process.

6.3 Future work

The integral equation approximations studied have been applied to a homogeneous and a simplified heterogeneous model which does not truly represent the subsurface geometry. There is therefore the need to update the Green's function to consider the layered earth model with varying conductivities. For a heterogeneous model the T-matrix approximation needs to be updated by modifying its background Green's function. This modification has been included in the appendix A. The source location and number affects the EM signal that maps the subsurface. It is important that several sources are considered in modeling and inversion of CSEM data.

While carrying out data inversion, linear inverse solutions (Born inversion) have been considered. But it could be quite interesting if the T-matrix and Extended Born inversions could be implemented which are ideally non-linear in nature. The iterative extended Born is

suggested to linearize the Extended Born approximation that is non-linear after a few iterations depending on the initial guess of contrast and background field. This has been included in the appendix.

In inverse modeling, the number of grids in the reservoir play an important role in the recovery of the true model. A different approximation scheme needs to be developed to address the limitations of considering regular grids replaced by irregular ones since the reservoirs do not assume regular shapes. This would greatly reduce on the computation errors of using an approximation of the reservoir on the assumption of being regular.

References

Abubakar, A. and T. M. Habashy (2005). "A Green function formulation of the Extended Born approximation for three-dimensional electromagnetic modelling." Wave Motion **41**(3): 211-227.

Andréis, D. and L. MacGregor (2011). "Using CSEM to monitor production from a complex 3D gas reservoir—A synthetic case study." The Leading Edge **30**(9): 1070-1079.

Árnason, G. P. H. a. K. (2010). "RESISTIVITY OF ROCKS ": 1-8.

Avdeev, D. (2005). "Three-Dimensional Electromagnetic Modelling and Inversion from Theory to Application." Surveys in Geophysics **26**(6): 767-799.

Bakr, S. and T. Mannseth (2009). Fast 3D modeling of the CSEM response of petroleum reservoirs. SEG Technical Program Expanded Abstracts 2009, Society of Exploration Geophysicists**:** 669-673.

Bhuyian, A., M. Landrø and S. Johansen (2012). "3D CSEM modeling and time-lapse sensitivity analysis for subsurface storage." GEOPHYSICS **77**(5): E343-E355.

Black, N. and M. S. Zhdanov (2010). "Active Geophysical Monitoring of Hydrocarbon Reservoirs Using EM Methods." **40**: 135-159.

Charalambopoulos, A., G. Dassios, G. Perrusson and D. Lesselier (2002). "The localized nonlinear approximation in ellipsoidal geometry: a novel approach to the low-frequency scattering problem." International Journal of Engineering Science **40**(1): 67-91.

Chew, W. C. (1999). "Waves and Fields in Inhomogenous Media." IEEE Press: 632.

Constable, S. (2010). "Ten years of marine CSEM for hydrocarbon exploration." GEOPHYSICS **75(**5): 75A67-75A81.

Constable, S. and L. Srnka (2007). "An introduction to marine controlled-source electromagnetic methods for hydrocarbon exploration." GEOPHYSICS **72**(2): WA3-WA12.

Constable, S. and C. Weiss (2006). "Mapping thin resistors and hydrocarbons with marine EM methods: Insights from 1D modeling." GEOPHYSICS **71(**2): G43-G51.

Eidesmo, T., S. Ellingsrud, L.M. MacGregor, S. Constable, M.C. Sinha, S. E. Johansen and F. N. K. a. H. Westerdahl (2002). "Sea Bed Logging (SBL), a new method for remote and direct identification of hydrocarbon filled layers in deepwater areas." EAGE **20**(Vol 20, No 3, March 2002): 9.

Gao, G., A. Abubakar and T. Habashy (2010). Simultaneous joint petrophysical inversion of electromagnetic and seismic measurements. SEG Technical Program Expanded Abstracts 2010**:** 2799-2804.

Gao, G., S. Fang and C. Torres-Verdín (2003). A New Approximation for 3D Electromagnetic Scattering in the Presence of Anisotropic Conductive Media. ASEG Extended Abstracts 2003**:** 1-9.

Gelius, L. and M. Tygel (2013). The cost function used in 3D mCSEM inversion – is the Born approximation valid? 13th International Congress of the Brazilian Geophysical Society & EXPOGEF, Rio de Janeiro, Brazil, 26–29 August 2013**:** 97-101.

Habashy, T. M., R. W. Groom and B. R. Spies (1993). "Beyond the Born and Rytov Approximations - a Nonlinear Approach to Electromagnetic Scattering." Journal of Geophysical Research-Solid Earth **98**(B2): 1759-1775.

Hansen, P. C. (2010). "Discrete Inverse Problems: Insight and Algorithms." SIAM Journal on Scientific Computing: 53-75.

Jakobsen, M. (2012). "T-matrix approach to seismic forward modelling in the acoustic approximation." Studia Geophysica Et Geodaetica **56**(1): 1-20.

Jean-Louis Chardac, Mario Petricola, S. J. and. and B. Dennis (1996). "in search of saturation."

Johansen, S., T. Wicklund and H. Amundssen (2007). "Interpretation example of marine CSEM data." The Leading Edge **26**(3): 348-354.

Kahnert, F. M. (2003). "Numerical methods in electromagnetic scattering theory." Journal of Quantitative Spectroscopy and Radiative Transfer **79–80**(0): 775 - 824.

Kang, S., S. J. Seol and J. Byun (2011). A Feasibility Study of CO2 Sequestration Monitoring Using the MCSEM Method At a Deep Brine Aquifer In a Shallow Sea.

Lien, M. and T. Mannseth (2008). "Sensitivity study of marine CSEM data for reservoir production monitoring." GEOPHYSICS **73**(4): F151-F163.

M.S. Zhdanov, M. E., N. Black, L. Spangler, S. Fairweather, R. Will, A. Hibbs and G. Eiskamp (2013). "Carbon Capture Utilization & Storage - Geophysical Monitoring " 75th EAGE Conference & Exhibition incorporating SPE EUROPEC 2013 1-5.

Martin Čuma, Masashi Endo, K. Yoshioka and M. S. Zhdanov (2008). "Electromagnetic modeling of large 3D geological structures with inhomogeneous background conductivity." Journal of Geophysics and Engineering **5**(4): 438–447

Mehta.K, a. Nabighian.M and L. Y. (2005). Controlled source electromagnetic (CSEM) technique for detection and delineation of hydrocarbon reservoirs: an evaluation. SEG Technical Program Expanded Abstracts 2005**:** 546-549.

Menke, W. (1989). "Geophysical Data Analysis: Discrete Inverse Theory." International geohysics Series **45**: 1-97.

Menke, W. (2012). "Geophysical Data Analysis: Discrete Inverse Theory (Third Edition)." Elsever: 1-122.

P. C. Hansen and D. p. O'Leary (1993). "THE USE OF THE L-CURVE IN THE REGULARIZATION OF DISCRETE ILL-POSED PROBLEMS." SIAM Journal on Scientific Computing **14**(6): 1487- 1503.

Ray, A. and K. Key (2012). "Bayesian inversion of marine CSEM data with a trans-dimensional self parametrizing algorithm." Geophysical Journal International **191**(3): 1135-1151.

S. E. Johansen, H.E.F. Amundsen, T. Røsten, S. Ellingsrud and T. E. a. A. H. Bhuiyan (2005). "subsurface hydrocarbons detected by electromagnetic sounding." (Vol 23, No 3, March 2005).

Shahin, A., K. Key, P. Stoffa and R. Tatham (2010). Time-lapse CSEM analysis of a shaly sandstone simulated by comprehensive petro-electric modeling. SEG Technical Program Expanded Abstracts 2010**:** 889-894.

Sheng, P. (1995). "Introduction to Wave Scattering, Localization, and Mesoscopic Phenomena " Elsever.

Song, L. L.-P. and Q. H. Q. Liu (2004). "Fast three-dimensional electromagnetic nonlinear inversion in layered media with a novel scattering approximation." Inverse problems **20**(6): S171-S194.

Stav, A. (2010). "Forovermodellering og inversjon av 3D og 4D CSEM-data basert på integralligningsmetoder." Bora.

Streich, R. (2009). "3D finite-difference frequency-domain modeling of controlled-source electromagnetic data: Direct solution and optimization for high accuracy." GEOPHYSICS **74**(5): F95-F105.

Summerfield, P., L. Gale, X. Lu, T. Phillips, R. Quintanilla, E. Eriksen, A. Rutledge and K. Solon (2005). Marine CSEM acquisition challenges. SEG Technical Program Expanded Abstracts 2005**:** 538-541.

Tadiwa, E. N., N. Yahya, B. H. Halabi, Y. B. N. Mohd and R. M. a. A. Ansari (2013). "Investigating Deep Target Reservoirs Using MCSEM Methods." International Journal of Scientific and Engineering Research **4**(5): 86-90.

Tehrani, A. M. and E. Slob (2010). "Fast and accurate three-dimensional controlled source electromagnetic modelling†." Geophysical Prospecting **58**(6): 1133-1146.

Torres-Verdin, C. and T. M. Habashy (1995). "A two-step linear inversion of two-dimensional electrical conductivity." Antennas and Propagation, IEEE Transactions on **43**(4): 405-415.

Vilamajó, E., P. Queralt, J. Ledo and A. Marcuello (2013). "Feasibility of Monitoring the Hontomín (Burgos, Spain) CO2 Storage Site Using a Deep EM Source." Surveys in Geophysics **34**(4): 441-461.

Wang, Y., W. Luo, Z. He, W. Sun and Z. Wang (2008). Born Approximation Inversion For the Marine CSEM Data Set.

Yahya, N. (2012). "Guided and Direct Wave Evaluation of Controlled Source Electromagnetic Survey Using Finite Element Method." Journal of Electromagnetic Analysis and Applications **04**(03): 135-146.

Yves Gueguen and V. palciauskas (1994). "Introduction to the Physics of Rocks." 182-247.

Zach, J., M. Frenkel, D. Ridyard, J. Hincapie, B. Dubois and J. Morten (2009). Marine CSEM time-lapse repeatability for hydrocarbon field monitoring. SEG Technical Program Expanded Abstracts 2009**:** 820-824.

Zhdanov, M. S. (2002). "Geophysical Inverse Theory and Regularization Problems." Elsever **36**: 3-609

Zhdanov, M. S. (2009). Geophysical Electromagnetic Theory and Methods. Methods in Geochemistry and Geophysics. Amesterdam, Elsevier. **43**.

Zhdanov, M. S., V. I. Dmitriev, S. Fang and G. Hursan (2000). "Quasi-analytical approximations and series in electromagnetic modeling." Geophysics **65**(6): 1746-1757.

Appendix

As suggested for future work, the bckground field can be updated to prvide better results for using T-matrix approximation in forward and inversion.

Background Green's Function for T-matrix

In a heterogeneous model, the background Green's tensor needs to be modified. The background Green's function for T-matrix in a heterogeneous media can be derived from equation (3.65) as

$$\mathbf{T}^b = \Delta\boldsymbol{\sigma}^b + \Delta\boldsymbol{\sigma}^b \mathbf{G}^o \mathbf{T}^b \tag{1}$$

where $\mathbf{T}^b$ and $\Delta\boldsymbol{\sigma}^b$ are the T-matrix and anomalous conductivity in the homogeneous background media. By re-arranging equation (6.1),

$$\mathbf{T}^b = \left(\mathbf{I} - \Delta\boldsymbol{\sigma}^b \mathbf{G}^o\right)^{-1} \Delta\boldsymbol{\sigma}^b \tag{2}$$

The background green's tensor is written as

$$\mathbf{G}^b = \mathbf{G}^o + \mathbf{G}^o \mathbf{T}^b \mathbf{G}^o \tag{3}$$

$\mathbf{G}^o$ is the Green's tensor in the homogeneous background media. By substituting equation (6.2) into equation (6.3)

$$\mathbf{G}^b = \mathbf{G}^o + \mathbf{G}^o \left(\mathbf{I} - \Delta\boldsymbol{\sigma}^b \mathbf{G}^o\right)^{-1} \mathbf{G}^o \tag{4}$$

where $\mathbf{G}^b$ is the new background Green's tensor for the heterogeneous media. This new tensor is now used to compute the T-matrix in equation (3.66).

The Iterative Extended Born Approximation

The total electric field inside the reservoir for the Extended Born approximation has been found in discretized form to be written as

$$\mathbf{E}_i = \mathbf{E}_i^b + \mathbf{G}_{ij}^b \Delta\boldsymbol{\sigma}_{jk}^1 \boldsymbol{\Gamma}_{kl}^0 \mathbf{E}_l^b \tag{5}$$

For iterative Extended Born approximation, the total field has to be updated. Similar to the iterative Born approximation but keeping the concept of Extended Born approximation in every iteration, we get for the general iterative form (Tehrani and Slob 2010) as,

$$\mathbf{E}_i^n = \mathbf{E}_i^b + \mathbf{G}_{ij}^b \Delta\boldsymbol{\sigma}_{jk}^{n+1} \boldsymbol{\Gamma}_{kl}^n \mathbf{E}_l^b \qquad (6)$$

$n = 1, 2, 3, \ldots$, is the number of iterations performed.

The Born approximation being a primary field is considered as the first (initialization) term for the series. Though equation is not a proper series and does not converge, it however improves the total field in a few iterations.

$$\boldsymbol{\Gamma}_{kl}^n = \left[I - \mathbf{G}_{lj}^b \Delta\boldsymbol{\sigma}_{jk}^{n+1} \right]^{-1} \qquad (7)$$

This depends on the contrast and the depolarization tensor. So, with an initial value for contrast, the series will depend on the tensor that has to be updated for each iterate. In Matlab, only the depolarization tensor needs to be updated for each iterate. These iterations make the EBA to behave as a linear equation which can then be used for inversion of data.

Matlab Scripts

These codes combine the Born, Extended Born and T-matrix approximations to the integral equation for a geo-electrical model with both homogeneous and heterogeneous conductivity contrasts for forward and inverse modeling. For homogeneous model, sigma is a constant. In these codes, only the anomalous E-field is considered in the computation of the amplitude and phase which are obtained by finding the L-2 norm of the real and the imaginary parts of the anomalous E-field and by calculating the arc tangent of the quotient of the imaginary and the real parts of the E-field. The codes are implemented to cater for 2D, 3D and 4D modeling for both isotropic and anisotropic media.

G_{vv} and are the Green's tensors for the background and the scattering domain. The G_{vv} is computed for the interaction in absence of the Scatterer; while G_rv is computed in the presence of the scatterer. L_1, L_2, and L_3 are the dimensions of the reservoir having N_1, N_2, and N_3 grid cells with dL_1, dL_2, and dL_3 as the sizes of the grid cells; and S_1, S_2, and S_3 are the initial positions of the scattering domain in the X, Y and Z directions, respectively.

1) For Born approximation,

$E_a = G_{rv} \times E^b \times dsigma$; where E_a and E^b are the scattering and background electric fields, dsigma is the conductivity contrast of the scatterer.

2) For Extended-Born approximation

$E_a = G_{rv} \times dsigma \times E_h$; where

$E_h = Gamma \times E^b$;

$Gamma = inv\left(I - G_{vv} \times dsigma\right)$.

when E_h is the modified background E-field to cater for multiple scatterings.

3) For T-matrix approximation

$E_a = G_{rv} \times T \times E^b$; with

$T = inv\left(I - dsigma \times G_{vv}\right) \times dsigma$

From the computations for the different approximations, the Magnitude and phase against offset were plotted for these approximations for comparison under different reservoir parameters.

```
%%%%%%%%%%%%%%%%%%%%%%%%%%%%%%%%%%%%%%%%%%%%%%%%%%%%%%%%%%%%%%%%%%%%%%%%%%%%%%%%
                                    EMForward.m
%%%%%%%%%%%%%%%%%%%%%%%%%%%%%%%%%%%%%%%%%%%%%%%%%%%%%%%%%%%%%%%%%%%%%%%%%%%%%%%%
clear all; close all;
global dV sigma_0

% Isotropic background medium with conductivity equal to one
sigma_0 = 0.5;
% Receiver positions
max_offset = 6000;
r1= -max_offset/2;
r2 = 0;
rows = 13;
Mx = 31;
dx = max_offset/Mx;
My = rows;
receivers = Mx;

M = Mx*My;
R = zeros(3,M);
t = 0;
for rr = 1:My
  for mm = 1:Mx
     t = t+1;
     R(1,t) = r1 + max_offset*(mm-1)/(Mx-1);
     if rows > 1
        R(2,t) = r1 + max_offset*(rr-1)/(My-1);
     else
       R(2,t) = 0;
     end
     R(3,t) = 0;
   end
end

x = linspace(r1,r1+max_offset,receivers); % offset

% Reservoir Dimensions
L1 = 1500;
L2 = 1500;
L3 = 50;
N1 = 30;
N2 = 30;
N3 = 1;
N = N1*N2*N3;
dL1 = L1/N1;
dL2 = L2/N2;
dL3 = L3/N3;

dV = dL1*dL2*dL3;
s3 = 850;
S = zeros(3,N);
```

```
sigma11_viz = zeros(N1,N2);
t = 0;

% Scattering Positions
for cc = 1:N3
   for bb = 1:N2
      for aa = 1:N1
         t = t + 1;
         if N1 > 1
            S(1,t) = -L1/2 - dL1/2 + aa*dL1;
         else
            S(1,t) = 0;
         end
         if N2 > 1
           S(2,t) = -L2/2 - dL2/2 + bb*dL2;
         else
            S(2,t) = 0;
         end
         S(3,t) = s3 + (cc-1)*dL3;

         b1 = 0.20*N2 +0.3*N2*sin(pi*bb/N2);
         %b1 = 0; % for o% saturation
         if aa < b1
            sigma(1,1,t) = 0.5;
         else
            sigma(1,1,t) = 0.01;
         end
         sigma(2,2,t) = sigma(1,1,t);
         sigma(3,3,t) = sigma(1,1,t);
         sigma11_viz(aa,bb) = sigma(1,1,t);

      end
   end
end


%% Green's Tensor
G4 = zeros(3, 3, M, N); % scattering tensor
for p = 1:M
   for q = 1:N
      Y = R(1:3,p) - S(1:3, q);
      tmp = greens(Y);
      for a = 1:3
         for b = 1:3
            G4(a,b,p,q) = tmp(a,b);
         end
      end
   end
end

G_rv = zeros(M, 3*N);
for a = 1:3
   for b = 1:3
      for p = 1:M
         for q = 1:N
            I = (a-1)*M + p;
            J = (b-1)*N + q;
            G_rv(I,J) = G4(a,b,p,q);
         end
      end
```

```
   end
end

%%
% Background Electric Field
source_strength = 100*1000;
source_vector = [source_strength 0 0]';
Eb_born = zeros(1,3*N);

for k = 1:3
   for t =1:N
      K = (k-1)*N+ t;
      G_VS = greens(S(1:3,t));
      tmp= G_VS*source_vector;
      Eb_born(K) = tmp(k);
   end
end
Eb_born = transpose(Eb_born);

Eb_diag = zeros(3*N,3*N);
for K = 1:3*N
   Eb_diag(K,K) = Eb_born(K);
end

 % anisotropic background field
 Eb = zeros(N,3);
 for k = 1:3
     for p =1:N
         G_VS = greens(S(1:3,p));
         tmp = G_VS*source_vector;
         Eb(p,k) = tmp(k);
     end
 end


V = zeros(3*N,3*N); % anomalous conductivity
dsigma = zeros(3,3);
for a = 1:3
   for b = 1:3
      for p = 1:N
         for q = 1:N
            I = (a-1)*N + p;
            J = (b-1)*N + q;
            if p == q
               delta_pq = 1;
            else
               delta_pq = 0;
            end

            dsigma(a,b) = sigma(a,b,p) - sigma_b(a,b);
            V(I,J) = dsigma(a,b)*delta_pq*dV;

         end
      end
   end
end
Vt = diag(V);

G4 = zeros(3, 3, N, N); % background greens tensor
```

```
for p = 1:N
   for q = 1:N
      Rx_Sx = S(1:3,p) - S(1:3,q); % receiver -scatterer distance
      tmp = greens(Rx_Sx);
      for a = 1:3
         for b = 1:3
            G4(a,b,p,q) = tmp(a,b); % green's tensor with 4 indices
         end
      end
   end
end

G_vv = zeros(3*N, 3*N);
for a = 1:3
   for b = 1:3
      for p = 1:N
         for q = 1:N
            I = (a-1)*N + p;
            J = (b-1)*N + q;
            G_vv(I,J) = G4(a,b,p,q);
         end
      end
   end
end

%% EBA computation

 G41 = zeros(3,3,N,N); % 4 tensor Green's
 delta_s = zeros(3,3,N);

  for p = 1:N
   for q = 1:N
       ss = S(1:3,p) - S(1:3,q); % scatterer receiver distance
       tmp = greens(ss);
     for a = 1:3
       for b = 1:3
           I = (a-1)*N + p;
           J = (b-1)*N + q;

            if a == b
                delta_ij = 1;
            else
                delta_ij = 0;
            end
     dsigma(a,b) = sigma(a,b,p) - sigma_b(a,b);
    delta_s(a,b,p) = dsigma(a,b)*delta_ij*dV;% conductivity for each grid
block

    G41(a,b,p,q) = tmp(a,b); % Green's funtion for each grid block

       end
     end
   end
  end

 AA = eye(3);
 BB = eye(3);
 Gamma = zeros(3,3,N);
 ramda = zeros(3,3,N);
 E = zeros(N,3);
```

```
 Eh = zeros(1,3*N);

for p = 1:N
    Ebb(1) = Eb(p,1);
    Ebb(2) = Eb(p,2);
    Ebb(3) = Eb(p,3);
    Gamma = zeros(3,3);
    for q = 1:N
          AA = G41(:,:,p,q);
          BB = delta_s(:,:,q);

      % A vector of tensors
          Gamma = AA*BB + Gamma;

      % inverse Scattering or Depolarizing tensor
          ramda = inv(eye(3)- Gamma);
    end
     tmp = ramda*transpose(Ebb);

    E(p,1) = tmp(1);
    E(p,2) = tmp(2);
    E(p,3) = tmp(3);

end

for a = 1:3
    for p = 1:N
        I = (a-1)*N + p;

     % modified field for the Scattering domain
        Eh(I)= E(p,a);
    end
end
Eh = transpose(Eh);

Eh_diag = zeros(3*N,3*N);
for K = 1:3*N
   Eh_diag(K,K) = Eh(K);
end

%% Computation of Approximations

II = eye(3*N);
T = V*inv(II - G_vv*V);
%T = V;
db2 = G_rv*V*Eb_born;
dT2 = G_rv*T*Eb_born;
dbe2 = G_rv*V*Eh;

% Noise level
for nr = 1:length(db)
    db(nr) = db(nr)*(1 + 0.000*rand);
end
```

%%%

EMinversion.m

%%%

```
%EMforward

A0 = G_rv*Eb_diag;

eps = 1e-5;
it = 0;
inversion_error = 1;
data_error = 1;

while data_error > 1E-5 && it < 100
   it = it + 1
   eps = eps*0.1

   % This is the inversion!
   V_inv = inv(real(A0'*A0) + eps*eps*II)*real(A0'*db);

   data_error = norm(db - A0*V_inv)/norm(db);
   inversion_error = norm(V_inv - Vt)/norm(Vt);

   data_err(it) = data_error;
   inv_err(it) = inversion_error;

   norm_m(it) = norm(V_inv);
   norm_E(it) = norm(db - A0*V_inv);
   m_inv(it, :,:) = V_inv;
end

[aa bb] = min(inv_err);

Vtp = Vt/dV;
V_invp = m_inv(bb, :,:)/dV;
%%%%%%%%%%%%%%%%%%%%%%%%%%%%%%%%%%%%%%%%%%%%%%%%%%%%%%%%%%%%%%%%%%%%%%%%%%%%
                                 greens.m
%%%%%%%%%%%%%%%%%%%%%%%%%%%%%%%%%%%%%%%%%%%%%%%%%%%%%%%%%%%%%%%%%%%%%%%%%%%%

function G = greens(x);
global dV sigma_0

 I0 = 1;
 dl = 1; % Modified by Morten
 f = 0.25;
 omega = 2*pi*f;
 mu0 = 4*pi*1E-7;

 k = sqrt(1i*omega*mu0*sigma_0);
 r = norm(x);

 if r > 0.1
 g = 1i*omega*mu0*I0*dl*exp(1i*k*r)/(4*pi*r); % Green's Scalar function

 E = 1/(k^2)*1/(r*r)*g;
 Et = E*(k*k*r*r + 1i*k*r - 1);
 Ert = E*(-3*1i*k + 3/r - r*k*k)*(1/r);

 Exx = Ert*x(1)*x(1) + Et;
 Exy = Ert*x(1)*x(2);
 Exz = Ert*x(1)*x(3);
```

```
 Eyx = Exy;
 Eyy = Ert*x(2)*x(2) + Et;
 Eyz = Ert*x(2)*x(3);

 Ezx = Exz;
 Ezy = Eyz;
 Ezz = Ert*x(3)*x(3) + Et;

G = [ Exx Exy Exz; Eyx Eyy Eyz; Ezx Ezy Ezz ];
 else
     G = zeros(3,3);
     G(1,1) = (-1/(3*sigma_0*dV));
     G(2,2) = G(1,1);
     G(3,3) = G(1,1);
 end

end
```